

**ACTIVE MEMBRANES FOR CONTAINING AND TREATING  
ENVIRONMENTAL CONTAMINATION**

A DISSERTATION  
SUBMITTED TO THE FACULTY OF THE GRADUATE SCHOOL  
OF THE UNIVERSITY OF MINNESOTA  
BY

**ERIN MEHLEIS SURDO**

IN PARTIAL FULFILLMENT OF THE REQUIREMENTS  
FOR THE DEGREE OF  
DOCTOR OF PHILOSOPHY

DR. WILLIAM A. ARNOLD, ADVISOR

DECEMBER 2009



## **Acknowledgements**

My heartfelt thanks go first to my adviser, Dr. William Arnold, for all of his wisdom and encouragement during my graduate education process. His broad spectrum of knowledge in chemistry and engineering helped shape this dissertation and guided the development of my own set of skills and knowledge. I learned so much, and, because of Dr. Arnold's well-balanced combination of patience and enthusiasm, I had a great deal of fun along the way.

This dissertation would also not have been possible without the contributions of Dr. Edward Cussler. His expertise in the areas of diffusion and reactive membranes helped me link theory to observation again and again. I would also like to thank Dr. Paige Novak for her active participation in my research and her guidance on all things microbiology. I would especially like to thank Dr. Novak for "adopting" me into her group while my adviser was away on sabbatical. Appreciation is also extended to Drs. Jim Cotner and John Gulliver for serving on my committee and strengthening my thesis during our discussions at my preliminary and final oral exams.

For their consistent supply of thoughtfulness, camaraderie, and fun, I would like to thank the many classmates, labmates, and officemates I have had the opportunity to work with during my time at the University of Minnesota. I would especially like to thank Tsutomu "Shimo" Shimotori, Andy Warta, Jenna Grady, Andrea Azary, and Mahati Chintapalli for their specific contributions to this dissertation. Sorbent particle characterization contributions from Navid Saleh and Ifthecker Khan (University of South Carolina) and Atif Choudhury (Vanderbilt University) are also appreciated.

Finally, special thanks go to my husband, Pete, for his endless encouragement both in research and in life. I cannot say enough about how much his support has meant to me. Encouragement from my parents, Dan and Lee Anne Mehleis, my sister and brother-in-law, Sarah and Brent Ruter, and the Surdo family has also been invaluable.

Financial support for this work came from a variety of sources, including grants from the U.S. Department of Energy (Environmental Management Science Program of the Office of Science, Grant #DE-FG07-02ER63509) and the Cooperative Institute for Coastal and Estuarine Environmental Technology (CICEET). I am also grateful for the financial support provided by University of Minnesota Graduate School and Doctoral Dissertation Fellowships and the National Science Foundation's Integrative Graduate Education and Research Traineeship (NSF-DGE 0504195).

## Abstract

Many hydrophobic compounds can diffuse through the hydrophobic high-density polyethylene (HDPE) geomembranes used to contain contaminated material in waste disposal and environmental engineering applications. Scavenger materials layered with or added to HDPE can intercept diffusing molecules via transformation or sorption, slowing the perceived rate of diffusion across the barrier.

Diffusion of a variety of chlorinated organic contaminants across HDPE, HDPE sandwich membranes, and HDPE/poly(vinyl alcohol) (PVA) composites containing zero-valent iron and powdered activated carbon (PAC) was measured. Reaction of carbon tetrachloride with zero-valent iron and sorption of trichloroethylene to PAC in sandwich membranes were fast, effectively delaying breakthrough until scavenger activity was exhausted. The diffusion of 1,2,4-trichlorobenzene and 2,3',4',5-tetrachlorobiphenyl was measured for HDPE, PAC-containing HDPE, and an HDPE/PVA composite using PAC as a scavenger in the PVA layer. Because diffusion of these bulky aromatic compounds was slow, sorption rates within the HDPE matrix were limited by diffusion from the bulk membrane to the PAC particle surface. The reduced sorption rate allowed some contaminant molecules to leak across the barriers, but the PAC captured enough to substantially slow the overall contaminant flux. In both studies, scavengers were more effective (more of the scavenger was available for reaction or sorption) when placed in a hydrophilic matrix layered with the HDPE.

Because PAC successfully intercepted such of variety of contaminants in our initial studies, factors controlling the sorption rate in active membranes were further explored

via comparison of PAC- and single-walled carbon nanotube (SWCNT)-containing PVA films. This study highlights the role of macropore/micropore diffusion on the kinetics of uptake by membrane-bound sorbent particles. While SWCNTs exhibit similar sorption capacities as PAC in aqueous solution, access of 1,2,4-trichlorobenzene to the sorption sites on the SWCNTs was severely limited in the PVA matrix.

This work provides experimental evidence for improved containment and a theoretical framework useful for the design of prototype and field-scale active membrane barriers. These findings also identify some limitations associated with the membrane encapsulation of scavenger materials and highlight the need for additional laboratory studies.

## Table of Contents

Acknowledgements	i
Abstract	iii
Table of Contents	v
List of Tables	x
List of Figures	xi
List of Acronyms	xv
List of Symbols	xvii
Chapter 1 Introduction	1
1.1 Geomembrane Barriers for Contaminant Containment	2
1.2 Contaminant Diffusion Across HDPE Membranes	5
1.3 Dissertation Overview	8
Chapter 2 Active Barrier Membranes: Review of Theory and Examples from the Literature	10
2.1 Diffusion Across Passive Polymer Membranes	11
2.1.1 Diffusion Across Homogeneous Polymers	11
2.1.2 Measuring Diffusion Using Membrane Uptake Experiments	13
2.1.3 Diffusion Across Membranes with Aligned Impermeable Flakes	14
2.2 Diffusion Across Active Membranes – Moving Reactive Front Model	15
2.2.1 Fast and Irreversible Reaction	15
2.2.2 Fast and “Irreversible” Sorption	17

2.2.3	Increasing Reactive Membrane Lag Times with Aligned Flakes	19
2.2.4	Characterizing Leakage in Reactive Membranes	19
2.3	Diffusion Across Active Membranes – Pseudo-First-Order Kinetics Model	20
2.3.1	Steady “Reaction” Model	20
2.3.2	Diffusion-Limited Kinetics Model	21
2.4	Diffusion Across Active Membranes – Fast Equilibrium Model	23
2.5	Active Membrane Models Summary	24
2.6	Composite Membranes	25
2.7	Membranes and Reactive Membranes for Non-Barrier Use	27
Chapter 3	Sorptive and Reactive Scavenger-Containing Sandwich Membranes as Contaminant Barriers	29
3.1	Introduction	30
3.2	Experimental Methodology	32
3.2.1	Preparation of Fe <sup>0</sup> Nanoparticles	32
3.2.2	Preparation of Composite Membranes	32
3.2.3	Breakthrough Experiments	34
3.2.4	Batch Experiments	35
3.2.5	Sample Extraction and Analysis	36
3.3	Results and Discussion	36
3.3.1	CT Containment Using Sandwich Membranes	36
3.3.2	Fe <sup>0</sup> -Containing Sandwich Membranes for TCE Containment	39

3.3.3 PAC-Containing Sandwich Membranes for TCE Containment	43
3.4 Engineering Considerations	47
Chapter 4 Geomembranes Containing Powdered Activated Carbon Have the Potential to Improve Containment of Chlorinated Aromatic Contaminants	50
4.1 Introduction	51
4.2 Experimental Section	54
4.2.1 PAC Preparation and Characterization	54
4.2.2 Membrane Preparation	54
4.2.3 Breakthrough Experiments	55
4.2.4 Equilibrium Experiments	57
4.2.5 Sample Extraction and Analysis	57
4.3 Results and Discussion	59
4.3.1 Pure Polymers	59
4.3.2 HDPE Membranes with PAC	65
4.3.3 HDPE/PVA-PAC Composite Membrane	72
4.3.4 Engineering Implications	74
Chapter 5 Barrier Properties of PVA Membranes with Carbon Nanotubes: A Comparison with Powdered Activated Carbon-Containing PVA	76
5.1 Introduction	77
5.2 Experimental Methodology	80
5.2.1 Materials	80
5.2.2 Sorbent Particle Preparation	80

5.2.3 Sorbent Particle Characterization	81
5.2.4 Membrane Preparation	82
5.2.5 Batch and Breakthrough Experiments	82
5.2.6 Sample Extraction and Analysis	84
5.3 Results	85
5.3.1 Particle Characterization	85
5.3.2 Sorbent Isotherms	88
5.3.3 Breakthrough Curves	90
5.3.4 Membrane Uptake Curves	91
5.4 Discussion	93
5.4.1 Sorption Mechanisms	93
5.4.2 Factors Controlling 1,2,4-TCB Sorption and Diffusion in PVA	97
5.4.3 Factors Controlling Cu <sup>2+</sup> Sorption and Diffusion in PVA	101
5.4.4 Implications	102
Chapter 6 Conclusions	104
6.1 Benefits of Active Barriers	105
6.2 Challenges in Active Barrier Design	105
6.3 Framework for Optimization/Prediction of Contaminant Flux	106
6.4 Opportunities for Future Research	108
References	111

Appendix A Flux Predictions for a Sorptive Abiotic Membrane, a Biologically-Active Membrane, and a Two-Layer Active Membrane for PCB Containment	127
A.1 Introduction	127
A.2 A Single PAC-Containing HDPE Barrier	128
A.3 A Single Biologically-Active PAA Barrier	129
A.4 A Composite Abiotic/Biologically-Active Barrier for PCB Containment	132
Appendix B <i>Burkholderia xenovorans</i> strain LB400 Growth on Benzoate at Reduced Dissolved Oxygen Concentrations	133
B.1 Introduction	133
B.2 Experimental Methodology	133
B.2.1 Experimental Apparatus Design	133
B.2.2 Growth Experiments	133
B.2.3 Measurement of Bacterial Growth	134
B.2.4 Measurement of Benzoate Consumption	135
B.2.5 Measurement of Dissolved Oxygen Concentration	135
B.3 Results	135
B.4 Discussion	138
Appendix C Equilibrium Adsorption/Partitioning of 1,2,4-TCB and Cu <sup>2+</sup> in Sorbent-Containing PVA Membranes	140
Appendix D Raman Spectra for Raw and Functionalized SWCNTs and PAC	142

## List of Tables

Table 1-1	Advantages and disadvantages of commonly-used synthetic geomembranes	4
Table 1-2	Diffusion coefficients $\times 10^{12}$ (m <sup>2</sup> /s) in HDPE for several common organic environmental contaminants	6
Table 1-3	HDPE-water partition coefficients (unitless) for several common organic environmental contaminants	7
Table 2-1	Assumptions and relationships of breakthrough curve models for membranes with active scavengers	25
Table 3-1	Summary of non-reactive TCE breakthrough experiments	41
Table 3-2	Summary of PAC-containing composite membrane breakthrough experiments using TCE	46
Table 4-1	Pure polymer transport data	60
Table 4-2	Observed and expected model parameter values for PAC-containing HDPE membranes	68
Table 4-3	Diffusion-limited kinetics model scale-up estimates for PAC-containing barriers	75
Table 5-1	Sorbent particle characteristics	85
Table 5-2	Breakthrough experiment data	93
Table 5-3	Relative second-order sorption rate constants and Damköhler numbers for some experimental membranes	98
Table A-1	Base values for predicting flux across single-layer and composite membranes	128
Table B-1	Oxygen diffusion coefficients ( <i>D</i> ) reported in the literature	139

## List of Figures

Figure 2-1	A generic pure polymer breakthrough curve	12
Figure 2-2	Schematic of a barrier membrane	13
Figure 2-3	A model barrier membrane containing aligned impermeable flakes	14
Figure 2-4	Concentration profiles in pure and reactive particle-containing membranes	15
Figure 2-5	Schematic of a Langmuir isotherm curve	18
Figure 2-6	Unit cell for diffusion toward a membrane-bound particle	22
Figure 3-1	Composite membrane assembly	33
Figure 3-2	Diaphragm cell apparatus for measuring solute breakthrough across membranes	34
Figure 3-3	Normalized CT breakthrough curves for a pure HDPE, composite, and Fe <sup>0</sup> -containing composite membranes	37
Figure 3-4	Replicate normalized breakthrough curves for TCE using single-layer HDPE membranes	40
Figure 3-5	Normalized TCE breakthrough for sandwich membranes containing Fe <sup>0</sup> nanoparticles	42
Figure 3-6	Normalized TCE breakthrough curves for a pure HDPE, composite, and PAC-containing composite membranes	44
Figure 3-7	Equilibrium sorption data for aqueous TCE sorption to PAC	45
Figure 4-1	Breakthrough curves for 1,2,4-TCB in water and 40:60 acetone:water and for 2,3',4',5-PCB in 40:60 acetone:water across pure HDPE	59
Figure 4-2	HDPE membrane-solution partition coefficients for 1,2,4-TCB and 2,3',4',5-PCB in water and acetone cosolvent solutions	61

Figure 4-3	Replicate 2,3',4',5-PCB breakthrough curves in 40:60 acetone:water across pure HDPE	62
Figure 4-4	Breakthrough curves for 1,2,4-TCB in water and 40:60 acetone:water and for 2,3',4',5-PCB in 40:60 acetone:water across pure PVA	63
Figure 4-5	Equilibrium sorption data for aqueous 1,2,4-TCB sorption to PAC	64
Figure 4-6	Equilibrium sorption data for 2,3',4',5-PCB sorption to PAC from 40:60 acetone:water	65
Figure 4-7	Breakthrough curves for 1,2,4-TCB in water across pure HDPE and PAC-containing HDPE membranes	66
Figure 4-8	Breakthrough curves for 2,3',4',5-PCB in 40:60 acetone:water across pure HDPE and PAC-containing HDPE membranes	67
Figure 4-9	Distribution of the total mass of a sieved PAC sample by particle diameter	69
Figure 4-10	Microscope images of PAC-containing HDPE and PVA membranes	70
Figure 4-11	2,3',4',5-PCB breakthrough in 40:60 acetone:water across an HDPE/PAC-containing PVA composite membrane	73
Figure 5-1	HRTEM images of SWCNT and ox-SWCNT	86
Figure 5-2	HRTEM images of PAC and ox-PAC	87
Figure 5-3	Isotherm data for 1,2,4-TCB sorption to PAC and SWCNTs	89
Figure 5-4	Isotherm data for 1,2,4-TCB sorption to ox-PAC and ox-SWCNTs	90
Figure 5-5	Isotherm data for Cu <sup>2+</sup> sorption to ox-PAC and ox-SWCNTs	91
Figure 5-6	Normalized 1,2,4-TCB breakthrough curves for pure PVA and sorbent-containing PVA membranes	92
Figure 5-7	Normalized Cu <sup>2+</sup> breakthrough curves for pure PVA and functionalized sorbent-containing PVA membranes	92

Figure 5-8	Normalized uptake curves for 1,2,4-TCB using PAC- and SWCNT-containing PVA membranes	94
Figure 5-9	Pseudo-first-order kinetic plot for 1,2,4-TCB uptake by PAC- and SWCNT-containing PVA membranes	94
Figure 5-10	Normalized uptake curves for Cu <sup>2+</sup> using ox-PAC- and ox-SWCNT-containing PVA membranes	95
Figure 5-11	Pseudo-first-order kinetic plot for Cu <sup>2+</sup> uptake by ox-PAC- and ox-SWCNT-containing PVA membranes	95
Figure A-1	Predicted pseudo-steady-state PCB flux across HDPE as a function of membrane thickness	129
Figure A-2	Predicted pseudo-steady-state PCB flux across HDPE as a function of PAC volume fraction	130
Figure A-3	Predicted steady-state PCB flux across PAA as a function of biologically-active degradation Damköhler number	130
Figure A-4	Predicted pseudo-steady-state PCB flux across an HDPE/PAA composite membrane	131
Figure B-1	Experimental apparatus used for supplying LB400 with a constant stream of reduced-oxygen gas	134
Figure B-2	OD <sub>600</sub> for LB400 growth reactors with 21% oxygen	136
Figure B-3	OD <sub>600</sub> for LB400 growth reactors with reduced oxygen concentrations	136
Figure B-4	Pseudo-first-order LB400 growth rate constants for various dissolved oxygen concentrations	137
Figure B-5	Benzoate concentrations in LB400 growth reactors with 21% oxygen	137
Figure B-6	Benzoate concentrations in LB400 growth reactors with reduced oxygen concentrations	138
Figure C-1	Membrane “isotherm” data for aqueous 1,2,4-TCB in equilibrium with PAC- and SWCNT-containing PVA	140

Figure C-2	Membrane “isotherm” data for aqueous 1,2,4-TCB in equilibrium with ox-PAC- and ox-SWCNT-containing PVA	140
Figure C-3	Membrane “isotherm” data for aqueous Cu <sup>2+</sup> in equilibrium with ox-PAC- and ox-SWCNT-containing PVA	141
Figure D-1	Raman spectra of SWCNT and ox-SWCNT	142
Figure D-2	Raman spectra of PAC and ox-PAC	143

## List of Acronyms

BET	Brunauer-Emmett-Teller, regarding a method for determining the specific surface area of particles
CF	chloroform
CNT	carbon nanotube
CSPE	chlorinated sulphonated polyethylene
CT	carbon tetrachloride
DOM	dissolved organic matter
EPDM	ethylene-propylene-diene monomer, a rubber formulation
fPP	flexible polypropylene
HDPE	high-density polyethylene
HRTEM	high-resolution transmission electron microscopy
LDPE	low-density polyethylene
LLDPE	linear low-density polyethylene
MS	mass spectrometry
MWCNT	multi-walled carbon nanotube
ox-PAC	surface-functionalized (oxidized) powdered activated carbon
ox-SWCNT	surface-functionalized (oxidized) single-walled carbon nanotube
PAA	polyacrylamide
PAC	powdered activated carbon
PCB	polychlorinated biphenyl
2,3',4',5-PCB	2,3',4',5-tetrachlorobiphenyl

PTFE	polytetrafluoroethylene
PVA	poly(vinyl alcohol)
PVC	poly(vinyl chloride)
SWCNT	single-walled carbon nanotube
1,2,4-TCB	1,2,4-trichlorobenzene
TCE	trichloroethylene
TEM	transmission electron microscopy
UV	ultraviolet
VOC	volatile organic chemical

## List of Symbols

$A$	area of the membrane normal to the direction of diffusion ( $\text{m}^2$ )
$b$	Langmuir isotherm fitting parameter ( $\text{m}^3/\text{mol}$ )
$C$	solute concentration in solution ( $\text{mol}/\text{m}^3$ )
$C_{down}$	solute concentration in the downstream reservoir ( $\text{mol}/\text{m}^3$ )
$C_e$	minimum equilibrium aqueous concentration at which $q_{max}$ is achieved in the Langmuir isotherm ( $\text{mol}/\text{m}^3$ )
$C_m$	solute concentration in the membrane ( $\text{mol}/\text{m}^3$ )
$C_m(x,t)$	solute concentration in the membrane at given depth $x$ and time $t$ ( $\text{mol}/\text{m}^3$ )
$C_{up}$	solute concentration in the upstream reservoir ( $\text{mol}/\text{m}^3$ )
$C_{s0}$	initial scavenger concentration in the membrane ( $\text{mol}/\text{m}^3$ or $\text{kg}/\text{m}^3$ )
$D$	solute diffusion coefficient in the membrane ( $\text{m}^2/\text{s}$ )
$D_A$	solute diffusion coefficient in polymer type A ( $\text{m}^2/\text{s}$ )
$D_B$	solute diffusion coefficient in polymer type B ( $\text{m}^2/\text{s}$ )
$D_{effective}$	effective solute diffusion coefficient in the membrane under the fast equilibrium model ( $\text{m}^2/\text{s}$ )
$H_B$	membrane-solution equilibrium partition coefficient for polymer type B or an aqueous layer sandwiched between two A layers (dimensionless)
$H$	membrane-solution equilibrium partition coefficient (dimensionless)
$j _{r=R}$	steady-state solute flux toward a spherical scavenger particle surface ( $\text{mol}/\text{m}^2 \cdot \text{s}$ )
$j$	steady-state or pseudo-steady-state flux across the membrane ( $\text{mol}/\text{m}^2 \cdot \text{s}$ )
$K$	sorptive scavenger-membrane partition coefficient (dimensionless)
$k_0$	zero-order rate constant ( $\text{mol}/\text{m}^3 \cdot \text{s}$ )

$k_1$	first-order or pseudo-first-order rate constant (1/s)
$k_2$	second-order rate constant ( $\text{m}^3/\text{mol}\cdot\text{s}$ )
$K_F$	Freundlich isotherm constant ( $\text{mol}^{1-1/n}\cdot\text{m}^{3/n}\cdot\text{kg}^{-1}$ )
$K_M$	Monod half-saturation constant ( $\text{mol}/\text{m}^3$ )
$k_M$	Monod second-order degradation rate constant ( $\text{mol}/\text{kg biomass}\cdot\text{s}$ )
$L$	membrane thickness (m)
$L_{A1}$	thickness of the upstream A layer of a composite membrane (m)
$L_{A2}$	thickness of the downstream A layer of an ABA composite membrane (m)
$L_B$	thickness of the B layer of a composite membrane (m)
$L_C$	thickness of the C layer of a hypothetical layered membrane (m)
$L_{composite}$	composite membrane thickness (m)
$L_{HDPE}$	total thickness of the HDPE layers in a composite membrane (m)
$M_t$	membrane-sorbed solute mass at time, $t$ (kg)
$M_{eq}$	membrane-sorbed solute mass at equilibrium (kg)
$n$	Freundlich isotherm constant (dimensionless)
$OD_{600}$	optical density at 600 nm used to measure bacterial concentrations in free solution (dimensionless)
$P$	solute permeability of the membrane ( $\text{m}^2/\text{s}$ )
$P_A$	solute permeability of polymer type A ( $\text{m}^2/\text{s}$ )
$P_B$	solute permeability of polymer type B ( $\text{m}^2/\text{s}$ )
$P_C$	solute permeability of the C layer of a hypothetical layered membrane ( $\text{m}^2/\text{s}$ )
$P_{composite}$	solute permeability of a composite membrane ( $\text{m}^2/\text{s}$ )

$q$	concentration of solute sorbed to particles (mol/kg)
$q_{\max}$	total capacity of particles for solute sorption (mol/kg)
$r$	direction of diffusion toward a spherical scavenger particle (m)
$r_{LB400}$	rate of PCB degradation by <i>Burkholderia xenovorans</i> strain LB400 (mol/m <sup>3</sup> ·s)
$R$	spherical scavenger particle radius (m)
$S$	radius of diffusion around a spherical scavenger particle (m)
$t$	elapsed time (s)
$t_{lag}$	lag time to membrane breakthrough (s)
$t_{lag,composite}$	composite membrane lag time (s)
$t_{lag,HDPE}$	predicted lag time for only the HDPE layers of a composite membrane (s)
$V_{down}$	downstream reservoir volume (m <sup>3</sup> )
$X$	biomass concentration (kg biomass/m <sup>3</sup> )
$x$	direction of diffusion across a membrane (m)
$\nu$	stoichiometric coefficient for reaction between solutes and reactive scavenger particles within the membrane (dimensionless)
$\Phi$	second Damköhler number (dimensionless)
$\phi$	volume fraction of scavenger particles in the membrane (dimensionless)

# **Chapter 1**

## **Introduction**

### ***1.1 Geomembrane Barriers for Contaminant Containment***

Synthetic polymers are used as physical, chemical, and biological barriers in a variety of applications. For example, many food products are packaged in flexible plastics to protect products from bacteria, moisture, or oxygen. Even the perfect polymer, however, will eventually be penetrated by chemicals. Oxygen diffusion through packaging polymers reduces the shelf-life of foods, an observation that has led to research focused on quantifying oxygen diffusion in packaging polymers (1-3) and developing additives that reduce the oxygen exposure of package contents (4,5). Such additives are often called “scavengers” and can be reactive, absorptive, adsorptive, or biologically-active. Scavengers slow diffusion across polymer barriers by intercepting the diffusing molecules and transforming or sequestering them within the polymer matrix.

In many environmental engineering applications, thin, nonporous polymer barriers called geomembranes are used to separate contaminated material from the environment. For example, high-density polyethylene (HDPE) geomembranes are often used as part of a composite liner system (in tandem with compacted clay) to separate landfilled hazardous and municipal waste from the environment as prescribed by Subtitle D of the Resource Conservation and Recovery Act (6-9). Geomembranes may also be used for lining tanks, evaporative ponds, leachate lagoons, and other reservoirs that may contain hazardous materials (10-12). Vertical barrier systems that use a protective geomembrane layer are expected to improve containment compared with soil or cement alone because of the additional chemical resistance and reduced permeability provided by the geomembrane (13). Additional applications of geomembrane barriers include landfill

covers, sediment caps, floating reservoir covers, secondary containment for storage tanks, and vapor barriers for buildings located on or near contaminated sites (11-15).

A variety of plastics are available for use as geomembrane barriers, including poly(vinyl chloride) (PVC), polypropylene, and low-density and high-density polyethylenes. Table 1-1 is a reproduction from Scheirs (11) that summarizes the general advantages and disadvantages of several common geomembrane materials. While it does have its disadvantages, HDPE is frequently selected for environmental engineering applications due to its superior resistance to chemical and photodegradation and its low cost. Anti-oxidants, carbon black, and other additives are used to reduce the effects of exposure to air, pollution, and ultraviolet (UV) radiation on the physical properties of the barrier (16). In addition, HDPE is easily welded in the field to produce a contiguous barrier for large area applications, such as landfill liners (11,12).

Puncture protection layers (e.g., clay) may be used when installing HDPE barriers to reduce the formation of defects (12), but some defects are inevitable. Moo-Young et al. (17) surveyed geomembrane-lined landfills at 169 sites and found anywhere between 0 and 774 defects/ha. Leakage models have been used to estimate the contributions of transport via defects and diffusion to the overall rate of leakage from an HDPE landfill liner (8,18), though these models are highly dependent upon the assumptions made regarding the number of defects present in the liners. Foose et al. (8) concluded that volatile organic carbon (VOC) transport through HDPE with 2.5 defects/ha was dominated by diffusion through the intact portions of the barrier, raising concerns about diffusion as a route of contaminant transport to the environment.

**Table 1-1.** Advantages and disadvantages of commonly-used synthetic geomembranes<sup>a,b</sup>

	Advantages	Disadvantages
HDPE	<ul style="list-style-type: none"> <li>• Broad chemical resistance</li> <li>• Good weld strength</li> <li>• Good low temperature properties</li> <li>• Relatively inexpensive</li> </ul>	<ul style="list-style-type: none"> <li>• Potential for stress cracking</li> <li>• High degree of thermal expansion</li> <li>• Poor puncture resistance</li> <li>• Poor multiaxial strain properties</li> </ul>
LLDPE	<ul style="list-style-type: none"> <li>• Better flexibility than HDPE</li> <li>• Better layflat than HDPE</li> <li>• Good multiaxial strain properties</li> </ul>	<ul style="list-style-type: none"> <li>• Inferior UV resistance to HDPE</li> <li>• Inferior chemical resistance to HDPE</li> </ul>
fPP	<ul style="list-style-type: none"> <li>• Can be factory fabricated and folded so fewer field fabricated seams</li> <li>• Excellent multiaxial properties</li> <li>• Good conformability</li> <li>• Broad seaming temperature window</li> </ul>	<ul style="list-style-type: none"> <li>• Limited resistance to hydrocarbons and chlorinated water</li> </ul>
PVC	<ul style="list-style-type: none"> <li>• Good workability and layflat behaviour</li> <li>• Easy to seam</li> <li>• Can be folded so fewer field fabricated seams</li> </ul>	<ul style="list-style-type: none"> <li>• Poor resistance to UV and ozone unless specially formulated</li> <li>• Poor resistance to weathering</li> <li>• Poor performance at high and low temperatures</li> </ul>
CSPE	<ul style="list-style-type: none"> <li>• Outstanding resistance to UV and ozone</li> <li>• Good performance at low temperatures</li> <li>• Good resistance to chemicals, acids and oils</li> </ul>	<ul style="list-style-type: none"> <li>• Cannot be thermally welded after ageing</li> </ul>
EPDM	<ul style="list-style-type: none"> <li>• Good resistance to UV and ozone</li> <li>• High strength characteristics</li> <li>• Good low temperature performance</li> <li>• Excellent layflat behaviour</li> </ul>	<ul style="list-style-type: none"> <li>• Low resistance to oils, hydrocarbons and solvents</li> <li>• Poor seam quality</li> </ul>
butyl rubber	<ul style="list-style-type: none"> <li>• Good resistance to UV and weathering</li> <li>• Good resistance to ozone</li> </ul>	<ul style="list-style-type: none"> <li>• Low tear strength</li> <li>• Low resistance to hydrocarbons</li> <li>• Difficult to seam</li> </ul>
nitrile rubber	<ul style="list-style-type: none"> <li>• Good resistance to oils and fuels (but not biodiesel)</li> </ul>	<ul style="list-style-type: none"> <li>• Poor ozone resistance unless properly formulated</li> <li>• Poor tear strength</li> </ul>

<sup>a</sup> Reproduced from (11).

<sup>b</sup> LLDPE=linear low-density polyethylene, fPP=flexible polypropylene, CSPE=chlorinated sulphonated polyethylene, and EPDM=ethylene-propylene-diene monomer rubber.

## ***1.2 Contaminant Diffusion Across HDPE Membranes***

Diffusion of VOCs and other hydrophobic organic compounds in HDPE has been the focus of many laboratory studies (19-26). Diffusion has been measured using membrane uptake experiments, in which HDPE coupons are immersed in the pure liquid compound (19-21) or aqueous solutions (21,22). Breakthrough experiments more accurately simulate environmental applications, where geomembranes are used as barriers separating contaminated material from the clean environment. In a breakthrough experiment, the membrane is fixed between two reservoirs: the contaminated “upstream” reservoir and the initially-clean “downstream” reservoir. Breakthrough experiments have been conducted for a variety of hydrophobic organic compounds in HDPE using either pure liquid compound (23) or aqueous solutions (24-26) upstream.

Contaminant flux across HDPE barrier membranes is driven both by the diffusion coefficient of the specific contaminant in the HDPE matrix,  $D$ , and by the contaminant concentration gradient across the membrane. Table 1-2 lists some  $D$  values for hydrophobic contaminants reported in the literature. First, it is interesting to note that  $D$  measured in experiments where HDPE is exposed to pure compound is typically higher than those using aqueous solutions. This phenomenon is the result of membrane swelling in the presence of pure organic solvents (19,27). It is also useful to view the  $D$  values in Table 1-2 in comparison to  $D$  for hydrophilic chemicals (acetone) that are less compatible with the hydrophobic HDPE matrix. Rowe et al. (29) estimated a maximum  $D$  of  $6 \times 10^{-15}$  m<sup>2</sup>/s for chloride ion in HDPE, reducing concerns about the transport of compounds not classified as “hydrophobic organics” across HDPE barriers.

**Table 1-2.** Diffusion coefficients  $\times 10^{12}$  ( $\text{m}^2/\text{s}$ ) reported for several common organic environmental contaminants<sup>a</sup>

	Pure Compound Uptake <sup>b</sup>	Aqueous Solution Uptake <sup>c,d</sup>	Pure Compound Breakthrough <sup>e</sup>	Aqueous Solution Breakthrough
Trichloroethylene	11.90 (21)	0.500-0.721 (21,22)	7.9 (23)	0.289-0.47 (24,25)
1,2-Dichloroethane	4.2 (20)	n/a	2.4 (23)	n/a
Carbon Tetrachloride	n/a	n/a	n/a	0.134 (28)
Chloroform	n/a	0.490 (22)	3.4 (23)	0.300-0.419 (24,28)
Benzene	6.4 (20)	0.852 (22)	3.2 (23)	0.459 (24)
Toluene	4.44-6.8 (20,21)	0.327-0.347 (21,22)	4.2 (23)	0.228-0.36 (24,25)
Chlorobenzene	2.42-5.4 (20,21)	n/a	n/a	n/a
Acetone	0.51-1.7 (20,21)	n/a	n/a	n/a

<sup>a</sup> References are in parentheses.

<sup>b</sup> Values reported by (20) are those at 25 °C.

<sup>c</sup> Values reported by (21) are those using 30 mM initial concentration.

<sup>d</sup> Values reported by (22) are those using 30 mg/L initial concentration.

<sup>e</sup> Values reported by (23) are those from permeation tests.

<sup>f</sup> Values reported by (24) and (25) are those using 50 mg/L upstream concentration.

Equilibrium membrane-water partition coefficients,  $H$ , reported in the literature are shown in Table 1-3. Absorption of hydrophobic contaminants by HDPE results in an elevated concentration at the upstream membrane-water interface, increasing the contaminant concentration gradient driving diffusion through the polymer. Thus, contaminant flux across a barrier membrane depends on both  $D$  and  $H$ .

**Table 1-3.** HDPE-water partition coefficients (unitless) for several common organic environmental contaminants<sup>a</sup>

	Equilibrium (Uptake) Experiments <sup>b,c</sup>	Breakthrough Experiments
Trichloroethylene	45.81-53.79 (21,22)	n/a
Carbon Tetrachloride	105.4 (28)	25.8 (28)
Chloroform	18.89 (22)	6.0 (24,28)
Benzene	28.19 (22)	n/a
Toluene	57.32-83.92 (21,22)	n/a

<sup>a</sup> References are in parentheses.

<sup>b</sup> Values reported by (21) are those using 30 mM initial concentration.

<sup>c</sup> Values reported by (22) are those using 30 mg/L initial concentration.

Fast diffusion across intact HDPE raises concerns regarding its efficiency as a barrier for hydrophobic organic contaminants. Using the *D* and *H* values listed in Tables 1-2 and 1-3, respectively, Shimotori et al. (28) estimated that carbon tetrachloride (CT) would begin to leak through to the downstream side of a 1.5-mm thick HDPE geomembrane barrier in about one month. Additives, like the oxygen scavengers used in food packaging materials, have the potential to reduce environmental and public health exposure to hydrophobic contaminants by intercepting these compounds as they diffuse through HDPE geomembranes. Reactive zero-valent iron (Fe<sup>0</sup>) added to HDPE and poly(vinyl alcohol) (PVA) membranes has already been shown to improve containment of CT, a solvent occasionally found in landfill leachate (28,30-33). The current research builds on the potential of reactive scavengers to enhance environmental barriers. In addition, this work explores the use of sorptive scavengers and the mechanisms by which sorption slows diffusion in membranes containing them.

### *1.3 Dissertation Overview*

The goal of this research is to explore the use of active scavengers in single-layer and composite membrane systems to improve contaminant barrier performance. The main objectives were to:

- design and evaluate active HDPE-based barriers for improving the containment of small chlorinated solvent molecules found in landfill leachate and of bulky, very hydrophobic sediment contaminants like polychlorinated biphenyls (PCBs),
- evaluate the influence of scavenger characteristics and membrane matrix properties on the effectiveness of scavenger addition to barrier membranes,
- optimize barrier properties by layering active membranes with high scavenger effectiveness with durable, low-permeability membranes like HDPE, and
- develop a framework for predicting contaminant flux across field-scale layered active membranes.

Chapter 2 provides an overview of the one-dimensional diffusion theory used to describe contaminant migration across pure polymers, layered membranes, and membranes containing reactive scavengers. Experimental studies in which this theory has been applied are described. This section also sets a theoretical context for predicting the performance of membranes containing sorptive scavengers, such as activated carbon.

In Chapter 3, the effect of matrix properties on reactive scavenger effectiveness is explored by comparing CT breakthrough across the  $\text{Fe}^0$ -containing HDPE membranes described by Shimotori et al. (28) to sandwich membranes in which  $\text{Fe}^0$  is incorporated into an aqueous layer sandwiched between two HDPE films. This comparison provides

an initial view into the importance of membrane matrix properties (i.e., water solubility) on the efficiency of reaction within a membrane barrier. Chapter 3 also introduces the sorptive scavenger concept. Trichloroethylene (TCE) breakthrough across sandwich membranes containing powdered activated carbon (PAC) is compared to breakthrough across  $\text{Fe}^0$ -containing sandwich membranes.

In Chapter 4, HDPE and PAC-containing HDPE barriers are evaluated for use as landfill liners or sediment caps for the remediation of PCB-contaminated sediments. This section provides some new insights on how kinetics influence the effectiveness of active scavengers in barrier membranes. The effect of membrane matrix was again studied in Chapter 4 through measurement of 2,3',4',5-tetrachlorobiphenyl (2,3',4',5-PCB) breakthrough across a 2-layer membrane comprised of pure HDPE followed by a hydrophilic active layer (PAC-containing PVA).

Chapter 5 focuses on the effects of sorbent properties on sorptive scavenger efficiency in barrier membranes. Sorptive scavengers with different properties (PAC, carbon nanotubes (CNTs), and their surface-oxidized counterparts) were added to hydrophilic PVA membranes, and breakthrough for both 1,2,4-trichlorobenzene (1,2,4-TCB) and copper ion ( $\text{Cu}^{2+}$ ) was measured in an attempt to understand how the mechanisms of sorption (hydrophobic,  $\pi$ - $\pi$ , ionic interactions, etc.) influence contaminant breakthrough.

Finally, Chapter 6 summarizes the implications of the experimental results described in Chapters 3 through 5 and offers suggestions for further research and alternative applications of active membranes in environmental engineering.

## **Chapter 2**

### **Active Barrier Membranes:**

### **Review of Theory and Examples from the Literature**

## 2.1 Diffusion Across Passive Polymer Membranes

### 2.1.1 Diffusion Across Homogeneous Polymers

Diffusion of a solute across a barrier membrane has been described extensively through the use of Fick's second law (34-36):

$$\frac{\partial C_m}{\partial t} = D \frac{\partial^2 C_m}{\partial x^2} \quad (2-1)$$

where  $C_m$  is the solute concentration in the membrane,  $D$  is the solute diffusion coefficient in the membrane,  $t$  is time, and  $x$  is the direction of diffusion.

By solving Fick's second law for a plane membrane of finite thickness separating two solutions, it is possible to predict the solute concentration on the downstream side of the membrane as a function of time (34):

$$\frac{C_{down}}{C_{up}} = \frac{DHA}{LV_{down}} \left( t - \frac{L^2}{6D} - \frac{2L^2}{\pi^2 D} \sum_{n=1}^{\infty} \frac{(-1)^n}{n^2} e^{-\frac{Dn^2\pi^2 t}{L^2}} \right) \quad (2-2)$$

where  $C_{down}$  and  $C_{up}$  are the downstream and upstream solute concentrations, respectively,  $H$  is the membrane-solution partition coefficient of the solute,  $A$  is the area of the membrane normal to the direction of diffusion,  $L$  is the membrane thickness, and  $V_{down}$  is the downstream reservoir volume. The permeability of the membrane,  $P$ , is equivalent to  $DH$ . Equation 2-2 was derived assuming  $V_{down}$  is finite,  $C_{up}$  is constant, and  $C_{down} \ll C_{up}$ . Experimentally, a finite downstream volume is used in conjunction with downstream concentration measurements to determine the cumulative mass of solute that has diffused across the membrane,  $C_{down}V_{down}$ . With a finite downstream volume, however,  $C_{down}$  eventually approaches  $C_{up}$ , reducing flux and invalidating Equation 2-2.

Equation 2-2 is often simplified to its linear form (34,36):

$$\frac{C_{down}}{C_{up}} = \frac{DHA}{LV_{down}}(t - t_{lag}) \quad (2-3)$$

In Equation 2-3,  $C_{down}$  remains zero during the lag time,  $t_{lag}$ , while the solute diffuses from the contaminated side of the membrane to the downstream side. For pure polymer membranes (34,36):

$$t_{lag} = \frac{L^2}{6D} \quad (2-4)$$

After the lag, a constant (steady-state) flux,  $j$ , develops (34,36):

$$j = \frac{DHC_{up}}{L} \quad (2-5)$$

A generic breakthrough curve is shown in Figure 2-1, which shows the lag time and the steady increase in downstream concentration after the lag. An effective contaminant barrier will have a long lag time, a low flux, or both.

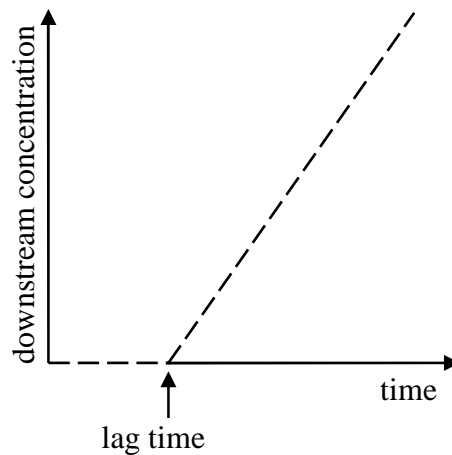


**Figure 2-1.** A generic pure polymer breakthrough curve.

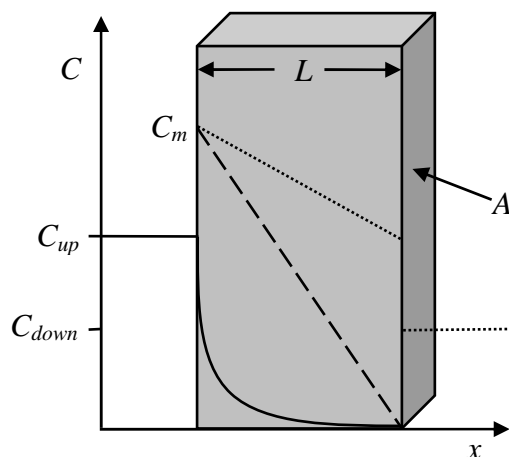


**Figure 2-2.** Schematic of a barrier membrane including concentration profiles for  $t < t_{lag}$  (—),  $t = t_{lag}$  (---) and  $t > t_{lag}$  (····).

Figure 2-2 indicates schematically the concentration and geometric parameters of Equations 2-1 through 2-5. It includes concentration profiles within the membrane ( $C_m$ ) as a function of location within the membrane,  $x$ , at various times in the breakthrough curve. Because  $C_m$  at the upstream surface of the membrane is equivalent to  $HC_{up}$ , the higher  $C_m$  relative to  $C_{up}$  shown in Figure 2-2 indicates  $H > 1$ , which is the case for hydrophobic solutes in a hydrophobic membrane such as high-density polyethylene (HDPE).

### 2.1.2 Measuring Diffusion Using Membrane Uptake Experiments

Much of the initial data describing diffusion of hydrophobic organic compounds in HDPE was derived from membrane uptake experiments (19-22). The total mass of solute that has diffused into the membrane,  $M_t$ , has been derived for plane membranes with diffusion coming from both sides as a function of time (34):

$$\frac{M_t}{M_{eq}} = 1 - \sum_{n=0}^{\infty} \frac{8}{\pi^2 (2n+1)^2} e^{-\frac{D\pi^2 (2n+1)^2 t}{4L^2}} \quad (2-6)$$

where  $M_{eq}$  is the mass absorbed in the membrane at equilibrium, determined from  $H$ , the membrane volume ( $AL$ ), and the final aqueous concentration of the solute.

### 2.1.3 Diffusion Across Membranes with Aligned Impermeable Flakes

The addition of impermeable materials to barrier membranes and polymer coatings has been used as a means of reducing the effective solute diffusion coefficient (37-45). This effect is optimized when the impermeable flakes are aligned parallel to the membrane (normal to the direction of diffusion) (38). The addition of 10 vol% aligned impermeable flakes to poly(vinyl alcohol) (PVA) membranes reduced observed  $D$  by an order of magnitude in some experiments (41,46). The flakes improve the barrier properties of the membranes by reducing the effective cross-sectional area,  $A$ , available for diffusion and by increasing the tortuosity of the path a solute must use to diffuse from one side of the barrier to the other, as shown in Figure 2-3 (37). The latter effect introduces resistances associated with the constriction of solute “flow” through slits between two adjacent flakes and, more importantly, with “wiggles”, which ultimately



**Figure 2-3.** A model barrier membrane containing aligned impermeable flakes (37).

increase the effective diffusion path length,  $L$  (37,40). While aligned flakes are not used in the present work, the concept of increased tortuosity is explored in Chapter 3 with the use of an aqueous clay layer in sandwich membrane barriers.

## 2.2 Diffusion Across Active Membranes – Moving Reactive Front Model

### 2.2.1 Fast and Irreversible Reaction

Several models have been proposed to describe the effect of scavenger particle addition on membrane breakthrough curves. Yang et al. (47) described the effect on lag time when particles that react rapidly and irreversibly with diffusing solutes are added to membranes. Solute molecules that enter the membrane at the upstream surface are immediately consumed by reaction. The reactive particles are also consumed, allowing new solute molecules to diffuse deeper and advancing the “reactive front”, as shown in Figure 2-4.

When all of the scavenger particles are exhausted and the front reaches the downstream side of the membrane, solute breakthrough to the downstream reservoir is

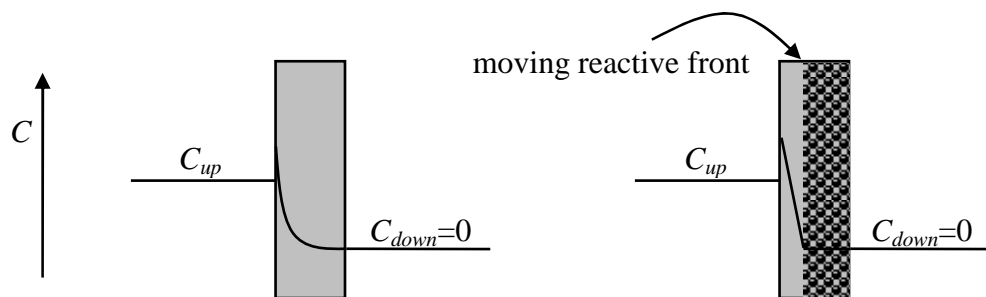


**Figure 2-4.** Concentration profiles in pure and reactive particle-containing membranes for  $t < t_{lag}$ .

observed. Yang et al. (47) estimated the lag time for reactive membranes by equating the consumption rate of the reactive particles to the flux of solute molecules toward the reactive front from the upstream reservoir:

$$t_{lag} = \frac{L^2 C_{s0}}{2\nu DHC_{up}} \quad (2-7)$$

where  $C_{s0}$  is the initial concentration of reactive particles present in the membrane and  $\nu$  describes the stoichiometry of the reaction. Unless the particles interfere with the diffusion or partitioning properties of the membrane, the steady-state flux is the same as that for a non-reactive membrane, and the breakthrough curve is estimated by combining Equations 2-7 and 2-3.

Shimotori et al. (28,30) applied Equation 2-7 and the concepts behind it to design a barrier membrane for hazardous waste landfill contaminants. Lag times of chromate,  $\text{Cu}^{2+}$ , carbon tetrachloride (CT), and other oxidized contaminants were increased 2 to 14-fold with the addition of  $\text{Fe}^0$  nanoparticles to PVA films (30). About 30% of the  $\text{Fe}^0$  successfully reduced CT before breakthrough—surface oxidation of the  $\text{Fe}^0$  nanoparticles likely slowed reaction rates with time, reducing the effectiveness of the particles before they could be completely consumed (30).  $\text{Fe}^0$  nanoparticles embedded in HDPE membranes also increased CT lag times, but only 2-3% of the  $\text{Fe}^0$  was actually consumed before breakthrough was observed (28). In HDPE, the reduced reaction efficiency may have been caused by insufficient concentrations of water necessary for the redox reaction with CT to occur. Diffusion of reaction products (chloroform (CF) for  $\text{Fe}^0$  reaction with CT) from membranes and back into the upstream and downstream reservoirs of a

breakthrough experiment has been modeled successfully using the moving reaction front concept (48).

### 2.2.2 Fast and “Irreversible” Sorption

Several methods have been developed to describe diffusion behavior of membranes containing scavengers that reversibly sorb diffusing solutes. Paul and others (49-53) developed a series of analytical “dual sorption” models to elucidate the difference between pure polymer uptake data, breakthrough data, and the theoretical curves described by Equations 2-2 through 2-5. Specifically, imperfections in polymer matrices were charged with the formation of “holes” within the barrier that have sorptive properties different than those of the bulk polymer. These “holes” were suspected of causing longer-than-expected lag times by trapping solute molecules according to the Langmuir isotherm (51-53):

$$q = \frac{q_{\max} b C}{1 + b C} \quad (2-8)$$

where  $q$  is the concentration of solute sorbed to the particles or “holes”,  $q_{\max}$  is the total capacity of the particles for solute sorption,  $C$  is the concentration of solute in solution, and  $b$  is a fitting parameter. A generic Langmuir isotherm curve is shown in Figure 2-5.

Warta et al. (54) presented a simplified model for the case of high upstream concentration well beyond the point where the sorbent’s capacity is reached. Although the model was originally derived for a generic sorbent or resin capacity, it has been modified below to specifically describe capacity in terms of the Langmuir isotherm

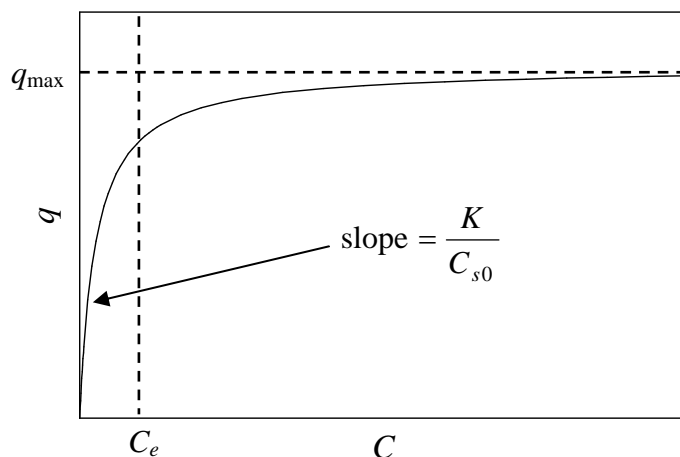


**Figure 2-5.** Schematic of a Langmuir isotherm curve.

parameter,  $q_{\max}$ :

$$t_{lag} = \frac{L^2 C_{s0} q_{\max}}{2DH(C_{up} - C_e)} \quad (2-9)$$

In Equation 2-9,  $C_e$  is the minimum equilibrium aqueous concentration at which  $q_{\max}$  is achieved, where the isotherm curve begins to flatten (54). Equation 2-9 predicts the lag time as if sorption were irreversible, because a high concentration front encountering the sorptive particles will quickly load the particles to capacity before diffusing further into the membrane. The driving force for sorption is approximated as  $C_{up} - C_e$ . Equation 2-9 was used successfully to describe observed lag times for cesium ion breakthrough of PVA membranes filled with 5 wt% crystalline silicotitanate, an ion-exchange resin. Lag times were extended by over an order-of-magnitude (54).

### 2.2.3 Increasing Reactive Membrane Lag Times with Aligned Flakes

Lape et al. (46) combined the concepts of reactive membranes for lag time extension with aligned flake-filled membranes to reduce the effective diffusion coefficient. The effect of both additives working together can be evaluated using Equation 2-7, which predicts that lag time is directly proportional to the concentration of reactive particles and indirectly proportional to  $D$ . Acid breakthrough experiments using PVA films containing mica flakes and zinc oxide nanoparticles confirmed their hypothesis (46).

### 2.2.4 Characterizing Leakage in Reactive Membranes

Several attempts have been made to characterize the effectiveness of scavenger-containing membranes by estimating the leakage of solute molecules through the membranes before the theoretical lag times predicted by Equations 2-7 and 2-9 (55-58). Leakage is typically attributed to slow reaction or sorption kinetics relative to the rate of diffusion through the membrane. Nuxoll and Cussler (55) used the second Damköhler number,  $\Phi$ , to describe the relative rates of reaction and diffusion:

$$\Phi = \frac{k_2 C_{s0} L^2}{D} \quad (2-10)$$

where  $k_2$  is the second-order rate constant for reaction (or sorption) between the particle and the solute. When  $\Phi$ , or the “reaction” rate divided by the diffusion rate, is high, behavior approaches that described in Equations 2-7 and 2-9. Lower  $\Phi$  values indicate a lower “reaction” rate relative to the rate of diffusion. When  $\Phi$  is low, therefore, there is a

greater chance that a solute molecule will be able to diffuse across the entire thickness of the membrane without “reacting”. Nuxoll and Cussler (55) use  $\Phi$  in tandem with the scavenger loading to predict leakage, or the total amount of solute that diffuses into the downstream reservoir before the theoretical lag time. The approaches of Siegel (57) and Solovyov and Goldman (58) also consider  $\Phi$  and/or the Thiele modulus in their derivations, which offer complex relationships that predict similar breakthrough curves.

### **2.3 Diffusion Across Active Membranes – Pseudo-First-Order Kinetics Model**

#### **2.3.1 Steady “Reaction” Model**

Diffusion across membranes with scavengers that slowly react or sorb solutes (relative to diffusion) can also be described by adapting Fick’s law to account for the transformation or immobilization of solute molecules. The “reaction”-diffusion equation for a membrane with pseudo-first-order kinetics is (34,35):

$$\frac{\partial C_m}{\partial t} = D \frac{\partial^2 C_m}{\partial x^2} - k_1 C_m \quad (2-11)$$

where  $k_1$  is the pseudo-first-order “reaction” rate constant in the membrane. Solving Equation 2-11 for the steady-state case gives a pseudo-steady-state concentration profile in the membrane (35):

$$\frac{C_m}{C_{up}} = \frac{H \sinh\left((L-x)\sqrt{\frac{k_1}{D}}\right)}{\sinh\left(L\sqrt{\frac{k_1}{D}}\right)} \quad (2-12)$$

Equation 2-12 has been used to predict oxygen diffusion across scavenger-containing packaging materials (3) and to calculate rate constants for oxygen scavenging reactions (59).

The term pseudo-steady-state indicates that the steady-state solution of the steady “reaction” model is an intermediate value—the derivation assumes an infinite capacity of the scavenger for the diffusing solute. In reality, the scavenger slows diffusion by intercepting and transforming or immobilizing solute molecules within the membrane. When the particles are exhausted or saturated, flux across the membrane will proceed as if across a pure polymer as described by Equation 2-5.

### 2.3.2 Diffusion-Limited Kinetics Model

When particle concentrations within the membrane are low, diffusion from the bulk membrane to the particle surface may limit the kinetics of reaction or sorption. The “reaction” rate can be described using the steady-state Fick’s law expression for diffusion toward spherical particles as described by Ferrari et al. (5):

$$\frac{d}{dr} \left( r^2 \frac{dC_m}{dr} \right) = 0 \quad (2-13)$$

where  $r$  is the direction of diffusion. Equation 2-13 is solved using the boundary conditions:

$$\begin{aligned} \text{at } r = R, C_m &= 0 \\ \text{at } r = S, C_m &= C_m(x, t) \end{aligned} \quad (2-14)$$

$C_m(x, t)$  is the concentration of solute in the membrane at a given depth  $x$  and time  $t$ ,  $R$  is

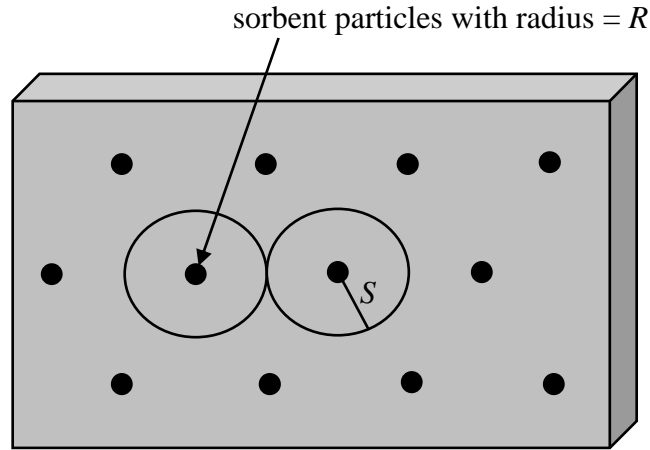


**Figure 2-6.** Unit cell for diffusion toward a membrane-bound particle.

the radius of the particle,  $S$  is the radius of diffusion around the particle defined by:

$$\phi = \frac{R^3}{S^3} \quad (2-15)$$

where  $\phi$  is the volume fraction of particles in the membrane. Figure 2-6 describes the radius of diffusion,  $S$ , schematically.

Combining Equations 2-13 through 2-15 gives a steady-state concentration profile around a single particle:

$$C_m = \frac{C_m(x,t)}{1 - \phi^{1/3}} \left(1 - \frac{R}{r}\right) \quad (2-16)$$

The flux of solute molecules toward the particle surface is:

$$j|_{r=R} = D \frac{dC_m}{dr} \Big|_{r=R} = \frac{DC_m(x,t)}{\left(1 - \phi^{1/3}\right)} \left(\frac{1}{R}\right) \quad (2-17)$$

The pseudo-first-order diffusion-limited “reaction” rate constant,  $k_1$ , is directly

proportional to the steady-state flux of solute molecules toward the particles:

$$k_1 = \frac{j|_{r=R}}{C_m(x,t)} \cdot \frac{\text{spherical particle surface area}}{\text{unit cell membrane volume}} \quad (2-18)$$

which reduces to:

$$k_1 = \frac{3D}{R^2 \left(1 - \phi^{1/3}\right) \left(\frac{1}{\phi} - 1\right)} \quad (2-19)$$

when combined with the steady-state flux given in Equation 2-17. Equations 2-12 and 2-19 can be combined to predict concentrations and flux across a scavenger-containing membrane when reaction or sorption is diffusion-limited. The form of Equation 2-19 is similar to that derived previously for particles in a cubic unit cell (60).

#### **2.4 Diffusion Across Active Membranes – Fast Equilibrium Model**

Equilibrium reaction or sorption slows diffusion across membranes until the scavenger establishes equilibrium with the upstream reservoir. For example when the dissolved upstream concentration is below  $C_e$  (Figure 2-5), equilibrium sorption is simplified from the Langmuir isotherm equation to a linear function:

$$q = q_{\max} bC \quad (2-20)$$

Diffusion across a membrane containing sorbent particles is described by equating the rate of solute loss in the membrane to the rate of sorption (34):

$$\frac{\partial C_m}{\partial t} = D \frac{\partial^2 C_m}{\partial x^2} - C_{s0} \frac{\partial q}{\partial t} \quad (2-21)$$

Equation 2-21 can be rearranged using a dimensionless equilibrium constant describing the relative concentrations of dissolved and sorbed solute in the membrane,  $K$ :

$$K = \frac{qC_{s0}}{C_m} = \frac{q_{\max}bC_{s0}}{H} \quad (2-22)$$

Equations 2-21 and 2-22 reduce to (34):

$$\frac{\partial C_m}{\partial t} = \frac{D}{1+K} \frac{\partial^2 C_m}{\partial t^2} \quad (2-23)$$

Equation 2-23 mimics Fick's second law (Equation 1) but with an effectively reduced diffusion coefficient (34,47):

$$D_{\text{effective}} = \frac{D}{(1+K)} \quad (2-24)$$

and  $t_{lag}$  becomes (47):

$$t_{lag} = \frac{L^2}{6D}(1+K) \quad (2-25)$$

Equation 2-2 predicts the initial curvature of breakthrough curves if  $D$  is replaced with  $D_{\text{effective}}$  (47). After equilibrium is established, flux across the membrane is again equal to that expected for the pure polymer (Equation 2-5).

## 2.5 Active Membrane Models Summary

Table 2-1 provides a summary of lag times and pseudo-steady-state flux expressions that can be used to estimate diffusion behavior in reactive and sorptive scavenger-containing membranes.

**Table 2-1.** Assumptions and relationships of breakthrough curve models for membranes with reactive or sorptive scavengers

	$t_{lag}$	Pseudo-Steady-State $j$
<b>model 0</b> pure polymer (34-36)	$\frac{L^2}{6D}$	$\frac{DHC_{up}}{L}$
<b>model 1</b> fast, irreversible reaction or sorption (moving reactive front model) (47)	$\frac{L^2 C_{s0} q_{max}}{2DH(C_{up} - C_e)}$	$\frac{DHC_{up}}{L}$
<b>model 2</b> pseudo-first-order kinetics (34,35)	n/a	$\frac{HC_{up} \sqrt{k_1 D}}{\sinh\left(L \sqrt{\frac{k_1}{D}}\right)}$
<b>model 3</b> fast equilibrium kinetics (34,47)	$\frac{L^2(1+K)}{6D}$	$\frac{DHC_{up}}{L}$

## 2.6 Composite Membranes

The expressions presented above describe diffusion across single-layer membranes. Layered membrane systems have been proposed in a variety of applications for their ability to provide a complete barrier that takes advantage of the positive aspects of each layer. For example, Saito and Nakagawa (61) recently proposed an organic/silica nanocomposite-coated PVA membrane to combine the effective gas barrier properties of dry PVA with the exceptional water vapor barrier properties of the coating.

The solute permeability and lag time of composite (multi-layer) membranes are defined using the properties of each individual layer and a sum of resistances relationship (62,63). For an A-B-A sandwich membrane:

$$\frac{L_{composite}}{P_{composite}} = \frac{L_{A1} + L_{A2}}{P_A} + \frac{L_B}{P_B} \quad (2-26)$$

and

$$t_{lag} = \frac{\left[ \frac{L_{A1}^2}{D_A} \left( \frac{L_{A1} + 3L_{A2}}{6P_A} + \frac{L_B}{2P_B} \right) + \frac{L_B^2}{D_B} \left( \frac{L_{A1} + L_{A2}}{2P_A} + \frac{L_B}{6P_B} \right) \right] + \frac{L_{A2}^2}{D_A} \left( \frac{3L_{A1} + L_{A2}}{6P_A} + \frac{L_B}{2P_B} \right) + \frac{L_{A1}L_B L_{A2}}{P_A^2}}{\frac{L_{A1} + L_{A2}}{P_A} + \frac{L_B}{P_B}} \quad (2-27)$$

where  $L_{A1}$  and  $L_{A2}$  are the thicknesses of the two A layers,  $L_B$  is the thickness of the center B layer,  $P_A$  and  $D_A$  are the permeability and diffusion coefficient of the solute in material A, and  $P_B$  and  $D_B$  are the permeability and diffusion coefficient of the solute in material B. For a two-layer A-B composite membrane,  $L_{A2}=0$ .

Mayer et al. (64) used the sandwich membrane concept to measure diffusion coefficients in liquid media by sandwiching the liquid between two membranes. An aqueous B layer can be modeled as a membrane, because transport is limited to diffusion. When the center layer of a sandwich membrane is water,  $H_B = 1$  and  $D_B = P_B$ .

Composite membranes with active layers may be designed to optimize the effect of the scavenger addition. Nuxoll et al. (65) studied how scavenger location affects breakthrough by modeling a zinc oxide-containing PVA membrane as a two-layer system with homogeneous permeability. The zinc oxide was concentrated on one side of the membrane due to settling in during the membrane preparation process. They found that locating the reactive material downstream (in the B layer of an A-B membrane) extended lag times to acid breakthrough to a greater extent than locating it upstream. Solovyov and Goldman (66,67) developed a method to predict scavenger “exhaustion times” for A-B

membranes where the A layer contains reactive material and the two layers have different permeabilities.

## ***2.7 Membranes and Reactive Membranes for Non-Barrier Use***

This summary would not be complete without the mention of several recent non-barrier applications for membranes and reactive membranes by environmental engineers. Accumulation of hydrophobic compounds by hydrophobic polymers has attracted the attention of researchers in the environmental monitoring arena. The use of semi-permeable membrane devices (triolein-filled low-density polyethylene (LDPE) tubes designed to mimic passive accumulation of hydrophobic contaminants in the lipids of aquatic species) relies on the easy diffusion of contaminants through LDPE (68-72). More recently, polyethylene devices (strips of LDPE often deployed beneath surface sediments) have been used to quantify sediment porewater concentrations of polychlorinated biphenyls (PCBs) and polyaromatic hydrocarbons (73-77). The uptake of hazardous hydrophobic organic compounds by polyethylenes and other polymers has also raised concerns by those in the packaging and recycling industries (78-81).

In some cases, the incorporation of reactive materials into polymer matrices may improve reaction performance. Xu, Bhattacharyya, and others (82-86) have prepared polymer-bound Fe<sup>0</sup>, iron-nickel, and iron-palladium particles and observed efficient degradation of trichloroethylene (TCE) and PCBs. Embedding these particles into microfiltration membranes helps reduce particle loss, prevent particle agglomeration, and can be used in simultaneous reaction/filtration operations during water treatment (82).

Others have immobilized enzymes and bacteria in membranes and hydrogels for biosensing, sequestering, or degrading aqueous pollutants (87-90).

## **Chapter 3**

### **Sorptive and Reactive Scavenger-Containing Sandwich Membranes as Contaminant Barriers<sup>†</sup>**

<sup>†</sup> Reproduced in part with permission from “Surdo, E.M.; Cussler, E.L.; Arnold, W.A. Sorptive and reactive scavenger-containing sandwich membranes as contaminant barriers. *Journal of Environmental Engineering*, 2009, 135, 69-76.” Copyright 2009 American Society of Civil Engineers.

### **3.1 Introduction**

To prevent the migration of hazardous chemicals from landfills to the surrounding environment, many landfill liner systems use high-density polyethylene (HDPE) geomembranes in tandem with a compacted clay liner (6-9). When intact, geomembrane liners are effective in keeping water and heavy metals from leaking into the groundwater below the landfill (9). Hydrophobic compounds, however, can partition into and diffuse through HDPE (19-26,28). Chlorinated solvent transport in compacted clay has also been measured (91,92), and Foose et al. (8) used data from laboratory tests on several materials to predict transport rates through composite liners. In some cases, they predicted that contaminant transport via diffusion would be more significant than advective transport via defects in the geomembrane (8,18).

Many of the chlorinated solvents that diffuse readily through HDPE and composite liners are considered hazardous to the environment and to public health and are listed as priority pollutants by the U.S. Environmental Protection Agency (93,94). Baun et al. (95) showed that the dissolved organic contingent of a leachate plume in a Denmark aquifer was toxic to algae up to 80 m away from the landfill.

$\text{Fe}^0$  is an inexpensive, non-hazardous reducing agent used in the remediation of plumes containing chlorinated compounds such as carbon tetrachloride (CT) and trichloroethylene (TCE) (96-104). Increased reaction rates for CT, TCE, and other chlorinated organic compounds using nano-sized  $\text{Fe}^0$  particles has been attributed to the high specific surface area associated with these particles (102-107).  $\text{Fe}^0$  nanoparticles have also been used to reduce perchlorate and nitrate in laboratory tests (108-110) and

have been proposed for the treatment of biosolids for the reduction of odorous compounds (111). Xu and Bhattacharyya (82,84) have measured TCE reduction with Fe<sup>0</sup> and bimetallic nanoparticles embedded in microfiltration membranes designed for water treatment, citing benefits such as reductions in particle loss and agglomeration to membrane immobilization of the particles.

Shimotori et al. (28) immobilized Fe<sup>0</sup> nanoparticles directly in HDPE, resulting in a reactive membrane in which CT was reduced as it diffused through the geomembrane barrier. Bartelt-Hunt et al. (112) studied the addition of sorptive amendments to compacted clay to slow the transport of hydrophobic chemicals from landfills. This research combines these two concepts by using Fe<sup>0</sup> nanoparticles or powdered activated carbon (PAC) as reactive or sorptive contaminant scavengers in composite “sandwich” membranes. Sandwich membranes are prepared by incorporating scavengers into an aqueous clay “paste” sandwiched between two sheets of HDPE. The clay provides a physical support system for the scavengers in the center layer, helps keep them homogeneously dispersed (113), and may reduce the apparent diffusion coefficient of contaminants in the center layer of the composite.

PAC-containing sandwich membranes were tested using TCE as a model contaminant. To compare the performance of PAC with the previously-proposed Fe<sup>0</sup> reactive scavenger, sandwich membranes containing Fe<sup>0</sup> nanoparticles were also tested. The results from these sandwich membrane experiments are compared with those reported previously for single-layer reactive membranes containing Fe<sup>0</sup> (28).

### **3.2 Experimental Methodology**

#### **3.2.1 Preparation of Fe<sup>0</sup> Nanoparticles**

Fe<sup>0</sup> nanoparticles were prepared using a method adapted from Liu et al. (103). All solutions were deoxygenated by sparging with argon for no less than one hour. Ten grams of ferrous sulfate heptahydrate (99%, Fisher) were dissolved in 540 mL of a 35 vol% deoxygenated methanol (99.9% Mallinckrodt)/65 vol% deoxygenated nanopure water (Milli-Q, Millipore) solution inside an anaerobic glove bag (7% H<sub>2</sub>/93% N<sub>2</sub>, Coy Laboratory Products). The pH was adjusted from 4.3 to 7.5 with deoxygenated 5 M sodium hydroxide (98%, Sigma-Aldrich). Twenty-five milliliters of a 2 M sodium borohydride solution (96%, Mallinckrodt), prepared in the glove bag using deoxygenated nanopure water, were added 400 μL at a time to the ferrous sulfate solution while stirring. After 20 minutes, the particles were allowed to settle for one hour. After the liquid was decanted, the particles were centrifuged in sealed plastic tubes for 10 minutes at 5,000 rpm. The particles were rinsed with deoxygenated methanol three times, centrifuged after each rinse, and dried at 100 °C under argon for approximately one hour. After drying, the particles were immediately transferred to the glove bag where agglomerations of particles were separated using a mortar and pestle. The resulting powder was sealed and stored in the glove bag.

#### **3.2.2 Preparation of Composite Membranes**

Typical commercially-available HDPE geomembranes have thicknesses on the order of millimeters. To expedite experiments, pure high-density polyethylene beads

(DOWLEX IP-40, Dow) were pressed with 3300-6700 N force at 160 °C to films with thicknesses ranging from 100 to 400  $\mu\text{m}$  using a Wabash hot press (Wabash Metal Products). Membrane thicknesses were measured using a micrometer (Mitutoyo). The center layer of the membrane was prepared by combining kaolin clay (Ridel-de Haën) and nanopure water to achieve a paste with a peanut butter-like texture. Ion effects associated with other clays, such as bentonite, have the potential to interfere with the reaction of  $\text{Fe}^0$  with CT or TCE. Kaolin clay was chosen for this study as an inert physical support for scavenger particles in the sandwich membranes. The solids volume fraction in the paste was 0.40 for all experiments. The membranes were assembled using a polytetrafluoroethylene (PTFE) spacer to control the thickness of the center layer, as shown in Figure 3-1. Layers were glued together and fixed between the upstream and downstream breakthrough experiment diaphragm cells with epoxy (Quick Set, Loctite). The PAC (J.T. Baker) was combined with clay and nanopure water all at once, except in two experiments. In the experiment using 12 wt% (194 g/L) PAC in the center layer, the PAC was combined with water and allowed to sit in an airtight container for

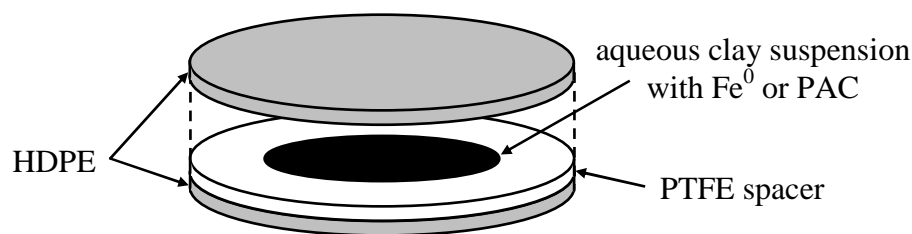


**Figure 3-1.** Composite membrane assembly. An aqueous clay suspension (solids volume fraction = 0.40) containing reactive scavengers, such as  $\text{Fe}^0$  nanoparticles, or sorptive scavengers, such as PAC, is sandwiched between two sheets of HDPE.

approximately 6 hours to allow water to diffuse into the pores of the PAC before the clay was added. In the experiment where 24 wt% (357 g/L) was used, the water and PAC were equilibrated overnight. For experiments using Fe<sup>0</sup> nanoparticles, a deoxygenated 50 mM Tris buffer with a pH of approximately 7.2 (7.88 g/L Tris[hydroxymethyl]aminomethane hydrochloride: 99%; 0.35 g/L NaOH: 50-52%, Titristar; 5.85 g/L NaCl: 100.0%, Mallinckrodt) was used instead of nanopure water.

### 3.2.3 Breakthrough Experiments

Diaphragm cells (Figure 3-2) were used to measure membrane lag times and permeabilities as described previously (28,30). The membrane cross-sectional area was

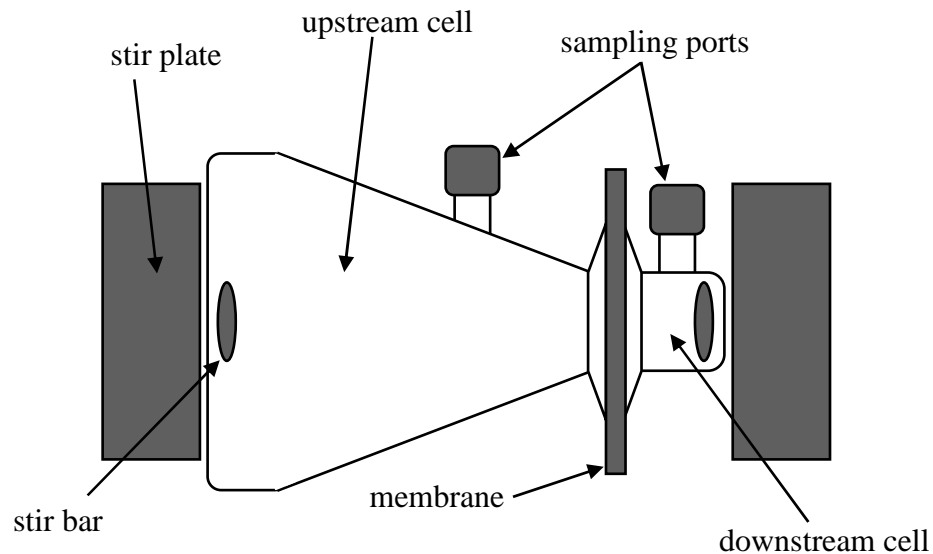


**Figure 3-2.** Diaphragm cell apparatus for measuring solute breakthrough across membranes. The upstream cell is spiked with a concentrated solute stock solution to begin each breakthrough experiment.

5.07 cm<sup>2</sup>. The upstream and downstream cell volumes were initially filled with deoxygenated pH 7.2 50 mM Tris buffer in experiments using Fe<sup>0</sup> as the scavenger or nanopure water when PAC was the scavenger. To start an experiment, a methanolic solution of either CT (99.9%, Sigma-Aldrich) or TCE (reagent grade, Fisher) was injected into the upstream cell to achieve the desired upstream concentration (2000 μM for CT or 4000 μM for TCE). Methanol concentrations were less than 1 vol% in the upstream cell.

#### *3.2.4 Batch Experiments*

Reaction rates of the prepared Fe<sup>0</sup> nanoparticles with each of the two model contaminants were measured in 120-mL headspace-free batch reactors. Each reactor initially contained 0.15 g of the Fe<sup>0</sup> nanoparticles and either 100 μM CT or 400 μM TCE in deoxygenated pH 7.2 50 mM Tris buffer. Reactors were sampled every 15-20 minutes at the start of each experiment, tapering in frequency until t = 50 hours. A single CT reactor was used to confirm the rapid reaction rate of CT with Fe<sup>0</sup>. The formation and degradation of chloroform (CF), a CT reduction intermediate, was also monitored throughout this experiment. The TCE degradation rate experiment was run in quadruplicate.

The PAC sorption isotherm for TCE was determined using a series of 38-mL serum bottles loaded with 0.01 to 1.4 g of PAC and filled with water. The initial aqueous TCE concentration was 5000 μM. After 8 days, samples of the aqueous phase were collected

and analyzed for concentrations of TCE. To ensure the vials had achieved equilibrium, additional samples were collected after 20 and 41 days of equilibration.

### *3.2.5 Sample Extraction and Analysis*

Ten-microliter aqueous samples were collected throughout each experiment. For experiments using CT as the model contaminant, samples were extracted into 1 mL of pentane containing TCE (~15  $\mu\text{M}$ ) as an internal standard in a 2-mL autosampler vial by vortex mixing for 30 seconds (Touch Mixer 232, Fisher Scientific). Samples from experiments using TCE as the model contaminant were extracted into 1 mL of pentane containing ~0.2  $\mu\text{M}$  CT as an internal standard. Extracted samples were analyzed to quantify concentrations of CT, TCE, and CF using a ThermoQuest Trace GC with an electron capture detector (oven temperature at 40 °C for 5 min, 10 °C/min to 120 °C, 30 °C/min to 240 °C, hold at 240 °C for 1 min; detector temperature of 270 °C). A 1.5- $\mu\text{L}$  aliquot of the extract was injected directly onto a J&W DB-1 column (30 m  $\times$  0.32 mm i.d.  $\times$  5  $\mu\text{m}$  film thickness). Calibration was accomplished by preparing 6 to 10 aqueous standards of CT, TCE, or CF (99.9%, Sigma) and sampling and extracting as described above.

## **3.3 Results and Discussion**

### *3.3.1 CT Containment Using Sandwich Membranes*

Experiments using CT and  $\text{Fe}^0$ -containing sandwich membranes allow us to compare sandwich membranes directly to the single-layer poly(vinyl alcohol) (PVA) and

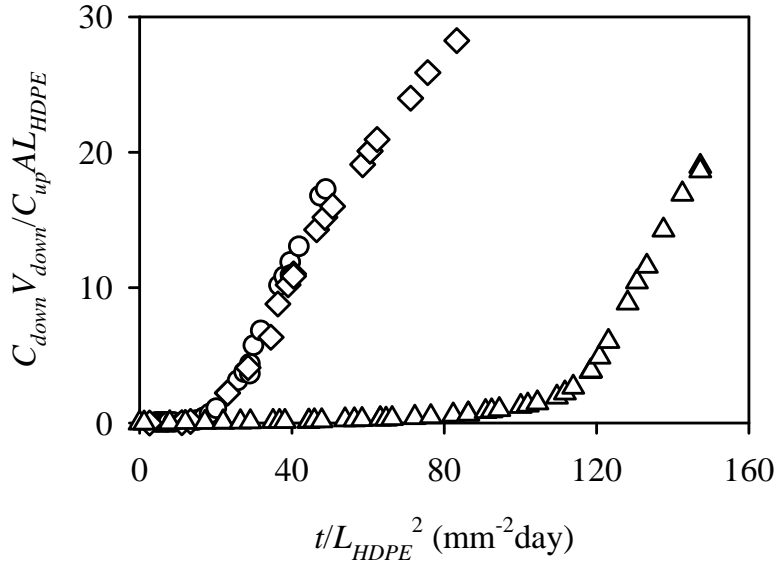


**Figure 3-3.** Normalized CT breakthrough curves for a pure HDPE membrane ( $\circ$ ), a non-reactive composite membrane ( $\square$ ), and a composite containing 1.8 wt%  $\text{Fe}^0$  nanoparticles in the center layer ( $\triangle$ ).

HDPE reactive membranes studied previously (28,30). Observed breakthrough curves for CT in a single HDPE membrane, a non-reactive sandwich membrane, and a sandwich membrane containing 1.8 wt%  $\text{Fe}^0$  nanoparticles in the center layer are shown in Figure 3-3. The axes of Figure 3-3 are based on Equation 3-1, a rearranged version of the linear breakthrough expression, Equation 2-3.

$$\frac{C_{down}}{C_{up}} = \frac{DHA}{LV_{down}} (t - t_{lag}) \quad (2-3)$$

$$\frac{C_{down} V_{down}}{C_{up} AL} = \frac{P}{L^2} (t - t_{lag}) \quad (3-1)$$

The dimensionless number on the left-hand side of Equation 3-1 is a normalized form of  $C_{down}$ . When plotted against  $t/L^2$ , a normalized time variable, breakthrough experiments can be compared to one another directly, regardless of variation in membrane thickness. The slope of each curve after the lag is equivalent to  $P$ , the permeability of CT in the membrane. The permeability of CT in a single HDPE layer observed in this study is similar to that reported by Shimotori et al. (28).

The plot axes in Figure 3-3 use as a thickness,  $L$ , the sum of the thicknesses of only the HDPE layers,  $L_{HDPE}$ . This technique approximates the composite membrane as an HDPE membrane with an infinitely-thin center layer that does not contribute to the lag time or the overall permeability of the composite by neglecting the second term on the right-hand side of Equation 2-26.

$$\frac{L_{composite}}{P_{composite}} = \frac{L_{A1} + L_{A2}}{P_A} + \frac{L_B}{P_B} \quad (2-26)$$

The quality of this estimate is apparent in looking at the nearly identical curves for a single layer of pure HDPE and for a non-reactive composite shown in Figure 3-3. If the center layer of the sandwich membrane contributed significantly to the overall resistance of the barrier to CT diffusion, the slope of the sandwich membrane breakthrough curve would be reduced when  $L_{HDPE}$  is used in the axes of Figure 3-3.

Consumption of diffusing CT by reaction with  $Fe^0$ , even with the addition of only 1.8 wt%  $Fe^0$  to the center layer of the sandwich membrane, extended the lag time of the composite considerably (5-fold). Like the  $Fe^0$ -containing membranes described previously (28,30), however, only a percentage of the reactive scavenger was consumed

before breakthrough of CT to the downstream cell. Effective concentrations were back-calculated from observed lag times using Equation 2-7, a technique proposed by Shimotori et al. (30) for analyzing the effectiveness of scavengers in reactive membranes.

$$t_{lag} = \frac{L^2 C_{s0}}{2\nu DHC_{up}} \quad (2-7)$$

Effective scavenger concentrations were corrected for imperfect centering of the scavenger-containing layer as described by Nuxoll et al. (65). In this study, the effective Fe<sup>0</sup> concentration was approximately 30% of the actual C<sub>s0</sub>, a major improvement over the 2-3% observed for a single HDPE layer containing Fe<sup>0</sup> nanoparticles (28), but comparable with that observed for Fe<sup>0</sup>-containing PVA membranes (30). PVA membranes contain approximately 50% water by volume when hydrated. The fact that the composite membrane's aqueous center layer achieved more Fe<sup>0</sup> consumption before CT breakthrough supports the hypothesis that a lack of water in the single-layer HDPE membranes limited the reaction between Fe<sup>0</sup> and CT (28). The limit of 30% usage in both the PVA and the sandwich membrane is likely related to a decrease in reaction rate as oxides form on the surface of the Fe<sup>0</sup> nanoparticles (114-116).

### 3.3.2 Fe<sup>0</sup>-Containing Sandwich Membranes for TCE Containment

Replicate normalized breakthrough curves for TCE in a single HDPE layer are shown in Figure 3-4. The curves observed in these experiments are reproducible. The average permeability, equal to the slope of the normalized breakthrough curve, agrees with values reported previously (24,25).

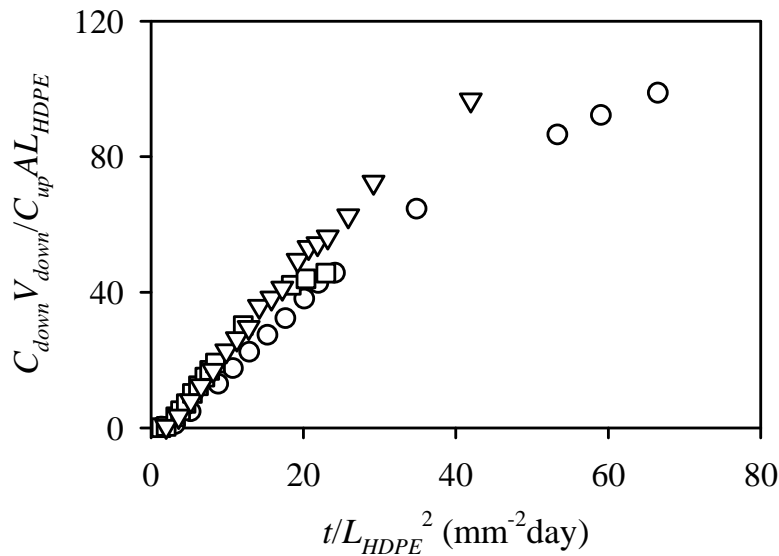


**Figure 3-4.** Replicate normalized breakthrough curves for TCE using single-layer HDPE membranes.

Table 3-1 provides a summary of the experimental conditions and results obtained from TCE breakthrough experiments using single HDPE membranes and non-reactive composites. The resistance of the HDPE layers was subtracted from the composite membrane resistance to calculate the permeability of the clay suspension layer for non-reactive composites,  $P_B$ , using Equation 2-26. Water-saturated cores of compacted clay liners collected from landfills in Wisconsin and Ontario show apparent diffusion coefficients of TCE of  $4 \times 10^{-10} \text{ m}^2/\text{s}$  and  $5 \times 10^{-12} \text{ m}^2/\text{s}$ , respectively (91,92), and the clay layer permeabilities observed in replicate scavenger-free sandwich membrane experiments reproducibly fall within this range. Batch equilibrium experiments confirmed that the kaolin clay used in this study did not sorb TCE ( $H_B = 1$ ).

**Table 3-1.** Summary of non-reactive TCE breakthrough experiments

$C_{up}$ ( $\mu\text{M}$ )	$L_{A1}$ <sup>a</sup> ( $\mu\text{m}$ )	$L_B$ <sup>b</sup> ( $\mu\text{m}$ )	$L_{A2}$ ( $\mu\text{m}$ )	$P_{composite}$ <sup>c</sup> ( $\text{m}^2/\text{s}$ )	$P_B$ <sup>d</sup> ( $\text{m}^2/\text{s}$ )	$t_{lag}$ (hr)
4851	134	-	-	$2.6 \times 10^{-11}$	-	1
5056	230	-	-	$3.6 \times 10^{-11}$	-	3
4430	117	-	-	$3.3 \times 10^{-11}$	-	1
3543	169	384	222	$1.9 \times 10^{-11}$	$1.4 \times 10^{-11}$	14
3848	185	385	175	$1.9 \times 10^{-11}$	$1.4 \times 10^{-11}$	15

<sup>a</sup>  $L_{A1}$  is the upstream membrane thickness for composite membranes or the total thickness for single-layer HDPE membranes.

<sup>b</sup>  $L_{A2}$  is the downstream membrane thickness for composite membranes.

<sup>c</sup>  $P_{composite}$  is the apparent permeability for composites or the HDPE permeability for single-layer membranes.

<sup>d</sup>  $P_B$  is the center layer permeability of an ABA composite membrane.

$\text{Fe}^0$ -containing sandwich membranes were unsuccessful in extending the lag time to TCE breakthrough beyond that of the membrane's non-reactive counterpart, as shown in Figure 3-5. Figure 3-5 includes data from  $\text{Fe}^0$ -containing sandwich membrane experiments and the breakthrough curve predicted for a non-reactive sandwich membrane based on the baseline permeabilities given in Table 3-1 and on a sandwich membrane with dimensions that are the average of the reactive membranes tested. We suspect that the slower reaction of  $\text{Fe}^0$  with TCE is primarily responsible for the failure of the  $\text{Fe}^0$  nanoparticles to increase the lag time to the extent that was observed for CT. Batch experiments resulted in second-order reaction rate constants,  $k_2$ , of  $0.0019 \pm 0.0002$  and  $0.2 \pm 0.1 \text{ M}^{-1}\text{s}^{-1}$  for TCE and CT, respectively. The TCE value lies within the range of  $0.0016 \text{ M}^{-1}\text{s}^{-1}$  to  $0.0082 \text{ M}^{-1}\text{s}^{-1}$  reported previously for reaction of with fresh and oxygen-stabilized particles, respectively (103,117). Wang and Zhang (117) and Liu et al. (103)

reported Brunauer-Emmett-Teller (BET) specific surface areas for the  $\text{Fe}^0$  nanoparticles used in their studies of 33.5 and 36.5  $\text{m}^2/\text{g}$ , respectively.

To compensate for the slow reaction, Damköhler numbers (defined in Equation 2-10) were raised by increasing the  $\text{Fe}^0$  concentration, increasing the thickness of the center layer, or both.

$$\Phi = \frac{k_2 C_{s0} L^2}{D} \quad (2-10)$$

Although a few experiments were designed to have Damköhler numbers that equaled or exceeded that of the successful experiment using  $\text{Fe}^0$  and CT, an increase in the lag time due to the presence of  $\text{Fe}^0$  was not observed. There are a few potential reasons for the failure of these experiments. When  $\text{Fe}^0$  concentrations were increased in the sandwich

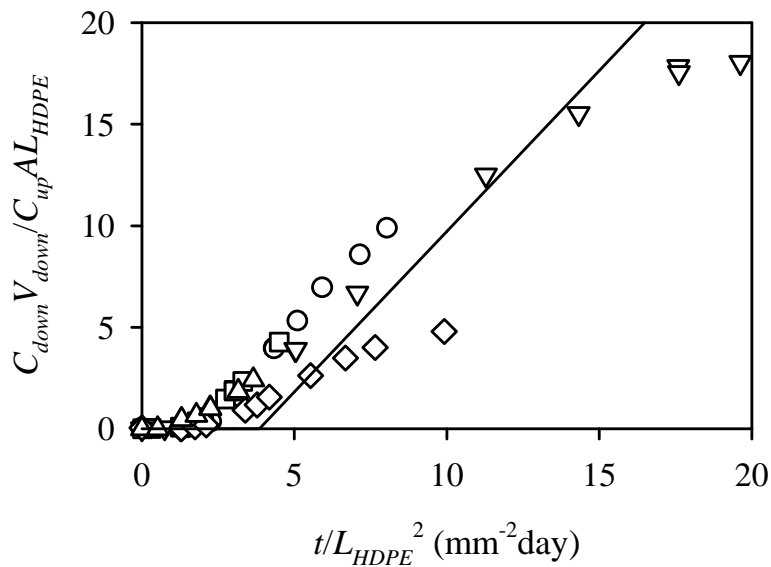


**Figure 3-5.** Normalized TCE breakthrough curves for sandwich membranes containing  $\text{Fe}^0$  nanoparticles and a predicted breakthrough curve for a non-reactive sandwich membrane with average dimensions (—).

membrane's center layer, the consistency of the clay-Fe<sup>0</sup>-water "paste" changed dramatically. Cracks in the center layer may have been more likely in the grainy high-Fe<sup>0</sup> mixture, providing a means for the TCE to shuttle across the membrane's center layer without reacting. Alternatively, the reaction chemistry in the center layer of the sandwich membrane may be complicated by surface dynamics not present in the batch reactors, reducing  $k_2$  within the membrane. The surface reaction of Fe<sup>0</sup> with TCE has previously been described using a Langmuir-Hinshelwood-Hougen-Watson model in which reduction occurs at a finite number of surface reaction sites and is limited by the reaction rate (101). This model implies that, at the high concentrations of TCE used in these experiments, the reactive sites on the Fe<sup>0</sup> nanoparticles at the "reactive front" moving across the center layer may be saturated with TCE molecules, allowing dissolved TCE to diffuse past the Fe<sup>0</sup> particles before reaction occurs.

### 3.3.3 PAC-Containing Sandwich Membranes for TCE Containment

TCE breakthrough curves for experiments using non-reactive and PAC-containing sandwich membranes are compared in Figure 3-6. Like Figure 3-3, the axes of Figure 3-6 use only the thicknesses of the HDPE layers in the sandwich membrane as  $L$ . Because TCE diffuses more quickly through HDPE, however, the resistance of the HDPE layers do not dominate as they do for CT. As a result, the slope of the sandwich membrane curve is lower than that for the single HDPE membrane. Regardless, it is easy to conclude in looking at Figure 3-6 that the PAC extends the lag time of the barrier beyond that of either non-reactive barrier. Breakthrough curves observed from experiments using

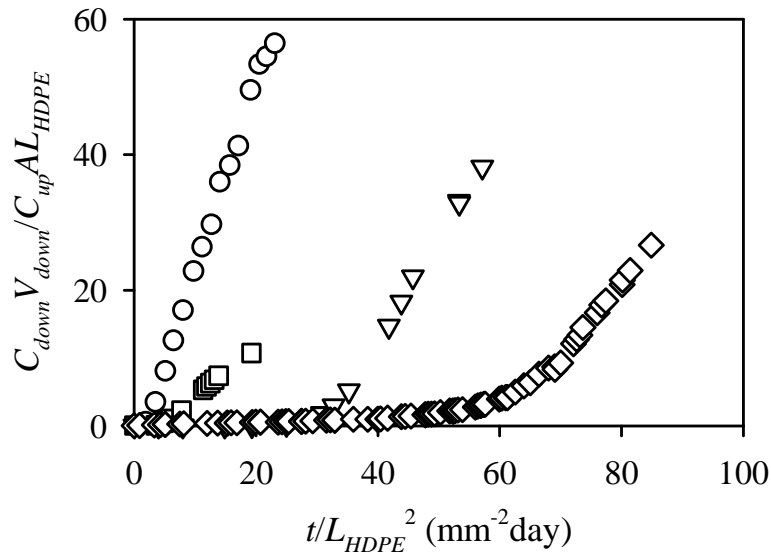


**Figure 3-6.** Normalized TCE breakthrough curves for a pure HDPE membrane ( $\circ$ ), a non-reactive composite membrane ( $\square$ ), a composite membrane with 12 wt% PAC in the aqueous clay suspension sandwiched between two layers of HDPE ( $\nabla$ ), and a composite membrane with 24 wt% PAC in the center layer ( $\diamond$ ).

12 wt% and 24 wt% PAC in the center layer of sandwich membranes, which are also shown in Figure 3-6, exhibit sizable increases in the lag time compared with the non-reactive barriers. The sorptive scavenger, PAC, produces a lag-time lengthening effect much like that expected for a reactive scavenger.

Batch equilibrium experiments yielded the isotherm for TCE sorption to PAC shown in Figure 3-7, which fits a Langmuir isotherm (Equation 2-8) with  $q_{max}=3000$   $\mu\text{mol/g}$  and  $b=0.0085$   $\mu\text{M}^{-1}$ .

$$q = \frac{q_{max} b C}{1 + b C} \quad (2-8)$$

This isotherm is comparable to those reported previously for TCE sorption to granulated activated carbon (112,118). For the high upstream concentrations used to test the PAC-containing membranes described in Table 3-2,  $\nu$  is equivalent to  $1/q_{max}$ , as defined in Equation 2-9.

$$t_{lag} = \frac{L^2 C_{s0} q_{max}}{2DH(C_{up} - C_e)} \quad (2-9)$$

The value of  $C_e$  is 117  $\mu\text{M}$ , the aqueous concentration at which the maximum sorption capacity is reached (54).

Like experiments using  $\text{Fe}^0$  nanoparticles, the PAC was not used to its fullest capacity before contaminant breakthrough. Table 3-2 lists the effective PAC concentration as a percentage of the actual concentration present in the center layer of the

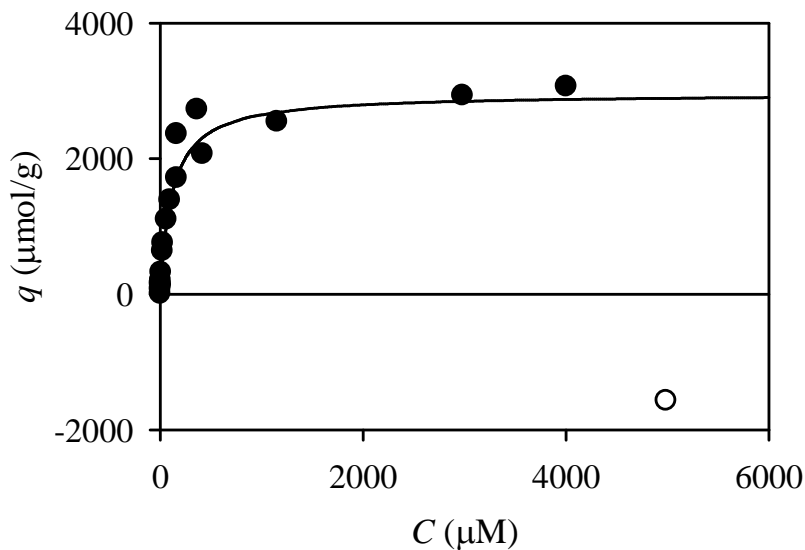


**Figure 3-7.** Equilibrium sorption data for aqueous TCE sorption to PAC (●) and a non-linear fit using the Langmuir isotherm model (—). Open symbols represent data that were omitted from the Langmuir fitting data set.

**Table 3-2.** Summary of PAC-containing composite membrane breakthrough experiments using TCE

$C_{up}$ ( $\mu\text{M}$ )	$L_{A1}$ ( $\mu\text{m}$ )	$L_B$ ( $\mu\text{m}$ )	$L_{A2}$ ( $\mu\text{m}$ )	$C_{s0}^a$ (g/L)	$P_{composite}$ ( $\text{m}^2/\text{s}$ )	$P_B$ ( $\text{m}^2/\text{s}$ )	Observed $t_{lag}$ (hr)	Expected Non-Reactive $t_{lag,composite}^b$ (hr)	Expected Non-Reactive $t_{lag,HDPE\ only}^c$ (hr)	% usage <sup>d</sup>
4156	132	381	134	40	$3.2 \times 10^{-11}$	$3.1 \times 10^{-11}$	16	7	4	32
4450	167	402	163	39	$2.4 \times 10^{-11}$	$2.1 \times 10^{-11}$	21	10	7	27
4543	177	402	161	77	$2.7 \times 10^{-11}$	$2.5 \times 10^{-11}$	30	10	7	25
4271	160	381	143	79	$2.9 \times 10^{-11}$	$2.7 \times 10^{-11}$	39	8	6	43
5784	155	400	140	194	$4.2 \times 10^{-11}$	$5.6 \times 10^{-11}$	67	8	5	64
3982	259	403	237	357	$2.4 \times 10^{-11}$	$1.9 \times 10^{-11}$	365	21	15	60

<sup>a</sup>  $C_{s0}$  is the initial concentration of PAC in the clay suspension layer.

<sup>b</sup> Expected non-reactive  $t_{lag,composite}$  is the expected lag time for an equivalent non-reactive version of the composite membrane. It is calculated using Equation 2-26.

<sup>c</sup> Expected non-reactive  $t_{lag,HDPE}$  is the expected lag time for a membrane with the thickness and permeability of only the two HDPE sheets used in the composite, representing the case in which the contribution of the center layer to the permeability of the composite is negligible.

<sup>d</sup> % usage is the percent of the total scavenger used before breakthrough. This is determined by back-calculating the effective  $C_{s0}$  from Equation 2-9 and the observed lag time and taking it as a percentage of the actual  $C_{s0}$  initially present in the membrane.

membrane. There are several possible reasons for the reduced capacity of carbon in the sandwich membrane. The small clay flakes may block sorption sites in the larger PAC particles due to the close proximity of the materials in the center layers. Alternatively, as contaminants are sorbed to the PAC, the driving force for sorption may be reduced so that sorption kinetics become important—the lower driving force results in a decrease in the product,  $k_2 C_{s0}$ . It is interesting to note that as the PAC concentration in the center layer is increased, the percentage of the total sorption capacity used before breakthrough also increases (see Table 3-2), supporting the hypothesis that the system is limited by kinetics over time.

### ***3.4 Engineering Considerations***

In addition to the increased  $\text{Fe}^0$  efficiency afforded by using sandwich membranes, composites containing either PAC or  $\text{Fe}^0$  may offer some practical benefits versus single-layer reactive membranes. For example, composite membranes can be assembled using commercially-available HDPE without the need for additional polymer processing. In the field, however, the thickness of the reactive or sorptive center layer may be difficult to control.  $\text{Fe}^0$  or PAC could be incorporated into commercially-available geosynthetic clay liners to provide strength and help keep the particles evenly distributed, provided the clay liners are wetted before placement between the two HDPE layers of the sandwich membrane. Consolidation of the aqueous clay suspension layer of the proposed sandwich membranes has the potential to squeeze water from the center layer, resulting in separate clay and water layers that may affect the permeability and shear strength of the composite

liner. How the center layer proposed in this study or commercially-available geosynthetic clay liners containing reactive or sorptive scavengers will perform under the confining stress of waste placed in a lined landfill deserves further investigation.

For chemicals that do not react quickly with  $\text{Fe}^0$ , PAC-containing sandwich membranes are successful in providing long lag times before contaminant breakthrough. Even more of the total scavenger capacity is used in PAC-containing sandwich membranes than in membranes using  $\text{Fe}^0$  before breakthrough is observed. This work shows that models used to describe membranes containing reactive scavengers can also be applied to sorptive scavenger-containing membranes when Equation 2-9 is used to account for the effects of sorption on the lag time. While these experiments show only the effects of the addition of PAC on TCE breakthrough, the effect of using activated carbon may be farther reaching. Any hydrophobic compound that can diffuse through HDPE is likely to sorb to PAC in the center layer of a sandwich membrane. Thus, barriers like this may provide improved containment for the wide range of hydrophobic chemicals present in many landfills (31-33,93). The consumption of PAC sorption sites by dissolved organic matter, however, could reduce the effectiveness of the barrier in containing anthropogenic chemicals. This topic also deserves further attention.

The data collected in this study can be used to estimate lag times expected for field-scale composite landfill liners. A sandwich membrane comprised of two 1-mm thick HDPE layers with a 2-mm thick clay suspension containing 1.8 wt%  $\text{Fe}^0$  nanoparticles will not allow the breakthrough of CT for 200 years when the upstream CT concentration is 10  $\mu\text{M}$ . This lag is a significant improvement over the 90-day lag time predicted for the

barrier's non-reactive counterpart. Based on the Langmuir isotherm at lower aqueous concentrations and on results listed in Table 3-2 for the membrane containing 24 wt% (357 g/L) PAC in the center layer, a barrier with the scaled-up dimensions described above and exposed on one side to an aqueous concentration of 10  $\mu\text{M}$  TCE will have a lag time of approximately 100 years. The same composite without the sorptive additive would see TCE breakthrough after 14 days.

## **Chapter 4**

### **Geomembranes containing powdered activated carbon have the potential to improve containment of chlorinated aromatic contaminants<sup>‡</sup>**

<sup>‡</sup> Reproduced in part with permission from “Surdo, E.M.; Cussler, E.L.; Novak, P.J.; Arnold, W.A. Geomembranes containing powdered activated carbon have the potential to improve containment of chlorinated aromatic contaminants. *Environmental Science and Technology*, 2009, 43, 8916-8922.” Copyright 2009 American Chemical Society.

#### **4.1 Introduction**

Exposure to polychlorinated biphenyls (PCBs) via equilibrium partitioning and through the food web leads to bioaccumulation in aquatic organisms (119-124). Consequently, high PCB concentrations in fish pose a human health threat that has led to fish consumption advisories for many lakes and rivers (125,126). Human exposure via consumption of PCB-contaminated food has been linked to outbreaks of skin lesions and chronic acne, elevated mortality rates from liver and respiratory system cancer, and delayed development in children exposed to PCBs via mothers' milk (127). The Yusho disease epidemic in northern Japan in 1968 and the 1979 Yu-Cheng incident in Taiwan highlight the risk of PCB exposure via the food chain, though many of the symptoms observed in Yusho patients have been attributed polychlorinated dibenzofurans, which can be produced through the pyrolysis of PCBs during cooking (127). Some PCB congeners also exhibit endocrine disrupting activity suspected of disrupting menstrual cycles in female Yusho patients (127,128).

While surface-water PCBs originate from a variety of sources (including atmospheric deposition) (126), contaminated sediment "hot spots" are the target of many remediation efforts. Traditionally, dredging has been used to reduce the exposure of aquatic species to PCB-contaminated sediments by physically removing them from lake- and riverbeds (129). Dredged sediments are commonly stored on non-porous high-density polyethylene (HDPE) geomembrane liners, either for permanent landfilling or for temporary dewatering before transport/treatment (130,131). HDPE geomembranes effectively contain water and heavy metals (9) and are regularly used for contaminant

isolation (e.g., landfill liners, silt screens). Hydrophobic molecules (trichloroethylene, benzene, xylene, etc.), however, diffuse more easily through HDPE (19-26,28). For example, Shimotori et al. (28) estimated that carbon tetrachloride would break through a 1.5-mm thick HDPE liner in 32 days. These observations highlight the potential for other hydrophobic contaminants, such as PCBs, to diffuse across HDPE liners. This study provides the first attempt at estimating PCB diffusion across HDPE geomembranes.

Sediment caps are increasingly preferred over dredging and *ex situ* treatment, because dredging stirs the contents of the river and its sediments, creating a slug of turbid and polluted water immediately following the dredging process (129,132-134). Sand caps physically separate contaminated sediments from the bioactive region and reduce the upward flux of aqueous PCBs from sediment porewater to the overlying surface water (135-138). Alternative materials, such as crushed limestone, bentonite-cement composites, and a proprietary clay-composite material called AquaBlok® offer reduced effective diffusion coefficients compared with sand (131,139,140).

Effective sorption of PCBs to activated carbon has led to research on the *in situ* sequestration of PCBs in contaminated sediments. One strategy mixes activated carbon into sediments to reduce PCB bioavailability (120,141-146). In laboratory tests, PCB bioaccumulation was up to 89% lower in *Macoma bathica* (clams) exposed to PCB-contaminated sediment treated with activated carbon than in those exposed to the same sediment without activated carbon (120). Less dramatic results were observed at a field site (142). Others have focused on the incorporation of thin layers of activated carbon or coke into sediment caps (136,147,148). Equilibrium sorption tests combined with

advection/diffusion modeling highlight the potential of active materials to extend the PCB isolation time in capped sediments (136). Coke incorporated into a permeable Reactive Core Mat® was recently deployed under a sand cap at a test site in the Anacostia River (147). To further the effectiveness of activated carbon sediment treatment/capping, using Fe<sup>0</sup>/Pd-doped activated carbon to both sorb and dechlorinate PCBs was recently proposed (149).

HDPE is used to line hazardous waste landfills because of its durability and resistance to degradation in the environment (11). Activated carbon has the potential to sorb PCBs as they migrate through an active sediment cap. The current study combines these two proven strategies to develop an HDPE barrier with improved barrier performance. Such a barrier might be used to line landfills and confined disposal facilities used to store PCB-contaminated sediments, to cap contaminated sediments *in situ* in special cases (when groundwater upwelling and gas production within capped sediments are not significant), and to cap terrestrial sources of atmospheric PCBs, such as transformer storage yards (126).

Experimentally, the first objective of this study was to characterize diffusion of a model PCB, 2,3',4',5-tetrachlorobiphenyl (2,3',4',5-PCB), through HDPE, poly(vinyl alcohol) (PVA), and composite membranes via breakthrough experiments. Experiments with 1,2,4-trichlorobenzene (1,2,4-TCB), a higher-solubility PCB surrogate, were used to evaluate the differences between conditions in our experiments and those expected in the environment. The second objective of this study was to determine the potential of powdered activated carbon (PAC) to improve the barrier performance of HDPE. By

comparing experimental breakthrough curves to existing model predictions, this work also provides results that further our understanding of how sorptive scavengers affect membrane breakthrough for hydrophobic pollutants and identifies the appropriate parameters for scaling results to field conditions.

## ***4.2 Experimental Section***

### *4.2.1 PAC Preparation and Characterization*

PAC (J.T. Baker) was sieved (150 mesh) before use. The particle size distribution of the sieved PAC, suspended in Isoton II Diluent (Beckman Coulter) was measured on a Beckman Coulter Multisizer 3 with a 400  $\mu\text{m}$  aperture tube.

### *4.2.2 Membrane Preparation*

Appropriate ratios of HDPE beads (DOWLEX IP-40, Dow) and PAC were mixed at 160°C in a Haake PolyLab OS RheoDrive 4 batch mixer (Thermo) for ~20 min. The resulting mixtures were pressed to films 100-400  $\mu\text{m}$  in thickness between two polytetrafluoroethylene (PTFE) sheets using a hot press (Wabash Metal Products) at 160°C with 3300-6700 N force. Membrane thicknesses varied as an artifact of variations in the membrane preparation process and were sometimes varied intentionally to test reproducibility. Thicknesses were measured with a micrometer (Mitutoyo). PVA membranes were prepared by adding 1.5 g PVA (Elvanol 71-30, DuPont) and the desired mass of PAC to 15 mL ultrapure water (Milli-Q, Millipore) on a hot plate (<100 °C) while stirring vigorously for 10 min. The suspension was cooled, degassed under

vacuum, and cast on a PTFE block. After drying at room temperature for two days, membranes were cross-linked in a 150 °C oven for 1 hour. PVA membranes were soaked in the appropriate liquid medium before use. A composite (layered) membrane was prepared by placing the two membranes, HDPE and PAC-containing PVA, back-to-back.

Digital photos of the PAC-containing HDPE and PVA membranes were taken using the 10×, 20×, and 40× lenses of a Nikon Eclipse E600 microscope equipped with an MTI 3CCD camera.

#### 4.2.3 Breakthrough Experiments

Membrane breakthrough experiments were conducted as described previously using the diaphragm cells shown in Figure 3-2 (28,30). Briefly, single-layer (HDPE or PVA) and composite (HDPE/PVA) membranes were fixed between two glass cells with epoxy (5-Minute Quick Set, Loctite or DP-125, 3M). Upstream cells were 350 and 550 mL for pure polymer and PAC-containing membrane breakthrough experiments, respectively.  $V_{down}$  was ~15 mL. Sediments are often used a reservoir for PCBs in biodegradation experiments, but in breakthrough experiments, slow desorption from sediments would make it difficult to maintain a constant aqueous  $C_{up}$  and would complicate specific evaluation of membrane performance. Using ultrapure water as the solvent in 2,3',4',5-PCB breakthrough experiments was not possible due to the low solubility of 2,3',4',5-PCB and limits on the size of samples that could be taken from the downstream cell. Instead, 2,3',4',5-PCB breakthrough experiments were conducted in a solution of 40% acetone (99.5%, Mallinckrodt Baker) and 60% ultrapure water. 1,2,4-TCB breakthrough

experiments were conducted in both water and in 40:60 acetone:water to evaluate the effect of the acetone cosolvent on breakthrough curves. To start each experiment, the upstream cell was spiked with an acetone solution of either 1,2,4-TCB (99+%, Sigma-Aldrich) or 2,3',4',5-PCB (99.0%, AccuStandard) to achieve a desired  $C_{up}$  of 40-50  $\mu\text{M}$  for 1,2,4-TCB experiments in water, 1000-1400  $\mu\text{M}$  for 1,2,4-TCB experiments in 40:60 acetone:water, and 4-10  $\mu\text{M}$  for 2,3',4',5-PCB experiments in 40:60 acetone:water. Acetone spikes were less than 1% of the upstream cell volume. Both cells were stirred rapidly using magnetic stirrers. One-milliliter samples were collected from both cells of 2,3',4',5-PCB experiments and from the downstream cells of 1,2,4-TCB experiments conducted with water. The sampled volume was replaced with clean solution to keep  $V_{down}$  constant throughout the experiment. Upstream samples collected from 1,2,4-TCB experiments in water were 50  $\mu\text{L}$ . For 1,2,4-TCB experiments in 40:60 acetone:water, 10- $\mu\text{L}$  and 5- $\mu\text{L}$  samples were collected from the downstream and upstream cells, respectively, without replacement.

One of the assumptions crucial to extrapolating  $D$ , the diffusion coefficient, and  $H$ , the membrane-solution partition coefficient, from breakthrough experiments is that the sole layer of diffusive resistance is the HDPE membrane (i.e., the diffusive boundary layer in the solution phase is infinitely thin). Upstream stirring rates were varied for several 2,3',4',5-PCB breakthrough experiments to evaluate the effects of boundary layer mixing. A Strobotac type 1531-A variable-frequency strobe light (General Radio Company) was used to estimate stirring rates in 2,3',4',5-PCB breakthrough experiments. The strobe light was aimed toward the upstream stir plate in a dark room. The frequency

was adjusted until the stir bar appeared to be still, indicating that the stir bar had made a full rotation between flashes of light. Frequency was adjusted through a broad spectrum to ensure that the frequency capturing one full rotation (e.g., not a half rotation or two rotations) was properly identified.

#### *4.2.4 Equilibrium Experiments*

To measure  $H$  at equilibrium, 20- or 40-mL serum bottles were loaded with HDPE strips with thicknesses up to 200  $\mu\text{m}$ , filled headspace-free with water (1,2,4-TCB only) or aqueous solutions of 10%, 20%, or 40% acetone, spiked with 1,2,4-TCB or 2,3',4',5-PCB stock solutions, sealed, and stored on a shaker table for 6 and 94 days, respectively. To develop PAC sorption isotherms for 1,2,4-TCB in water and 2,3',4',5-PCB in 40:60 acetone:water, serum bottles were loaded with varying mass of PAC, filled headspace-free with water or 40:60 acetone:water, spiked with 1,2,4-TCB or 2,3',4',5-PCB, respectively, and stored on a shaker table for at least 6 days. Bottles were removed from the shaker table a day before sampling to allow PAC particles to settle. All solutions were sampled as described above.

#### *4.2.5 Sample Extraction and Analysis*

For 2,3',4',5-PCB experiments, 1-mL samples were hand-shaken with two sequential aliquots of hexane (65% n-hexane, Fisher Scientific) for 2 minutes each. The hexane phase was then shaken for 2 minutes each with 1 mL sodium chloride solution (38 g sodium chloride (99.5%, Mallinckrodt Baker) in 900 mL Milli-Q water), 1 mL 10%

sulfuric acid solution (95.9%, Mallinckrodt Baker), and 1 mL sodium chloride solution again. Finally, the hexane phase was dried with ~2 g anhydrous sodium sulfate (99.4%, Fisher Scientific). The extraction efficiency of this procedure was 85-90%. For 1,2,4-TCB experiments in solutions containing 10%, 20%, and 40% acetone, 10- $\mu$ L samples were extracted in 1 mL hexane by vortex mixing (Touch Mixer 232, Fisher Scientific) for 30 seconds. For 1,2,4-TCB experiments in water, 0.5-mL samples were extracted in 1 mL hexane by vortex mixing for 1 minute. 1,2,4-TCB extraction efficiencies were 91% and 83-93%, respectively, for extraction from 40:60 acetone:water and from water.

Hexane extracts were analyzed on a Hewlett Packard 5890A gas chromatograph equipped with a an electron capture detector (oven temperature at 100 °C for 2 min, 15 °C/min to 160 °C, 5 °C/min to 235 °C, hold for 3 min, 15 °C/min to 270 °C, hold for 2 min). Two-microliter samples were injected to a splitless inlet at 225 °C on an HP-5 column (30 m  $\times$  0.32 mm i.d.  $\times$  0.25  $\mu$ m film thickness, J&W). The instrument was calibrated using a set of six to ten 2,3',4',5-PCB or 1,2,4-TCB standards in hexane. The limits of detection for 1,2,4-TCB and 2,3',4',5-PCB extracts in hexane were 0.02  $\mu$ M and 0.4  $\mu$ M, respectively, as determined from the area of a chromatography peak 3  $\times$  larger than the noise of the instrument.

### 4.3 Results and Discussion

#### 4.3.1 Pure Polymers

Normalized breakthrough curves across HDPE for both solutes are shown in Figure 4-1.  $D$  and  $H$  were calculated by fitting Equation 2-2 ( $n=6$ ) to the data using a least-squares fit (solid lines in Figure 4-1).

$$\frac{C_{down}}{C_{up}} = \frac{DHA}{LV_{down}} \left( t - \frac{L^2}{6D} - \frac{2L^2}{\pi^2 D} \sum_{n=1}^{\infty} \frac{(-1)^n}{n^2} e^{-\frac{Dn^2\pi^2 t}{L^2}} \right) \quad (2-2)$$

Fit  $D$  values (Table 4-1) for 1,2,4-TCB in HDPE using water and 40:60 acetone:water as the liquid media in the diaphragm cells are similar. Thus, the effect of acetone on  $D$  for 2,3',4',5-PCB was assumed to be minimal. The reduction in  $P$  observed with the addition

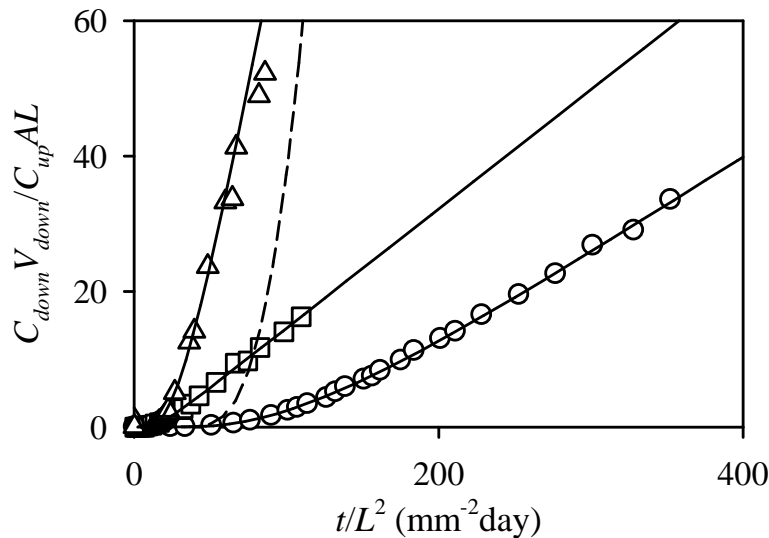


**Figure 4-1.** Breakthrough curves of 1,2,4-TCB in water ( $\Delta$ ), 1,2,4-TCB in 40:60 acetone:water ( $\square$ ), and 2,3',4',5-PCB in 40:60 acetone:water ( $\circ$ ) across HDPE. Curves (—) were fit using Equation 2-2 ( $n=6$ ), and resulting  $D$  and  $H$  values are reported in Table 4-1. Predicted curves (---) represent estimated 2,3',4',5-PCB breakthrough behavior in water.

**Table 4-1.** Pure polymer transport data<sup>a,b</sup>

Polymer	Solute	Solvent	$L^c$ ( $\mu\text{m}$ )	$C_{up}$ ( $\mu\text{M}$ )	$H$	$D \times 10^{12}$ ( $\text{m}^2/\text{s}$ )	$P \times 10^{12}$ ( $\text{m}^2/\text{s}$ )	$R^2$
HDPE	1,2,4-TCB	water	207 $\pm$ 3	53 $\pm$ 7	230 $\pm$ 30	0.059 $\pm$ 0.004	14 $\pm$ 2	0.998
HDPE	1,2,4-TCB	water	398 $\pm$ 7	39 $\pm$ 5	230 $\pm$ 50	0.050 $\pm$ 0.004	12 $\pm$ 3	0.997
HDPE	1,2,4-TCB	40:60 <sup>d</sup>	173 $\pm$ 4	1070 $\pm$ 40	18 $\pm$ 3	0.11 $\pm$ 0.01	2.0 $\pm$ 0.4	0.999
HDPE	2,3',4',5-PCB	40:60	200 $\pm$ 8	4.7 $\pm$ 0.1	102 $\pm$ 6	0.0161 $\pm$ 0.0005	1.6 $\pm$ 0.1	0.999
HDPE	2,3',4',5-PCB	40:60	140 $\pm$ 8	5.7 $\pm$ 0.2	47 $\pm$ 8	0.026 $\pm$ 0.003	1.2 $\pm$ 0.2	0.998
HDPE	2,3',4',5-PCB	40:60	154 $\pm$ 9	5.4 $\pm$ 0.1	110 $\pm$ 20	0.012 $\pm$ 0.001	1.3 $\pm$ 0.3 <sup>e</sup>	0.998
HDPE	2,3',4',5-PCB	40:60	150 $\pm$ 10	7.1 $\pm$ 0.2	110 $\pm$ 20	0.020 $\pm$ 0.002	2.2 $\pm$ 0.4 <sup>f</sup>	0.999
PVA	1,2,4-TCB	water	154 $\pm$ 4	55 $\pm$ 3	3 $\pm$ 2	60 $\pm$ 30	200 $\pm$ 200	0.999
PVA	1,2,4-TCB	40:60	80 $\pm$ 5	1350 $\pm$ 50	1.1 $\pm$ 0.5	2.0 $\pm$ 0.8	2 $\pm$ 1	0.999
PVA	2,3',4',5-PCB	40:60	123 $\pm$ 3	11.9 $\pm$ 0.4	2 $\pm$ 4	0.4 $\pm$ 0.6	1 $\pm$ 2	0.999

<sup>a</sup> upstream stirring rate = 940 s<sup>-1</sup> unless otherwise noted

<sup>b</sup> errors given are 95% confidence intervals

<sup>c</sup> membrane thicknesses were measured after "hydration" in water or 40:60 acetone:water

<sup>d</sup> 40:60 acetone:water solution

<sup>e</sup> upstream stirring rate = 690 s<sup>-1</sup>

<sup>f</sup> upstream stirring rate = 1300 s<sup>-1</sup>

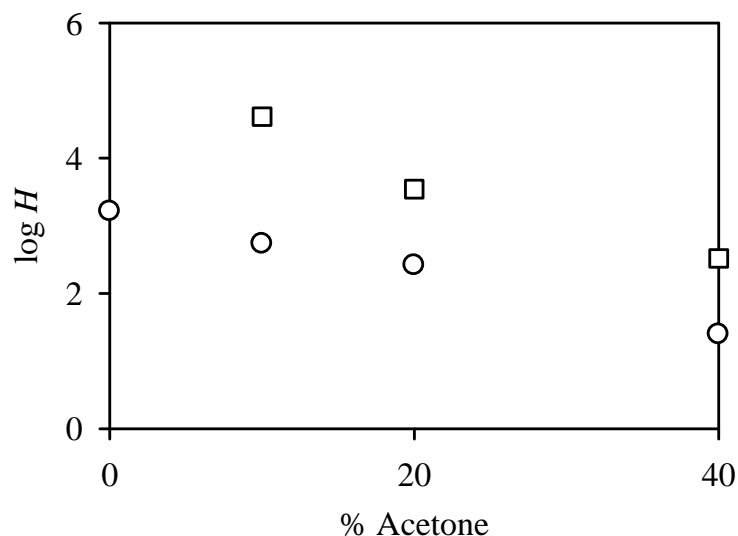


**Figure 4-2.** HDPE membrane-solution partition coefficients for 1,2,4-TCB (○) and 2,3',4',5-PCB (□) in water and in aqueous solutions containing up to 40% acetone.

of acetone to 1,2,4-TCB experiments, therefore, is due to a reduction in  $H$ . This reduction was expected, because solubility increases with the addition of an organic cosolvent.

The  $H$  values for HDPE determined by fitting breakthrough curves (Table 4-1) are 1.5 to 7-fold lower than those determined from equilibrium experiments shown in Figure 4-2. This result may be an artifact of leakage from the equilibrium experiments, although controls indicate that leakage was not a primary factor. The series of 2,3',4',5-PCB breakthrough experiments at various mixing rates were conducted to determine whether improper upstream mixing affected the apparent  $H$  in breakthrough experiments (Table 4-1 and Figure 4-3). The resulting breakthrough curves showed a small effect of mixing on apparent  $D$ , but  $H$  was unaffected.

Inflated equilibrium  $H$  values (compared with breakthrough experiment  $H$ ) have been observed previously (28,150). Historically, researchers have attributed differences in equilibrium and breakthrough experiment  $H$  to differences in the uptake kinetics and sorption capacities of crystalline and amorphous areas of glassy polymers (51,150). While room-temperature HDPE is above the glass transition temperature, heterogeneities in the polymer matrix may create areas with different sorption properties, resulting in the observed differences in breakthrough and equilibrium experiment  $H$  values. Regardless, breakthrough experiment  $D$  and  $H$  values represent the barrier abilities of HDPE when used for containment. Thus, breakthrough experiment values were used in the analysis presented below.

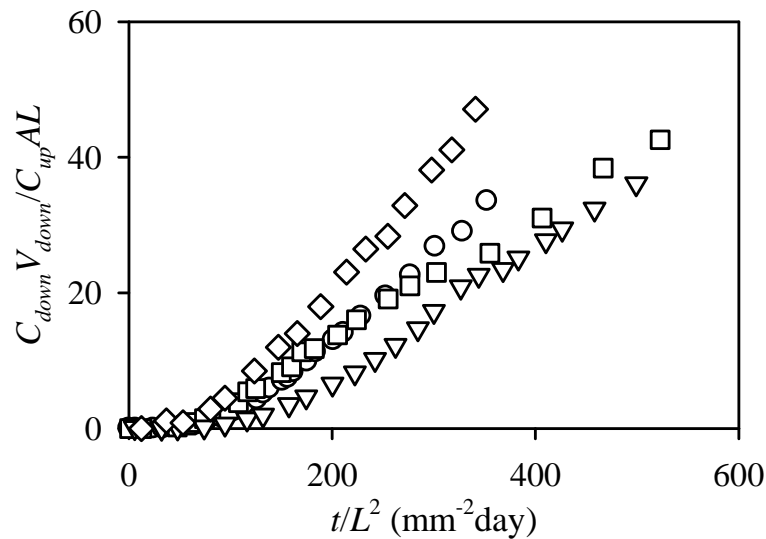


**Figure 4-3.** Replicate 2,3',4',5-PCB breakthrough curves in 40:60 acetone:water in HDPE. Experiments with a stirring rate of  $940 \text{ s}^{-1}$  ( $\circ, \square$ ) are compared with experiments with upstream stirring rates of  $690 \text{ s}^{-1}$  ( $\nabla$ ) and  $1300 \text{ s}^{-1}$  ( $\diamond$ ).

Figure 4-4 shows breakthrough curves for both solutes across pure PVA. PVA is hydrophilic and swelled with water in aqueous experiments. Reduced swelling in 40:60 acetone:water resulted in a denser polymer and, therefore, a reduced  $D$  (~30-fold) for 1,2,4-TCB (Figure 4-4 inset and Table 4-1). The magnitude of  $H$  for PVA was so low (order of magnitude=1), that equilibrium values were not measured. The reduction in permeability for 1,2,4-TCB in 40:60 acetone:water was primarily the result of reduced  $D$ .

The predicted curves (dashed lines) in Figures 4-1 and 4-4 were generated using Equation 2-2 and estimates of  $D$  ( $8 \times 10^{-15}$  m<sup>2</sup>/s for HDPE and  $1 \times 10^{-11}$  m<sup>2</sup>/s for PVA) and  $H$  (40,000 for HDPE and 6 for PVA) for 2,3',4',5-PCB in water. The estimate for  $D$  is

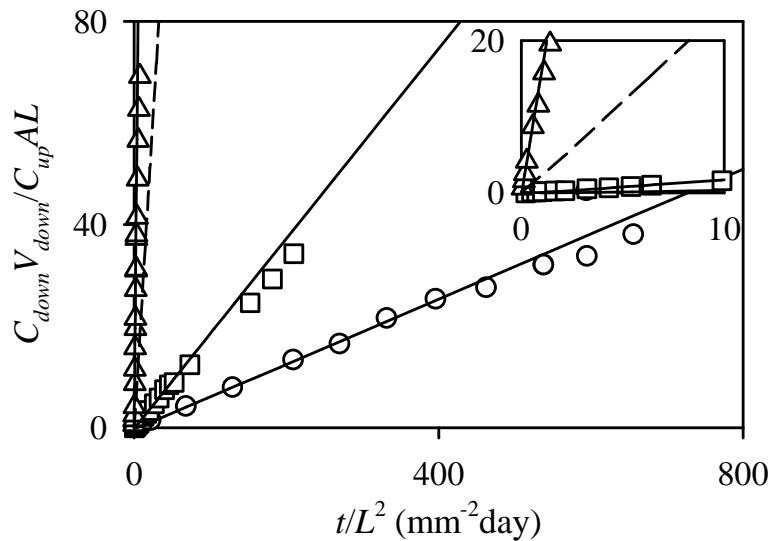


**Figure 4-4.** Breakthrough curves of 1,2,4-TCB in water ( $\Delta$ ), 1,2,4-TCB in 40:60 acetone:water ( $\square$ ), and 2,3',4',5-PCB in 40:60 acetone:water ( $\circ$ ) across PVA. Curves (—) were fit using Equation 2-2 ( $n=6$ ), and resulting  $D$  and  $H$  values are reported in Table 4-1. Predicted curves (---) represent estimated 2,3',4',5-PCB breakthrough behavior in water. The inset details initial data.

based on  $D$  for 2,3',4',5-PCB in 40:60 acetone:water, corrected for the solvent effects observed in 1,2,4-TCB experiments, and is about a factor of 15 lower than that reported by Pascall et al. (80) for 2,2',4,4'-tetrachlorobiphenyl in low-density polyethylene (LDPE). The HDPE  $H$  estimate is based on 2,3',4',5-PCB breakthrough experiment  $H$  and an equilibrium value for a solution with 0% acetone extrapolated from the data shown in Figure 4-2.

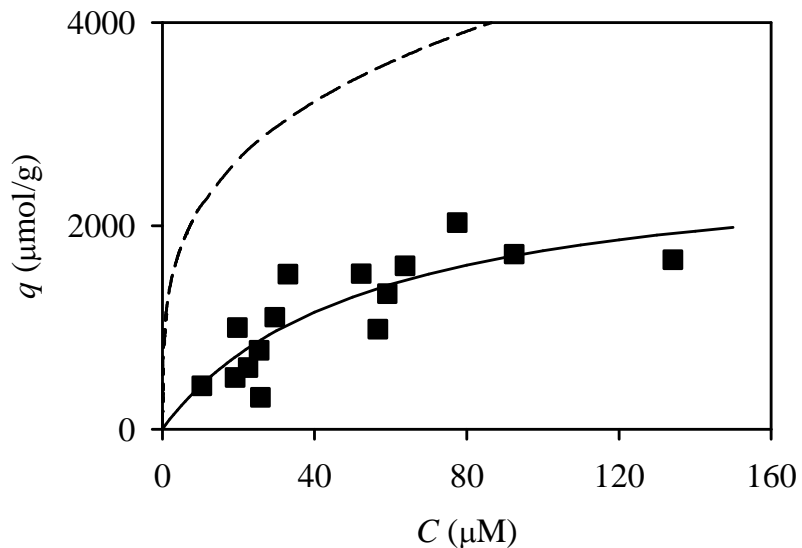


**Figure 4-5.** Equilibrium sorption data (■) for 1,2,4-TCB sorption to PAC in water and a Langmuir isotherm fit with  $q_{max}=3000\pm 1000 \mu\text{mol/g}$  and  $b=0.02\pm 0.02 \text{ L}/\mu\text{mol}$  (—).<sup>1</sup> The solubility-normalized Freundlich isotherm described by Kleineidam et al. (118) for sorption from water by an activated carbon is also shown (---).

<sup>1</sup> Isotherm data for 1,2,4-TCB were collected by Andrew Warta.

### 4.3.2 HDPE Membranes with PAC

PAC sorption isotherm data for 1,2,4-TCB in water and 2,3',4',5-PCB in 40:60 acetone:water are shown in Figures 4-5 and 4-6. Sorption of 1,2,4-TCB was lower than expected based on estimates reported in the literature. However, we suspect that the activated carbon used by Kleineidam et al. (118) was a granular activated carbon and not PAC. A comparison for 2,3',4',5-PCB is not provided in Figure 4-6, because experiments are not traditionally conducted in a cosolvent solution like the 40:60 acetone:water used in our experiments.

Breakthrough curves for PAC-containing HDPE membranes are summarized in Figures 4-7 and 4-8. The addition of 0.04 g PAC/cm<sup>3</sup> to HDPE clearly failed to alter

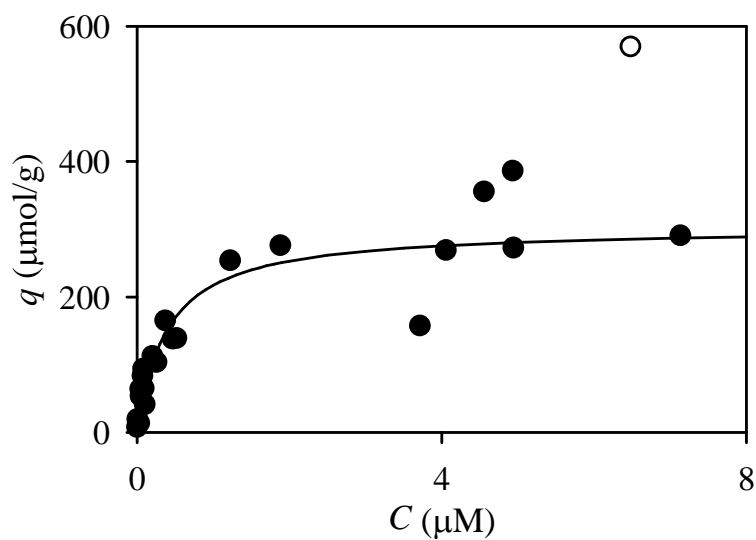


**Figure 4-6.** Equilibrium sorption data (●) for 2,3',4',5-PCB sorption to PAC in 40:60 acetone:water and a Langmuir isotherm fit with  $q_{max}=370\pm 80$  μmol/g and  $b=1\pm 1$  L/μmol (—). Open symbols represent data that were omitted from the Langmuir fitting data set.

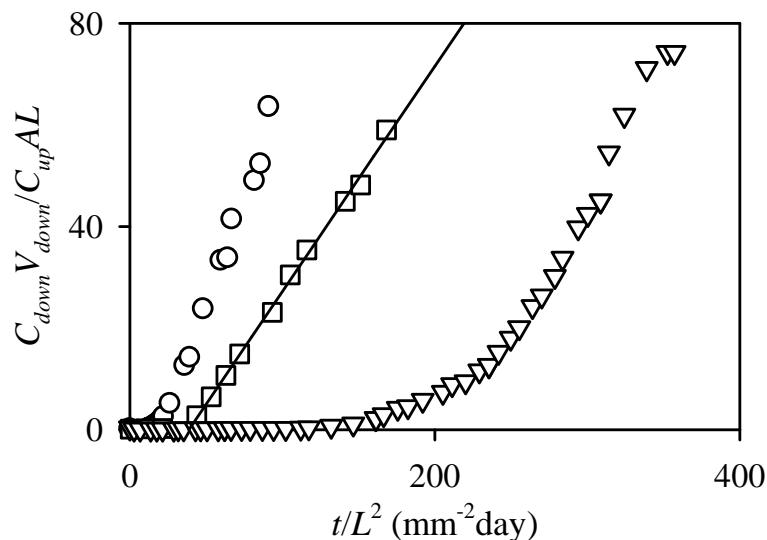


**Figure 4-7.** Breakthrough curves for 1,2,4-TCB in water across pure HDPE (○) and HDPE membranes with 0.14 g PAC/cm<sup>3</sup> (□) and 0.29 g PAC/cm<sup>3</sup> (▽). Solid line (—) is a linear fit for breakthrough across HDPE with 0.14 g PAC/cm<sup>3</sup> ( $P=5.1(\pm 0.7) \times 10^{-12}$  m<sup>2</sup>/s,  $R^2=0.997$ ).

2,3',4',5-PCB breakthrough. For membranes with 0.14 g PAC/cm<sup>3</sup>, the permeability of both solutes was reduced by ~60% compared with pure HDPE. Increasing the PAC content in the membrane to 0.29 g PAC/cm<sup>3</sup> increased the lag time for 1,2,4-TCB by more than a factor of 6 but did not further reduce the permeability.

To understand our experimental results in the context of the models described above, we fit the experimental data for membranes with 0.14 g PAC/cm<sup>3</sup> using each of the model equations in Table 2-1. Selected parameters ( $C_{s0}$  for model 1 and  $K$  for model 3) were allowed to vary during the fitting process (Table 4-2). For example, observed lag times were not accurately predicted by the moving-reactive front model (model 1 in

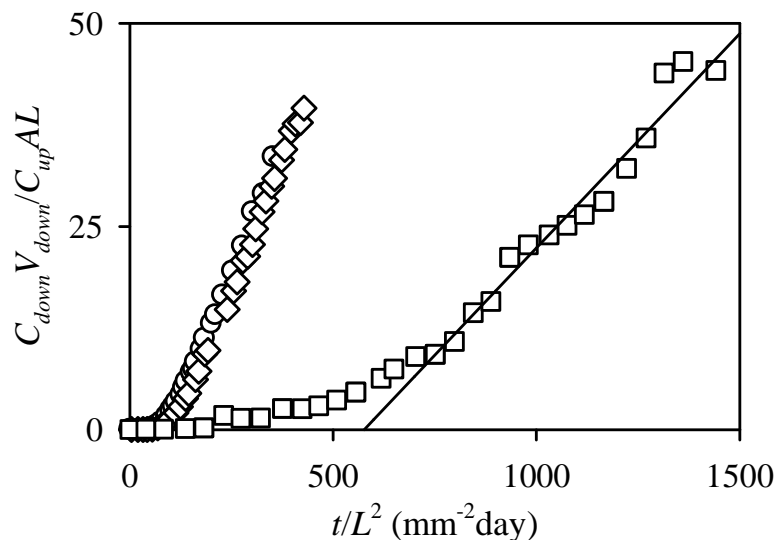


**Figure 4-8.** Breakthrough curves for 2,3',4',5-PCB in 40:60 acetone:water across pure HDPE ( $\circ$ ) and HDPE membranes with 0.04 g PAC/cm<sup>3</sup> ( $\diamond$ ) and 0.14 g PAC/cm<sup>3</sup> ( $\square$ ). Solid line (—) is a linear fit for 2,3',4',5-PCB breakthrough across HDPE with 0.14 g PAC/cm<sup>3</sup> ( $P=0.61(\pm 0.06)\times 10^{-12}$  m<sup>2</sup>/s,  $R^2=0.788$ ).

Table 2-1), which assumes complete saturation of the PAC before breakthrough. Instead, observed lag times were used to determine “effective”  $C_{s0}$  values for each experiment. This technique has been used previously to evaluate scavenger effectiveness in membrane barriers (28). “Effective”  $C_{s0}$  values were 140 and 35 times lower than the actual PAC loading (0.14 g PAC/cm<sup>3</sup>) for 1,2,4-TCB and 2,3',4',5-PCB, respectively. The moving reactive front model also predicts that the steady-state flux after breakthrough is equal to that for pure HDPE, which was not observed.

High experimental upstream concentrations invalidate the central assumption of the fast equilibrium model (model 3 in Table 2-1), that sorption occurs in the linear portion

**Table 4-2.** Observed and expected model parameter values for PAC-containing HDPE membranes

	1,2,4-TCB	2,3',4',5-PCB
Experimental Conditions		
$L$	144 $\mu\text{m}$	146 $\mu\text{m}$
$C_{up}$	42 $\mu\text{M}$	9.4 $\mu\text{M}$
$C_{s0}$	0.14 g PAC/cm <sup>3</sup>	0.14 g PAC/cm <sup>3</sup>
average $R$	20 $\mu\text{m}$	20 $\mu\text{m}$
Moving Reactive Front Model		
observed $t_{lag}$	19 $\pm$ 2 hr	300 $\pm$ 40 hr
predicted pure HDPE $t_{lag}$ (model 0)	17 hr	62 hr
predicted $t_{lag}$ with PAC (model 1)	2,100 hr	10,000 hr
“effective” $C_{s0}$	0.001 g PAC/cm <sup>3</sup>	0.004 g PAC/cm <sup>3</sup>
Fast Equilibrium Model		
expected PAC-membrane partition coefficient, $K$	4.4	250
“effective” $K$	0.1	3.8
Diffusion-Limited Kinetics Model		
“effective” $R$	38 $\mu\text{m}$	37 $\mu\text{m}$

of the Langmuir isotherm. Therefore, it was not surprising that the “effective”  $K$  determined from observed lag times were over 40 times less than those inferred from equilibrium PAC and membrane partition coefficients.

For the pseudo-first-order kinetics model, the reduced flux observed (Figures 4-7 and 4-8) was assumed to be the pseudo-steady-state flux predicted from the model 2 expression given in Table 2-1. For this model, a pseudo-first-order rate constant,  $k_1$ , is required. Because sorption to PAC is typically very fast, we suspected that the kinetics associated with sorption to membrane-bound PAC was limited by diffusion from the bulk membrane toward the PAC particles, as described in Chapter 2 (section 2.4.1). In this case, Equation 2-19 estimates the pseudo-first-order rate constant.

$$k_1 = \frac{3D}{R^2 \left(1 - \phi^{1/3}\right) \left(\frac{1}{\phi} - 1\right)} \quad (2-19)$$

The predictions of the diffusion-limited kinetics model vary with  $\phi$  and  $R$ . Because  $\phi$  is known (0.08 for membranes with 0.14 g PAC/cm<sup>3</sup>), particle radius,  $R$ , was allowed to vary.  $R$  calculated from model fitting (Table 4-2) was about twice the mass-averaged particle radius of 20  $\mu\text{m}$  (Figure 4-9). The wide distribution of particle radii shown in Figure 4-9 might partially explain the higher-than-expected “effective”  $R$ , because the presence of several large particles may dominate the total mass of particles in the membrane. Imperfect particle dispersion might also contribute to the observed “effective”  $R$ , because agglomerations of particles will act as one large particle. Such agglomeration was observed in the optical images shown in Figure 4-10.

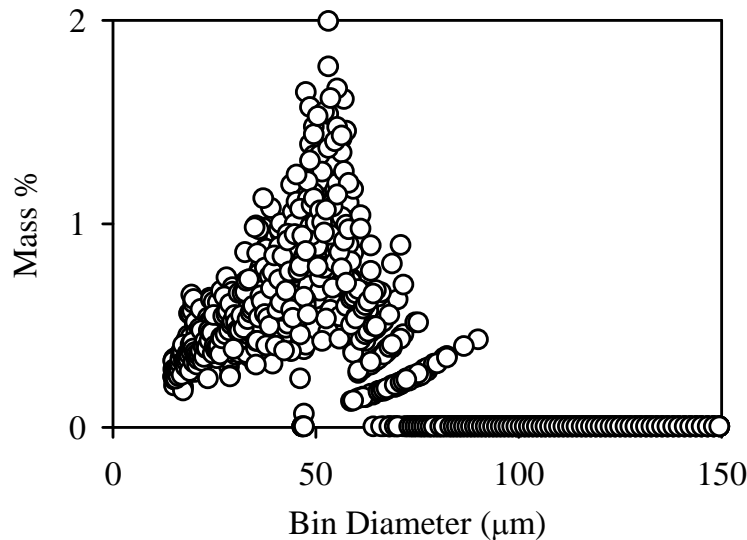


**Figure 4-9.** Distribution of the total mass of a sieved PAC sample by particle diameter.

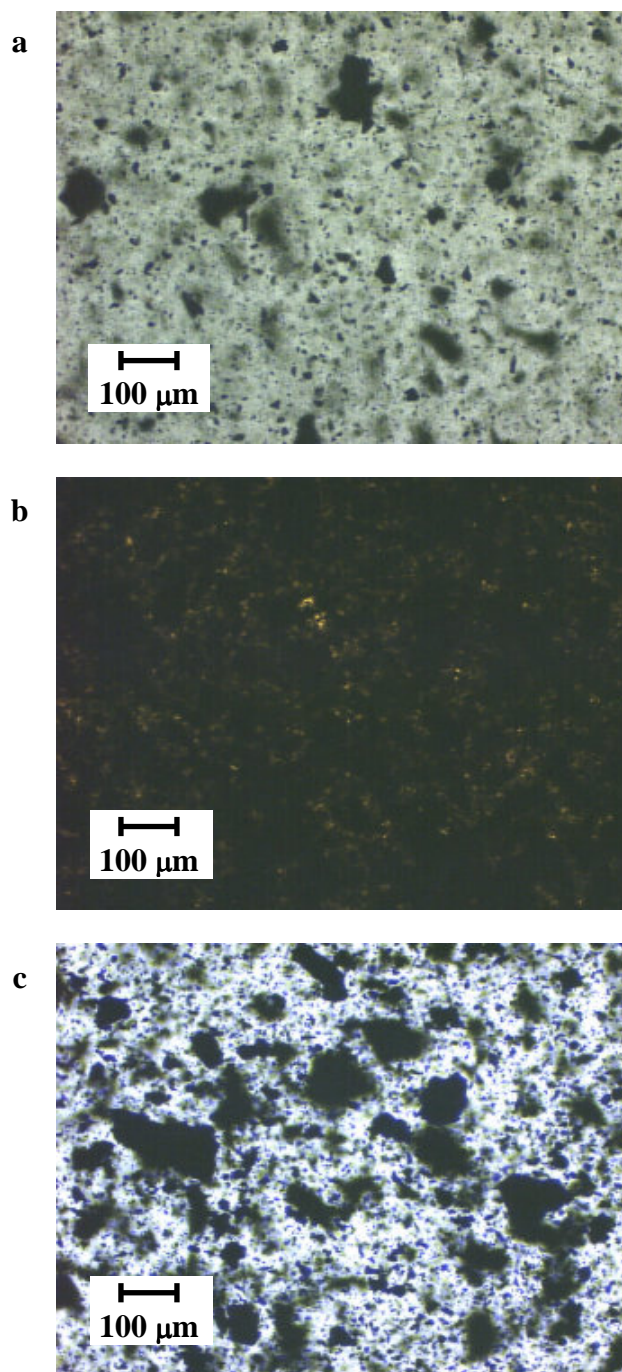


**Figure 4-10.** 10× magnified images of HDPE membranes containing 0.04 g PAC/cm<sup>3</sup> (a) and 0.14 g PAC/cm<sup>3</sup> (b) and PVA containing 0.05 g PAC/cm<sup>3</sup> (c). PAC particles in the HDPE membrane with 0.29 g PAC/cm<sup>3</sup> (not shown) were too dense to allow light through for a photograph.

Because it provided the best fit for HDPE breakthrough curves with 0.14 g PAC/cm<sup>3</sup>, the diffusion-limited kinetics model was used to analyze the remainder of our data. This model cannot be used to predict a lag time analytically, though others have developed numerical solutions to Equation 2-11 for specific cases (3,5).

$$\frac{\partial C_m}{\partial t} = D \frac{\partial^2 C_m}{\partial x^2} - k_1 C_m \quad (2-11)$$

With diffusion-limited kinetics, there is a brief lag time, a long period of reduced (pseudo-steady-state) flux, and after the PAC is saturated, the flux increases to the steady-state value for pure polymer membranes described by model 0 (Table 2-1). The duration and magnitude of this reduced-flux period provide the information needed to predict field-scale performance.

The diffusion-limited pseudo-first-order sorption rate constant,  $k_1$ , decreases with decreasing PAC loading (Equation 2-19), reducing the probability that a solute molecule will diffuse toward a PAC particle. The result is a shift in diffusion behavior toward that for the pure polymer, which might explain the apparent failure of the HDPE membrane with 0.04 g PAC/cm<sup>3</sup> to reduce 2,3',4',5-PCB flux (Figure 4-7). When PAC content was increased to 0.29 g PAC/cm<sup>3</sup>,  $t_{lag}$  increased but no additional effect on the pseudo-steady-state flux was observed (Figure 4-6). Here, the particles may be close enough to one another that diffusion to the particle surface is no longer the sole limiting factor. Fast “reaction” at the particle surface increases the lag time according to the moving reactive front model (model 1 in Table 2-1). Thus, the observed breakthrough curve suggests that

the underlying mechanisms in membranes with high PAC loading are a combination of those described by diffusion-limited kinetics and the moving reactive front model.

#### 4.3.3 HDPE/PVA-PAC Composite Membrane

In the experiments described in Chapter 3, Fe<sup>0</sup> nanoparticles were more effective (higher “effective” C<sub>s,0</sub>) when incorporated into an aqueous layer between two HDPE membranes than when embedded in HDPE (28). We suspected that the reaction involving Fe<sup>0</sup>, water, and the diffusing carbon tetrachloride was kinetically-limited in the hydrophobic HDPE matrix. If this hypothesis is correct, sorption to PAC from an HDPE matrix would also be less favorable than sorption to PAC from an aqueous solution (or hydrophilic polymer), resulting in a similar kinetic limitation in HDPE (if sorption rate, not diffusion toward a PAC particle, is limiting).

A breakthrough experiment with a 2-layer composite membrane was used to test whether incorporating the PAC into a hydrophilic layer would improve the effectiveness of PAC in a barrier membrane. The composite consisted of a pure HDPE membrane in contact with the upstream solution (to reduce the flux through the overall barrier) and a PAC-containing PVA layer downstream (to promote more effective 2,3',4',5-PCB sorption to PAC). Observed 2,3',4',5-PCB breakthrough data and a curve predicted for the same composite without PAC are shown in Figure 4-11. Equations 2-26 and 2-27 were used to generate the predicted curve.

$$\frac{L_{composite}}{P_{composite}} = \frac{L_{A1} + L_{A2}}{P_A} + \frac{L_B}{P_B} \quad (2-26)$$

$$t_{lag} = \frac{\left[ \frac{L_{A1}^2}{D_A} \left( \frac{L_{A1} + 3L_{A2}}{6P_A} + \frac{L_B}{2P_B} \right) + \frac{L_B^2}{D_B} \left( \frac{L_{A1} + L_{A2}}{2P_A} + \frac{L_B}{6P_B} \right) \right] + \frac{L_{A2}^2}{D_A} \left( \frac{3L_{A1} + L_{A2}}{6P_A} + \frac{L_B}{2P_B} \right) + \frac{L_{A1}L_BL_{A2}}{P_A^2}}{\frac{L_{A1} + L_{A2}}{P_A} + \frac{L_B}{P_B}} \quad (2-27)$$

The effective permeability of the PVA layer ( $1.8(\pm 0.2) \times 10^{-13} \text{ m}^2/\text{s}$ ) was a factor of 4.2 lower than for pure PVA in 40:60 acetone:water (Table 4-1). In fact, addition of 0.05 g PAC/cm<sup>3</sup> to PVA had greater impact on permeability than addition of 0.14 g PAC/cm<sup>3</sup> to HDPE, supporting our hypothesis that the matrix in which a scavenger is placed is an important factor in its effectiveness (28). This result is likely due to 1) the fact that

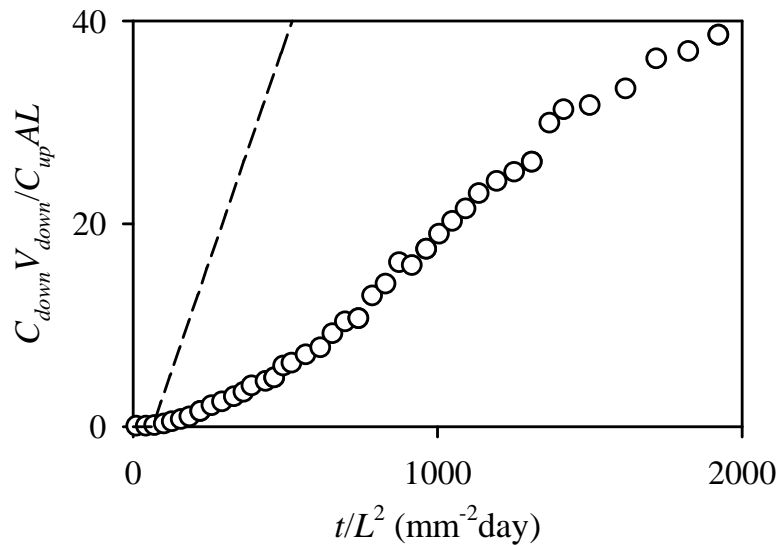


**Figure 4-11.** 2,3,4,5-PCB breakthrough curve in 40:60 acetone:water of a two-layer membrane with HDPE ( $132 \pm 6 \mu\text{m}$ ) upstream and PVA with 0.05 g PAC/cm<sup>3</sup> ( $130 \pm 3 \mu\text{m}$ ) downstream (O) and a curve predicted for a PAC-free version of this two-layer membrane (—).

2,3',4',5-PCB diffusion in PVA is faster than in HDPE, resulting in a higher  $k_1$ , 2) the increased driving force for sorption present when 2,3',4',5-PCB is dissolved in a hydrophilic matrix, or 3) both. Option 2 suggests that diffusion is not the only limitation affecting  $k_1$ , but it is difficult to separate the two effects experimentally.

#### 4.3.4 Engineering Implications

The pseudo-steady-state flux calculated using the diffusion-limited kinetics model is non-linear with respect to  $L$ . Using this model and the “effective”  $R$  determined from our experimental data, the pseudo-steady-state flux of both solutes through field-scale barriers is predicted (Table 4-3). The conservative upstream concentrations chosen for scale-up calculations were loosely based on total PCB porewater concentrations in contaminated sediment samples (73,151). The calculations assume constant upstream concentrations, which are not necessarily expected given the desorption resistance of sediment-associated PCBs (152-155), but the assumption helps to isolate the effect of the membrane barrier. The predicted pseudo-steady-state flux for both solutes is extremely low (as low as 300 *molecules* per  $m^2$  per year). In contrast, Murphy et al. (136) estimated diffusive fluxes from sediments capped with 15 cm of sand and those including a 1.25 cm activated carbon layer ranging from  $2.7 \times 10^{-5}$  to  $3.8 \times 10^{-7}$  mol/ $m^2$ year. Also apparent in Table 4-3 is the benefit of using a 2-layer membrane in which drastic flux reductions are achieved using less PAC.

Nevertheless, further confirmation of diffusion-limited kinetics predictions may be necessary to validate the values in Table 4-3. Model validity could be further investigated

**Table 4-3.** Diffusion-limited kinetics model scale-up estimates for PAC-containing barriers

$C_{up}$	1 nM TCB	0.01 nM PCB	0.01 nM PCB
$L$	2 mm	2 mm	1 mm pure HDPE and 1 mm PVA with PAC
$C_{s0}$	0.14 g PAC/cm <sup>3</sup>	0.14 g PAC/cm <sup>3</sup>	0.05 g PAC/cm <sup>3</sup>
$D$	$6 \times 10^{-14}$ m <sup>2</sup> /s	$8 \times 10^{-15}$ m <sup>2</sup> /s	$8 \times 10^{-15}$ m <sup>2</sup> /s for HDPE $1 \times 10^{-11}$ m <sup>2</sup> /s for PVA
$H$	230	40,000	40,000 for HDPE 6 for PVA
pseudo-steady-state flux <sup>a</sup>	$8 \times 10^{-21}$ mol/m <sup>2</sup> year	$5 \times 10^{-22}$ mol/m <sup>2</sup> year	$8 \times 10^{-18}$ mol/m <sup>2</sup> year
time until PAC capacity is reached <sup>b</sup>	70 years	12,000 years	6,000 years
final steady-state flux <sup>c</sup>	$2 \times 10^{-7}$ mol/m <sup>2</sup> year	$5 \times 10^{-8}$ mol/m <sup>2</sup> year	$2 \times 10^{-8}$ mol/m <sup>2</sup> year

<sup>a</sup> Intermediate, pseudo-steady-state flux as a result of adding PAC to the membranes.

<sup>b</sup> Assuming that all trichlorobenzene and PCB congeners diffuse and sorb similarly.

<sup>c</sup> Final steady-state flux after the PAC is loaded to capacity with solute. This flux is equivalent to that expected for a PAC-free barrier.

using thicker membranes with similar PAC loadings. Unfortunately, such experiments would require longer time periods than would be practical in a laboratory setting.

Additional studies may explore the effect of temperature, dissolved organic matter (DOM), and aging on PAC-containing membrane performance. For example, membrane-bound PAC may offer greater resistance to the reduction in sorption capacity in the presence of DOM observed by McDonough et al. (156) by reducing access of large DOM molecules to the PAC surface. The potential flux reductions outlined in Table 4-3 reinforce the need for further study.

## **Chapter 5**

### **Barrier Properties of PVA Membranes with Carbon Nanotubes: A Comparison with Powdered Activated Carbon-Containing PVA**

## 5.1 Introduction

The increasing use of carbon nanotubes (CNTs) in research and industry has captured the attention of the environmental community. While the risks associated with CNT release to the environment may be a cause for concern (157-159), some argue that the potential benefits afforded by CNT use in environmental engineering applications also deserves research exploration (160,161). One benefit, for example, is the potential adsorption capacity of CNTs for trace organic contaminant removal from water (162-177). The strong sorption of small trihalomethane molecules observed by Lu et al. (168) may compete with the activated carbon used at some water treatment plants as CNT costs decline. The  $\pi$ - $\pi$  bonding mechanism driving the sorption of aromatic compounds to CNTs could be advantageous in water treatment and remediation efforts (169-173). Some researchers have also investigated CNTs as a solid-phase extraction medium for quantifying trace concentrations of organic compounds (161,174-176).

Beyond the fields of environmental chemistry and engineering, researchers are exploiting the unique structures of CNTs for their electrical, mechanical, and thermal properties (178-180). For example, poly(vinyl alcohol) (PVA) membranes containing CNTs show improved thermal and mechanical properties compared with the pure polymer (181-185). Ciambelli et al. (182) observed increases in the glass transition and onset of combustion temperatures when CNTs were added to the PVA matrix. CNT-PVA composites also exhibit a higher Young's modulus than pure PVA (184). The addition of CNTs has been observed to promote crystallization in PVA (186), and many of the

improvements observed with CNT addition have been attributed to the increase in crystallinity (184-186).

Polymers are used as physical barriers against environmental contamination in a wide variety of applications (landfill liners, silt screens, vapor intrusion barriers, etc.). Powdered activated carbon (PAC) has been shown to slow the diffusion of some hydrophobic solutes through high-density polyethylene (HDPE) and HDPE sandwich membranes in Chapters 3 and 4. The added sorbent material traps hydrophobic solutes as they dissolve in the polymer and attempt to migrate from the isolated contaminated material and across the barrier membrane, resulting in either an increased time to contaminant breakthrough (Chapter 3) or a reduced contaminant flux (Chapter 4). Because CNTs have also displayed high sorption capacities for hydrophobic organic contaminants, we expect that CNT-containing PVA membranes will exhibit improved barrier performance as well. The first objective of this work is to examine the effect of adding single-walled carbon nanotubes (SWCNTs) to PVA on the breakthrough behavior of 1,2,4-trichlorobenzene (1,2,4-TCB), a model hydrophobic contaminant. While PVA is not typically used for containment in the environment, its high permeability makes it a good candidate to study the mechanisms of contaminant diffusion across sorbent-containing barrier membranes in the laboratory. Breakthrough experiments using PVA membranes containing PAC or SWCNTs are compared to those using pure PVA.

Some researchers have added oxidative functional groups to the surfaces of CNTs to better incorporate them into the hydrophilic PVA structure and have observed further mechanical property improvements in the CNT-PVA composites (181,182). Langley and

Fairbrother (187) studied several oxidation techniques and discovered that the type and strength of the oxidant affected the type of functional groups added to carbon surfaces. Any type of oxidation, however, is expected to decrease the sorptive capacity of CNTs for hydrophobic organics lacking functional groups that participate in hydrogen bonding, such as 1,2,4-TCB (188,189). Cho et al. (188) observed a 70% reduction in naphthalene sorption to multi-walled carbon nanotubes (MWCNTs) with 10% surface oxygen compared with raw MWCNTs. Sorption of non-polar solutes to PAC also decreased with surface oxidation (190,191). The addition of oxidative functional groups is expected to increase CNT and PAC sorption capacities for heavy metal ions (177,189,192-197), another important class of environmental contaminants. The second objective of this work is to examine the barrier performance of PVA membranes containing surface-functionalized SWCNT and PAC (ox-SWCNT and ox-PAC, respectively). Breakthrough experiments for these membranes conducted with 1,2,4-TCB and with  $\text{Cu}^{2+}$  are evaluated.

Finally, while a breakthrough experiment provides information on the barrier performance of a particular sorbent-containing membrane, broader conclusions regarding the use of sorbent particles in barrier membranes can be made with knowledge of the sorption mechanisms of the particles themselves. Sorption isotherms and particle characterization were used to better understand the sorption capabilities, surface chemistry, and the physical microstructure/macrostructure of each sorbent particle type used in this study.

## 5.2 *Experimental Methodology*

### 5.2.1 *Materials*

PVA (Elvanol 71-30) was provided by DuPont. PAC (J.T. Baker) was sieved (150-mesh) prior to use. SWCNT (Short SWNT 90s, 90%, CheapTubes.com) were used as received. Nanopure water (Milli-Q, Millipore) was used in all preparations and experiments. Ammonium persulfate (98.8%), cupric chloride dehydrate (99%), and hexane (65% n-hexane) were obtained from Fisher Scientific. 1,2,4-TCB (99+%) and hydroxylamine hydrochloride (99%) were purchased from Sigma-Aldrich. Sulfuric acid (95.7%), hydrochloric acid (36.5-38%), sodium hydroxide (NaOH, 98.6%), sodium chloride (NaCl, 99.7%), and sodium citrate (100%) were obtained from Mallinckrodt. Tris[hydroxymethyl]aminomethane hydrochloride (TRIZMA-HCl, 99%) was purchased from Sigma. Acetone (99.5%) was purchased from Mallickrodt Baker. Bathocuproinedisulfonic acid disodium hydrate was obtained from Aldrich. Epoxies used to fix and seal membranes into the diaphragm cell apparatus were from Loctite (5-Minute Quick Set) and 3M (DP-125).

### 5.2.2 *Sorbent Particle Preparation*

Functionalized PAC and SWCNTs were prepared as described by Langley and Fairbrother (187). A saturated solution was prepared by stirring 75 g ammonium persulfate with 100 mL 1 M sulfuric acid overnight. Undissolved ammonium persulfate was filtered from the solution with 0.22  $\mu\text{m}$  polyvinylidene fluoride membranes (PVDF, Durapore type GV, Millipore). Particles (0.2 g) were added to 100 mL of the saturated

ammonium persulfate solution, sonicated for 10 minutes (Cole Parmer Ultrasonic Processor, 750W at 30% amplitude) to break up particle agglomerations, and stirred rapidly on a magnetic stir plate for 24 hours. Particles were filtered (0.22  $\mu\text{m}$  PVDF), rinsed with water, and dried in a 70 °C oven.

### 5.2.3 Sorbent Particle Characterization<sup>2</sup>

Brunauer-Emmett-Teller (BET) specific surface area for each particle type was measured via a three-point nitrogen sorption isotherm using a Quantasorb surface area analyzer (Quantachrome).

Raw and functionalized PAC and SWCNTs were characterized using high-resolution transmission electron microscopy (HRTEM) and Raman spectroscopy. Dry sorbent samples were rinsed in isopropyl alcohol, suspended in ethyl alcohol, and sonicated using a Misonix sonic dismembrator. These suspensions were placed in a bath sonicator for 5 minutes before the imaging was performed. A drop of each suspension was placed on a 200-mesh copper transmission electron microscopy (TEM) grid coated with an amorphous carbon holey film (SPI Supplies) and allowed to dry for 2 minutes. Excess solvent was removed by wicking with filter paper. Images were collected using a JEOL JEM-2100F 200kV Schottky field emission gun HRTEM with a point resolution of 0.19 nm.

---

<sup>2</sup> HRTEM images and Raman spectra were collected and interpreted by Ifthekeer A. Khan (Department of Civil and Environmental Engineering, University of South Carolina), Atif A. Choudhury (Department of Medicine, Health, and Society, Vanderbilt University), and Navid B. Saleh (Department of Civil and Environmental Engineering, University of South Carolina).

Raman spectra were recorded for PAC, SWCNT, and their functionalized counterparts using a LabRam confocal Raman spectrophotometer (JY Horiba) equipped with a liquid nitrogen-cooled, charged coupled device detector and an He/Ne (632.817 nm) laser for excitation. Each spectrum represents the average of at least 5 scans with integration times of 15 seconds each.

#### *5.2.4 Membrane Preparation*

Pure PVA and sorbent-containing PVA membranes were prepared by sonicating sorbent particles in 15 mL water for 10 minutes before adding 1.5 g PVA. The particle/PVA suspension was heated (<100 °C) while stirring rapidly for 10 minutes, cooled, degassed under vacuum, and cast on a polytetrafluoroethylene (PTFE) plate. After drying at room temperature for 2 days, the PVA was crosslinked in a 150 °C oven for 1 hour. Thicknesses of hydrated membranes were measured with a micrometer (Mitutoyo).

#### *5.2.5 Batch and Breakthrough Experiments*

All 1,2,4-TCB experiments were conducted in nanopure water. Cu<sup>2+</sup> experiments were conducted in pH 7.2 50 mM Tris buffer (7.88 g/L TRIZMA-HCl; 0.18 g/L NaOH; 5.85 g/L NaCl). Batch experiment initial concentrations and breakthrough experiment upstream concentrations were 50 µM and 1 mM for all 1,2,4-TCB and Cu<sup>2+</sup> experiments, respectively.

Equilibrium experiments were conducted for particles and membranes. For each isotherm, a series of vials was loaded with particles or dry membrane pieces with varying mass. Vials were filled with liquid medium, and membranes were allowed to hydrate overnight before spiking with a concentrated stock solution to achieve the desired initial concentration. Particle equilibrium vials were placed on a rotator or handshaken twice daily for at least 6 days prior to sampling.  $\text{Cu}^{2+}$  samples (100  $\mu\text{L}$ ) were filtered with a 0.22  $\mu\text{m}$  nylon syringe filter (Acrodisc). 1,2,4-TCB samples (250  $\mu\text{L}$ ) were collected after either centrifugation at 900 g for 15 minutes or allowing particles to settle for 48 hours. Membrane partitioning/isotherm experiments were stored on a shaker table for at least 24 and 5 days for 1,2,4-TCB and  $\text{Cu}^{2+}$  experiments, respectively, before collecting of 250- $\mu\text{L}$  and 100- $\mu\text{L}$  samples from each.

Batch uptake experiments were conducted by placing equal mass pieces of dry membrane into a series of vials and adding the appropriate liquid medium. After overnight hydration, each vial was spiked with concentrated stock solution and samples were collected through each experiment, sampling each vial once. Sample volumes were equivalent to those for equilibrium experiments.

Breakthrough experiments were conducted by placing hydrated membranes between two diaphragm cells, filling the cells with the appropriate liquid medium, and sealing the joint with epoxy. The upstream cell was spiked with either a concentrated 1,2,4-TCB stock solution in acetone or a concentrated cupric chloride solution in Tris buffer to achieve the desired initial upstream concentration. Downstream samples (500  $\mu\text{L}$ ) were collected throughout each experiment and were replaced with clean liquid

medium to maintain a constant downstream volume.  $\text{Cu}^{2+}$  experiment upstream samples were also collected in this manner. Fifty-microliter samples were collected from 1,2,4-TCB experiment upstream cells without replacement.

#### *5.2.6 Sample Extraction and Analysis*

1,2,4-TCB samples were extracted with 1 mL hexane by vortex mixing for 60 sec. The extraction efficiency of this procedure was 79% for 500  $\mu\text{L}$  samples, 100% for 250  $\mu\text{L}$  samples, and 98% for 50  $\mu\text{L}$  samples. Most breakthrough and uptake experiment extracts were analyzed on a Hewlett Packard 5890A gas chromatograph equipped with an electron capture detector (oven temperature at 100 °C for 2 min, 15 °C/min to 160 °C, 5 °C/min to 235 °C, hold for 3 min, 15 °C/min to 270 °C, hold for 2 min). Two-microliter samples were injected to a splitless inlet at 225 °C on an HP-5 column (30 m  $\times$  0.32 mm i.d.  $\times$  0.25  $\mu\text{m}$  film thickness, J&W). Equilibrium experiment and some breakthrough experiment extracts were analyzed on a Hewlett Packard G1800A gas chromatograph using mass spectrometry (MS) for analyte detection (oven temperature at 100 °C for 2 min, 15 °C/min to 160 °C, 5 °C/min to 235 °C, hold for 3 min, 15 °C/min to 270 °C, hold for 2 min). Two-microliter samples were injected to a splitless inlet at 225 °C on an RTX-5 column (30 m  $\times$  0.25 mm i.d.  $\times$  0.25  $\mu\text{m}$  film thickness, Restek). The MS was set for the detection of ions with mass/charge ratios of 145, 180, and 182. Calibration was accomplished with a set of 8-12 trichlorobenzene standards in hexane.

$\text{Cu}^{2+}$  breakthrough experiment upstream samples were diluted to 24.5 mL. All other  $\text{Cu}^{2+}$  experiment samples were diluted to 3.5 mL.  $\text{Cu}^{2+}$  concentrations in 3.5-mL aliquots

of each dilution were measured using the bathocuproine method (198) and a Shimadzu UV-1601PC spectrophotometer. The measurement was calibrated using a set of 8 cupric chloride standards.

### 5.3 Results

#### 5.3.1 Particle Characterization

Table 5-1 lists BET specific surface areas for each sorbent particle type. Oxidation was completed in small batches, and several batches of ox-PAC and ox-SWCNT were needed to complete the breakthrough, uptake, and isotherm experiments described below. While the surface areas for ox-PAC listed in Table 5-1 disagree, sorption tests confirmed that the two batches achieved the same per mass sorption capacity. Other researchers have compared BET specific surface areas for raw and functionalized particles with mixed results—some observed increases in surface area upon oxidation (167) and others have observed surface area reduction (169,192). We suspect the Batch 1 value given in

**Table 5-1.** Sorbent particle characteristics

	BET Specific Surface Area (m <sup>2</sup> /s)
PAC	1100±90
SWCNT	380±10
ox-PAC	
Batch 1	102±8
Batch 2	700±100
ox-SWCNT	
Batch 1	400±100
Batch 2	410±50

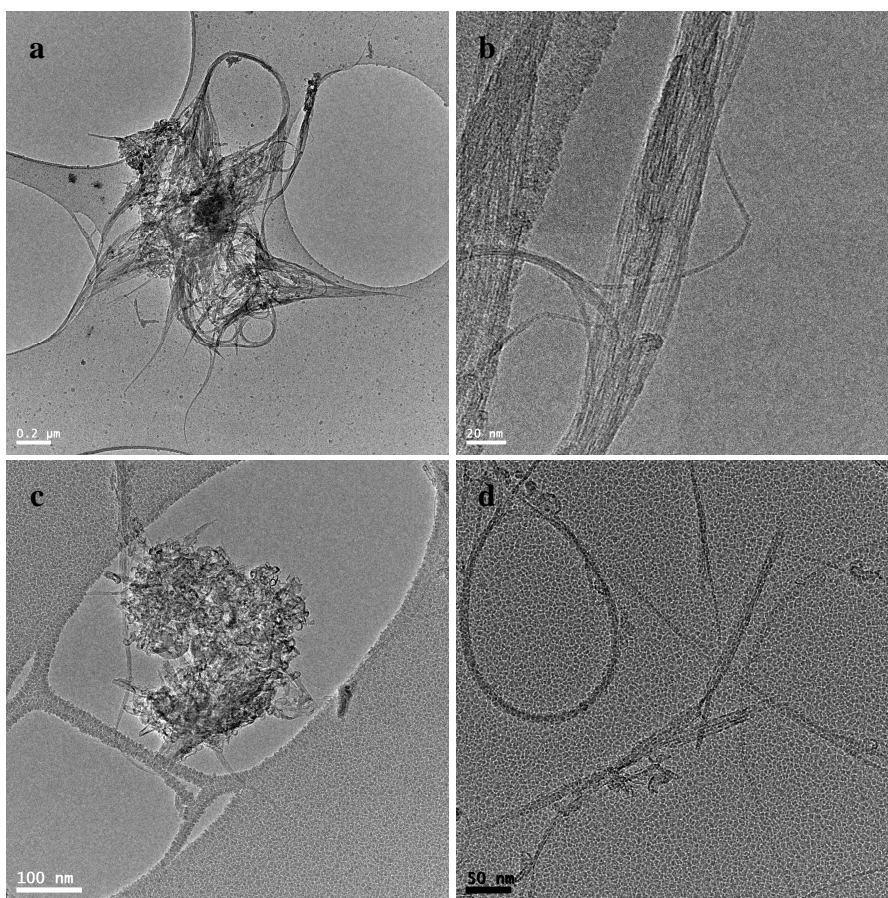


**Figure 5-1.** HRTEM images of representative SWCNT (a-b) and ox-SWCNT (c-d). The wide angle view shows comparative cluster sizes (a and c) and the high resolution view presents the bundling state of the clusters (b and d).

Table 5-1 for ox-PAC to be erroneous, as no other researchers have observed 7-fold differences between the two.

HRTEM imaging of SWCNTs (Figure 5-1a) shows highly bundled clusters (cluster size of a few microns) with long nanotubes entangled with one another. Figure 5-1b shows a high resolution image, which also confirms a highly bundled state. The lattice spacing is on the order of 0.8-2 nm, which confirms that most of the tubes are single-

walled. The cluster size is reduced to a few hundred nanometers after functionalization (Figure 5-1c). The sharp and uncapped features of the ox-SWCNTs shown in Figures 5-1c and 5-1d are another result of the oxidation procedure. Acid etching debundled and shortened the ox-SWCNTs significantly. Similar observations were made for PAC and ox-PAC. PAC samples formed clusters that are microns in size (Figure 5-2a). Deeply clustered morphology is presented in a representative high resolution image in Figure

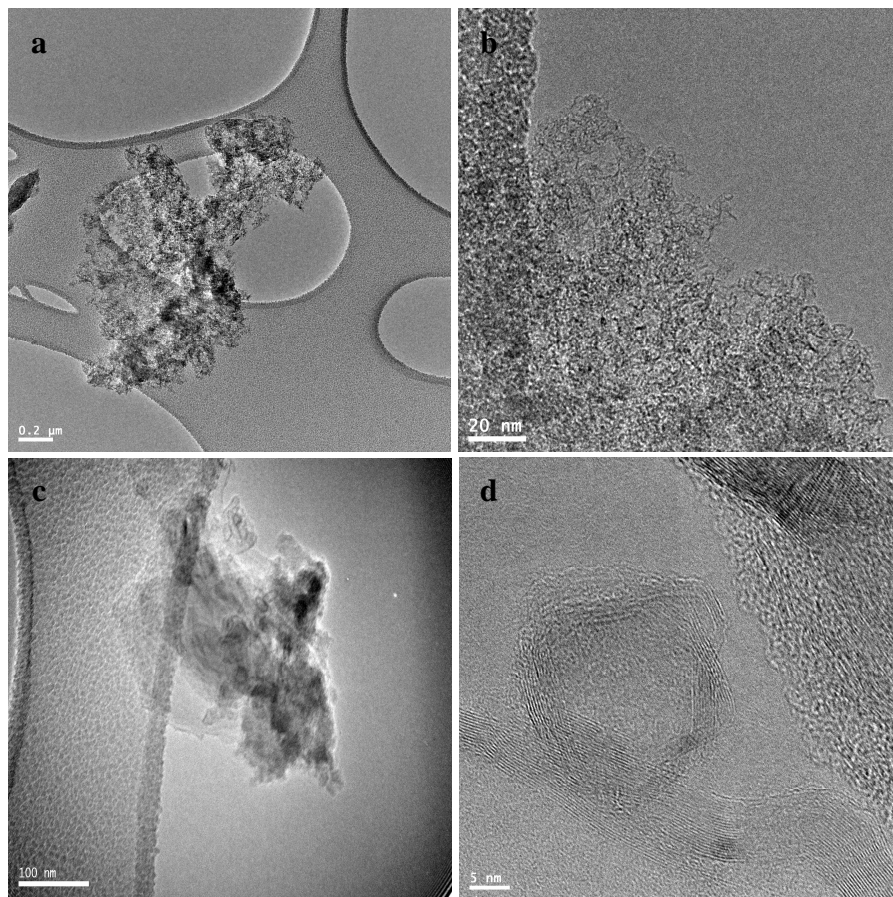


**Figure 5-2.** HRTEM images of representative PAC (a-b) and ox-PAC (c-d). The wide angle view shows comparative cluster sizes (a and c) and the high resolution view presents the morphological state of the clusters (b and d).

5-2b. Functionalization declustered the PAC significantly (Figures 5-2c and 5-2d), with cluster sizes on the order of 100 nm.

Raman spectra (shown in Appendix D) were used to estimate SWCNT diameters of 1.1-1.5 nm (199-203). Differences in spectra for raw and functionalized SWCNTs indicate an increase in defect level as expected with the addition of functional groups (204). Differences in Raman spectra for raw and functionalized PAC were consistent with those reported previously (205,206).

### 5.3.2 Sorption Isotherms

To understand the impact of sorbent particles in a membrane barrier, it is useful to understand their sorption capabilities outside of the membrane matrix. Sorption isotherm data were collected and fit to the Langmuir isotherm model using the least-squares fitting option in Scientist for Windows (MicroMath). Isotherm data and Langmuir fit curves are shown in Figures 5-3 through 5-5.

We suspect the high  $\text{Cu}^{2+}$  concentration data points (open symbols in Figure 5-5) are the result of experimental error, because these experiments required weighing of very small amounts of particles using a balance that measures down to 0.1 mg. For example,  $q$  was calculated from the measured aqueous  $\text{Cu}^{2+}$  concentration and the mass of particle initially added to each vial. The mass of ox-PAC added to the “outlier” vial was 0.0001 g. If the mass was actually 0.0002 g,  $q$  is halved, resulting in a value that is much more reasonable considering the rest of the isotherm data. Thus, these data points were omitted from the Langmuir fitting data set.

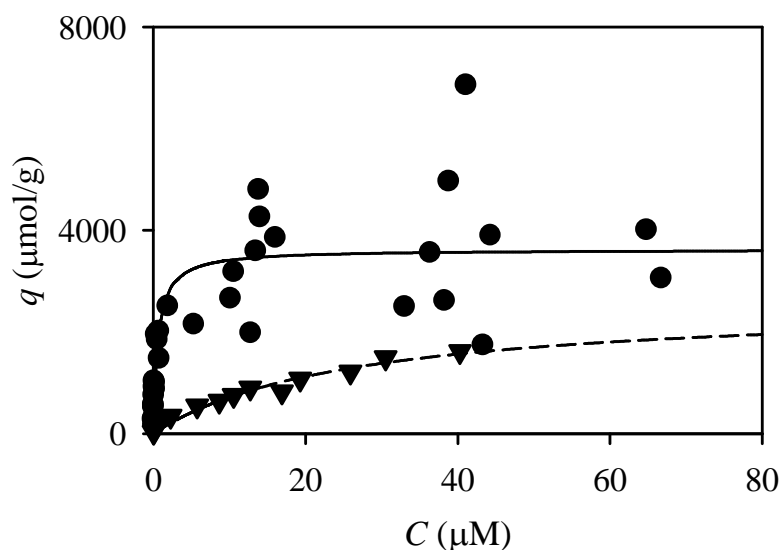


**Figure 5-3.** Isotherm data for 1,2,4-TCB sorption to PAC (●) and SWCNT (▼). Langmuir isotherm fits with  $q_{\max}=3600\pm500$   $\mu\text{mol/g}$  and  $b=2\pm1$   $\text{L}/\mu\text{mol}$  for PAC (—) and with  $q_{\max}=2600\pm800$   $\mu\text{mol/g}$  and  $b=0.04\pm0.02$   $\text{L}/\mu\text{mol}$  for SWCNT (--) are included.

Isotherm experiments using pure and sorbent-containing PVA membranes were also conducted, though the scatter present in the data obtained makes it difficult to make any quantitative conclusions. (These isotherms may be viewed in Appendix C.) Overall, however, the observed sorption capacity of the membrane-bound sorbent particles was lower than expected based on the isotherm data shown in Figures 5-3 through 5-5 and on the final concentrations observed in the uptake experiments described below.

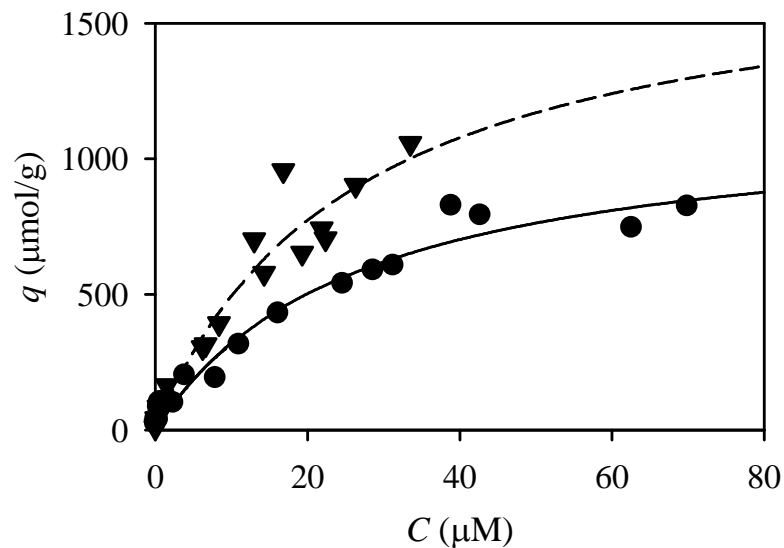


**Figure 5-4.** Isotherm data for 1,2,4-TCB sorption to ox-PAC (●) and ox-SWCNT (▼). Langmuir isotherm fits with  $q_{\max}=1200\pm300$   $\mu\text{mol/g}$  and  $b=0.04\pm0.02$   $\text{L}/\mu\text{mol}$  for ox-PAC (—) and with  $q_{\max}=1800\pm900$   $\mu\text{mol/g}$  and  $b=0.04\pm0.03$   $\text{L}/\mu\text{mol}$  for ox-SWCNT (---) are included.

### 5.3.3 Breakthrough Curves

Breakthrough curves for 1,2,4-TCB and  $\text{Cu}^{2+}$  across pure PVA membranes and those containing sorbent particles are shown in Figures 5-6 and 5-7, respectively. The slope of each curve is equivalent to the permeability of the membrane, a result of normalizing the data according to Equation 3-1.

$$\frac{C_{\text{down}}V_{\text{down}}}{C_{\text{up}}AL} = \frac{P}{L^2}(t - t_{\text{lag}}) \quad (3-1)$$

Permeabilities, observed lag times, and other experimental information are given in Table 5-2.

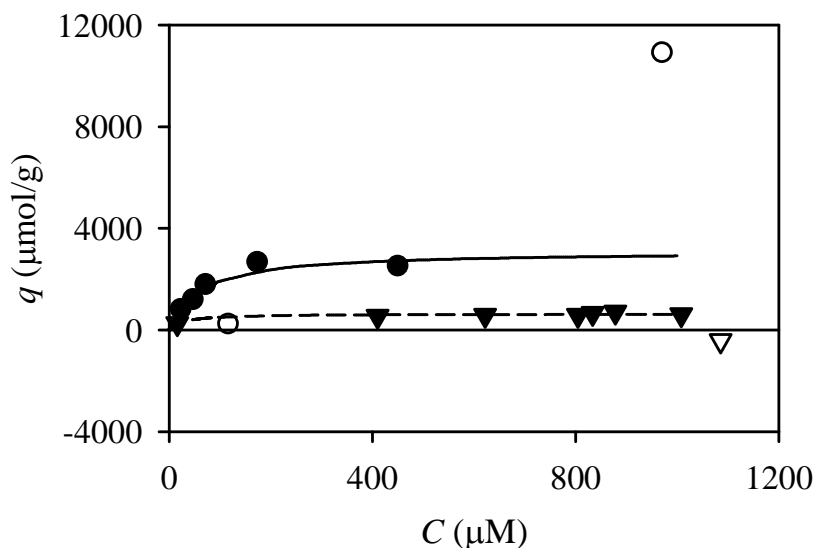


**Figure 5-5.** Isotherm data for  $\text{Cu}^{2+}$  sorption to ox-PAC (●) and ox-SWCNT (▼). Langmuir isotherm fits with  $q_{\text{max}}=3000\pm 1000 \mu\text{mol/g}$  and  $b=0.02\pm 0.02 \text{ L}/\mu\text{mol}$  for ox-PAC (—) and with  $q_{\text{max}}=630\pm 70 \mu\text{mol/g}$  and  $b=0.04\pm 0.04 \text{ L}/\mu\text{mol}$  for ox-SWCNT (---) are included. Open symbols represent data that were omitted from the Langmuir fitting data set.

#### 5.3.4 Membrane Uptake Curves

The effect of sorptive particle addition to barrier membranes is dependent on both a high sorption capacity and on fast sorption kinetics. To explore differences in the rate of contaminant uptake by membrane-bound particles, membrane uptake experiments were conducted. Figures 5-8 and 5-10 present normalized uptake data as measured by concentration loss in aqueous solution. Figures 5-9 and 5-11 may be used to estimate pseudo-first-order uptake rates for each of the contaminant/particle combinations.

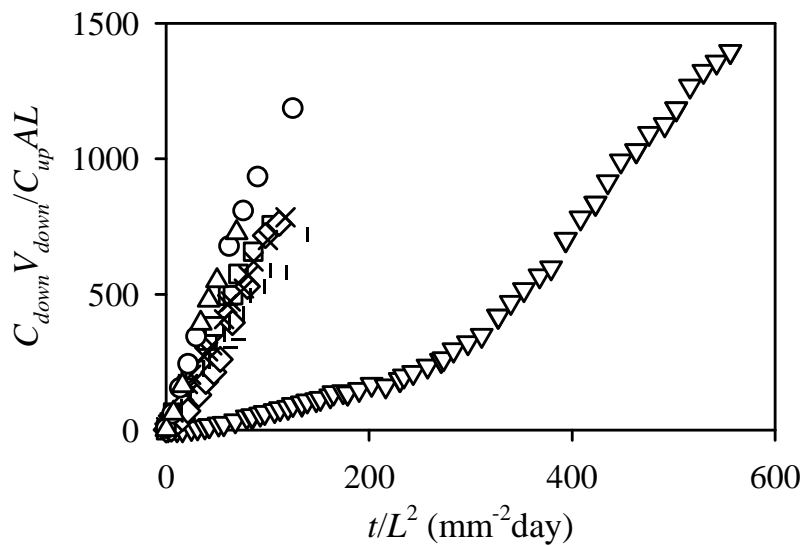


**Figure 5-6.** Normalized 1,2,4-TCB breakthrough curves for pure PVA (—, □), PVA with 32 (△) or 69 g/L PAC (▽), PVA with 77 (◇) or 141 g/L SWCNT (○), PVA with 62 g/L ox-PAC (|), and PVA with 42 g/L ox-SWCNT (×).

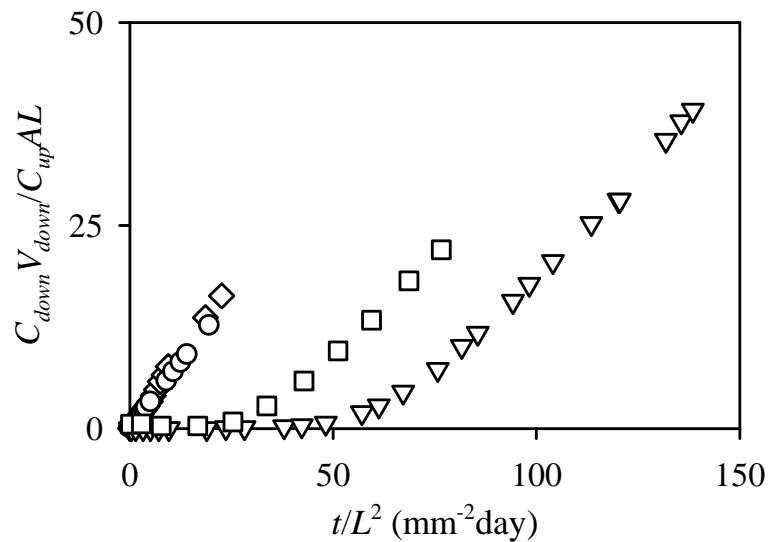


**Figure 5-7.** Normalized  $\text{Cu}^{2+}$  breakthrough curves for pure PVA (○, ◇), PVA with 186 g/L ox-PAC (▽), and PVA with 157 g/L ox-SWCNT (□).

**Table 5-2.** Breakthrough experiment data<sup>a</sup>

Solute	Sorbent	$C_{s0}$ (g/L)	$L$ ( $\mu\text{m}$ )	$C_{up}$ ( $\mu\text{M}$ )	$P \times 10^{12}$ ( $\text{m}^2/\text{s}$ )	$t_{lag}$ (hr)	PVA $t_{lag}$ (hr) <sup>b</sup>
1,2,4-TCB	-	-	186 $\pm$ 5	52 $\pm$ 1	63 $\pm$ 3	0.1 $\pm$ 0.6	-
1,2,4-TCB	-	-	222 $\pm$ 5	47 $\pm$ 3	94 $\pm$ 8	0 $\pm$ 2	-
1,2,4-TCB	PAC	32	168 $\pm$ 4	44 $\pm$ 5	140 $\pm$ 20	2 $\pm$ 1	0.10
1,2,4-TCB	PAC <sup>c</sup>	69	270 $\pm$ 20	44 $\pm$ 2	11 $\pm$ 1	51 $\pm$ 7	0.3
				53 $\pm$ 2	40 $\pm$ 4	370 $\pm$ 6	
1,2,4-TCB	SWCNT	77	250 $\pm$ 10	48 $\pm$ 6	70 $\pm$ 10	14 $\pm$ 5	0.2
1,2,4-TCB	SWCNT	141	126 $\pm$ 6	48 $\pm$ 4	140 $\pm$ 20	0.8 $\pm$ 0.6	0.06
1,2,4-TCB	ox-PAC	62	222 $\pm$ 5	48 $\pm$ 4	70 $\pm$ 9	6 $\pm$ 6	0.2
1,2,4-TCB	ox-SWCNT	42	227 $\pm$ 6	48 $\pm$ 2	82 $\pm$ 8	-2 $\pm$ 5	0.2
$\text{Cu}^{2+}$	-	-	230 $\pm$ 10	1220 $\pm$ 10	8.7 $\pm$ 0.5	0.4 $\pm$ 0.3	-
$\text{Cu}^{2+}$	-	-	328 $\pm$ 8	1260 $\pm$ 20	7.5 $\pm$ 0.2	1.0 $\pm$ 0.2	-
$\text{Cu}^{2+}$	ox-PAC	186	230 $\pm$ 3	970 $\pm$ 10	5.5 $\pm$ 0.2	77 $\pm$ 3	0.5
$\text{Cu}^{2+}$	ox-SWCNT	157	85 $\pm$ 4	998 $\pm$ 9	5.5 $\pm$ 0.2	5.4 $\pm$ 0.2	0.06

<sup>a</sup> Errors given are 95% confidence intervals.

<sup>b</sup> PVA  $t_{lag}$  is a predicted value for pure PVA with the same thickness as the membrane studied.

<sup>c</sup> 1,2,4-TCB breakthrough across PAC-containing PVA occurred in three distinct phases: 1) the lag time, 2) a period of low apparent permeability, and 3) permeability similar to that observed for pure PVA. The two rows of information given are the result of applying Equation 2-3 to data in the latter two phases.

## 5.4 Discussion

### 5.4.1 Sorption Mechanisms

The sorption isotherms described in Figures 5-3 through 5-5 provide some initial insight into the interactions between solutes and the sorbent particles used in this study, which may improve our understanding of the membrane breakthrough experiment data. For example, the isotherm data for  $\text{Cu}^{2+}$  clearly follows the Langmuir isotherm model. Langley and Fairbrother (187) studied several oxidation processes and concluded that oxidation with persulfate results in a high concentration of carboxylic acid groups on the

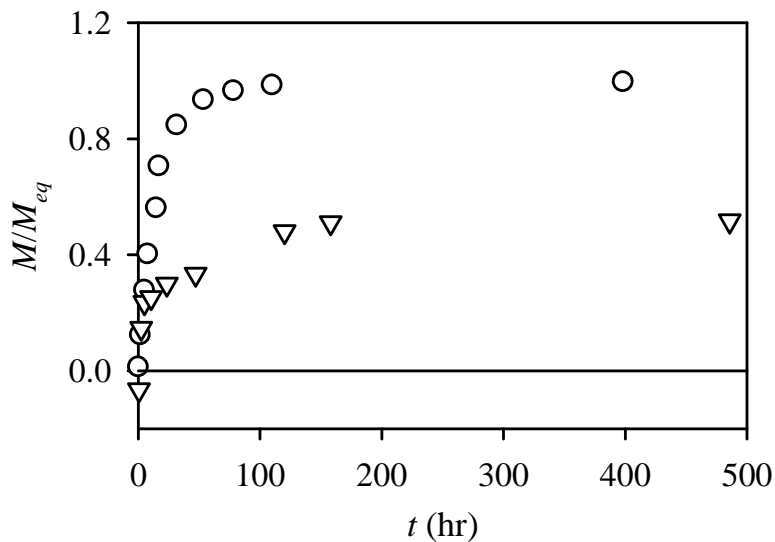


**Figure 5-8.** Normalized membrane uptake curves for 1,2,4-TCB using membranes containing 69 g/L PAC (○) or 77 g/L SWCNT (▽).  $M$  is the sorbed contaminant mass and  $M_{eq}$  is the expected mass sorbed to the membrane-bound particles at equilibrium.

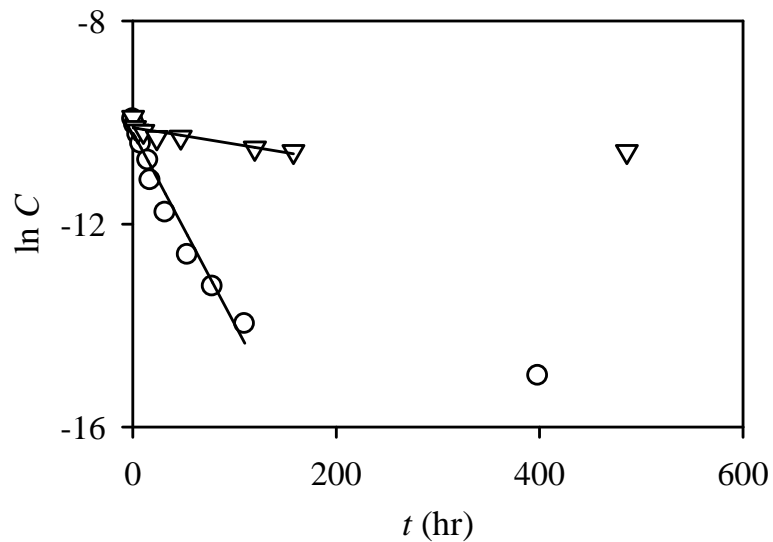


**Figure 5-9.** Pseudo-first-order kinetic plot for 1,2,4-TCB uptake by PVA membranes containing 69 g/L PAC (○) or 77 g/L SWCNT (▽).

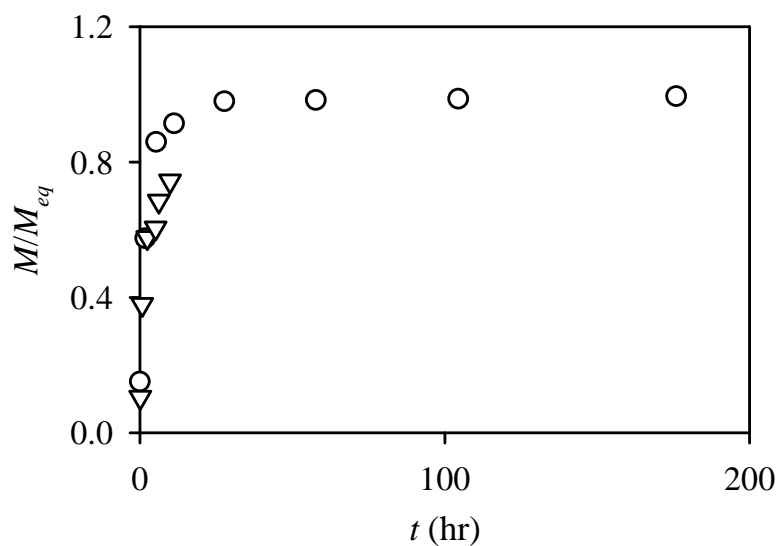


**Figure 5-10.** Normalized membrane uptake curves for  $\text{Cu}^{2+}$  using membranes containing 186 g/L ox-PAC (○) or 157 g/L ox-SWCNT (▽).  $M$  is the sorbed contaminant mass and  $M_{eq}$  is the expected mass sorbed to the membrane-bound particles at equilibrium.

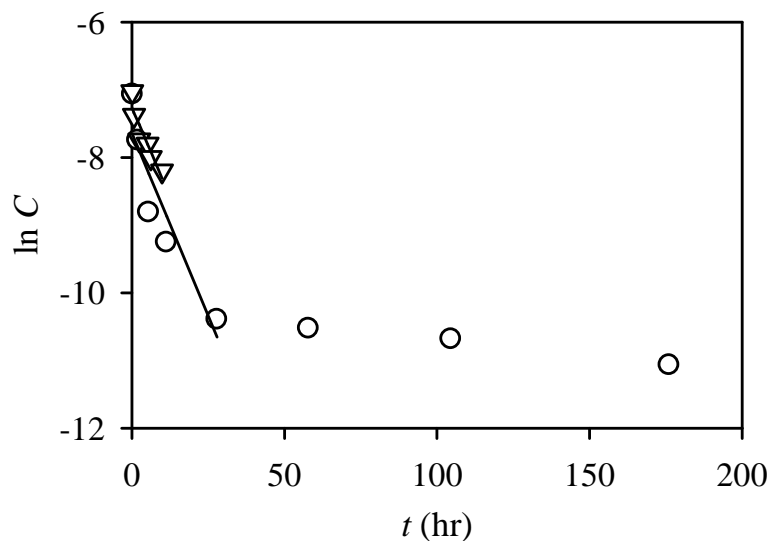


**Figure 5-11.** Pseudo-first-order kinetic plot for  $\text{Cu}^{2+}$  uptake by PVA membranes containing 186 g/L ox-PAC (○) or 157 g/L ox-SWCNT (▽).

surface.  $\text{Cu}^{2+}$  binds easily to carboxylic acid groups, not only because these groups increase the ability for hydrogen bonding with water surrounding the  $\text{Cu}^{2+}$  ion, but because deprotonation of the carboxylic acid groups at neutral pH creates a negative charge that attracts the metal cation (189). This electrostatic attraction ceases when enough  $\text{Cu}^{2+}$  molecules are present to neutralize the surface, leading to the obvious plateau in the sorption isotherms at  $q_{\text{max}}$  for both ox-PAC and ox-SWCNT (Figure 5-5).

The  $\pi$ - $\pi$  interactions thought to drive aromatic sorption to CNTs are best described by a monolayer Langmuir sorption isotherm model (162). Hydrophobic interactions, however, may allow for the weak adsorption of additional layers, leading many researchers to report Freundlich isotherm fitting parameters for aromatic sorption to CNTs (163,170,173,176). The Freundlich isotherm model is a semi-empirical exponential model that is often used to describe non-linear adsorption that does not plateau like the monolayer Langmuir model:

$$q = K_F C^{1/n} \quad (5-2)$$

where  $K_F$  and  $n$  are both fitted parameters. Whether the data in Figures 5-3 (sorption to PAC and SWCNT) exhibit more Freundlich-type character or more Langmuir-type character is difficult to say with certainty without data at higher concentrations.

Freundlich fits (not shown) resulted in similar  $R^2$  values as the Langmuir fits given. The lack of a sorption plateau is even more apparent for 1,2,4-TCB sorption to the functionalized particles (Figure 5-4), possibly because the first layer of sorption to the functionalized surfaces of ox-PAC and ox-SWCNT is also weak. Additional layers may

sorb more strongly to the now hydrophobic surface, leading to sorption increases even at higher concentrations.

#### 5.4.2 Factors Controlling 1,2,4-TCB Sorption and Diffusion in PVA

The PVA membrane with 69 g/L PAC was the only sorbent-containing membrane with a measurably different 1,2,4-TCB breakthrough curve than the pure polymer, as shown in Figure 5-6. Fast “reaction” relative to diffusion should result in increased lag times as observed previously (47), but slower “reaction” can lead to reduced flux, as shown in Chapter 4. In Chapter 4, the rate of 1,2,4-TCB sorption to HDPE-bound PAC was attributed to kinetic limitations associated with diffusion from the bulk membrane to the particle surface. This may not be the case in PVA, however, as  $D$  in PVA ( $1.3 \times 10^{-11}$  m<sup>2</sup>/s) is over 200 times larger than  $D$  in HDPE ( $6 \times 10^{-14}$  m<sup>2</sup>/s).

The relative kinetic differences between 1,2,4-TCB sorption to PVA-encapsulated PAC and SWCNTs have been captured in the uptake experiments described in Figure 5-8. Assuming pseudo-first-order sorption kinetics, the plot shown in Figure 5-9 can be used to estimate the relative pseudo-first-order rate constants,  $k_1$ , for each sorbent type. Because diffusion also plays a part in these membrane-based uptake experiments,  $k_1$  determined using this method is not an actual sorption rate constant. The relative differences between  $k_1$  derived from PAC and SWCNT data, however, may provide some useful information. Further, relative second-order rate constants can be calculated:

$$k_2 = \frac{k_1}{C_{s0} q_{\max}} \quad (5-2)$$

where the product,  $C_{s0}q_{\max}$ , is the sorptive capacity per active membrane volume. Relative  $k_2$  values are given in Table 5-3. Relative Damköhler numbers,  $\Phi$ , were calculated using Equation 5-3, which is a modified version of Equation 2-10 that accounts for the stoichiometric differences in sorption capacity afforded by the different sorbent materials.

$$\Phi = \frac{k_2 C_{s0} q_{\max} L^2}{D} \quad (5-3)$$

$$\Phi = \frac{k_2 C_{s0} L^2}{D} \quad (2-10)$$

The values of  $k_2$  given in Table 5-3 for uptake of 1,2,4-TCB by membrane-bound SWCNT may be doubled if the reduction in capacity observed in Figure 5-10 is also considered.

Typically, Damköhler numbers should be above 0.01 for any visible barrier improvements (and above 100 to show increased lag time-type behavior) with the addition of an active scavenger (3). The values in Table 5-3 are relative numbers based on relative kinetic data, and thus the absolute values of  $\Phi$  reported in Table 5-3 cannot be

**Table 5-3.** Relative second-order sorption rate constants and Damköhler numbers for some experimental membranes

Solute	Sorbent	$C_{s0}$ (g/L)	$L$ ( $\mu\text{m}$ )	Relative $k_2$ (L/ $\mu\text{mol}\cdot\text{s}$ )	Relative $\Phi$
1,2,4-TCB	PAC	32	168 $\pm$ 4	4.2 $\times 10^{-11}$	0.011
1,2,4-TCB	PAC	69	270 $\pm$ 20	4.2 $\times 10^{-11}$	0.061
1,2,4-TCB	SWCNT	77	250 $\pm$ 10	4.5 $\times 10^{-12}$	0.005
1,2,4-TCB	SWCNT	141	126 $\pm$ 6	4.5 $\times 10^{-12}$	0.002
Cu <sup>2+</sup>	ox-PAC	186	230 $\pm$ 3	5.2 $\times 10^{-11}$	0.298
Cu <sup>2+</sup>	ox-SWCNT	157	85 $\pm$ 4	3.0 $\times 10^{-10}$	0.040

compared to this theoretical range. Because  $\Phi$  for the membrane with 69 g/L PAC was more than 5 times higher than for the rest of the 1,2,4-TCB breakthrough experiments, however, it is easy to conclude that kinetics are the reason this sorptive membrane showed barrier improvements while the others did not. A reduced sorbent loading and a thinner membrane contributed to the low Damköhler number for the membrane with 32 g/L PAC. Higher loadings were used for the SWCNT-containing PVA membranes in an attempt to counteract the effects of the sorbent's slightly lower capacity for 1,2,4-TCB sorption (shown in Figure 5-5), but the kinetics of 1,2,4-TCB sorption to PVA-bound SWCNTs were clearly too slow to lead to improved barrier performance.

There are several possible explanations for the slow sorption rate to membrane-bound SWCNTs. For example, the rate of sorption to the outer surface sites on an SWCNT cylinder will obviously be faster than the rate of sorption to the inner sites, especially for bulky compounds like 1,2,4-TCB that must diffuse, maybe one molecule at a time, through the tube end to access the inner surface sites. (The LeBas molar volume of aqueous 1,2,4-TCB is  $147.6 \text{ cm}^3/\text{mol}$  (207), so a "spherical" molecule would have a diameter of 0.78 nm. SWCNT tube diameter determined using the Raman spectra ranged from 1.1-1.5 nm.) In fact, the  $M_{eq}$  values in Figure 5-8 were calculated for the uptake experiments using the free solution sorption isotherms shown in Figure 5-3. The leveling of the SWCNT data in Figure 5-8 at  $M/M_{eq} = 0.5$  suggests that 1,2,4-TCB cannot easily access the inner surfaces when embedded in PVA. This effect accounts for a two-fold difference in sorption rate, but the observed second-order sorption rate constants for PAC and SWCNT differ by a factor of 10. Tight bundling of SWCNTs may also impede 1,2,4-

TCB access to some outer SWCNT surfaces, slowing sorption to the interstitial surfaces. Finally, imperfections in the SWCNT structure, such as metals and functional groups, may interact with functional groups in PVA. If this interaction is stronger than interactions with water, sorption sites that are easily available in water may be more difficult for the 1,2,4-TCB to access in the PVA matrix.

Functional groups intentionally added to PAC and SWCNT surfaces reduced their sorption capacities for 1,2,4-TCB (Figure 5-4). This result was expected given that functional groups reduce the aromatic and hydrophobic nature of carbon sorbents. Thus, ox-PAC and ox-SWCNT were unsuccessful at quantifiably intercepting 1,2,4-TCB as it diffused across the PVA membranes.

One last feature of Figure 5-6 worth noting is the observed transition from reduced flux to a steady-state flux (nearly parallel to the pure PVA membrane breakthrough curve). This transition occurred after an estimated 37% of the total sorption capacity of the PAC was occupied by 1,2,4-TCB, as calculated from the area between the observed breakthrough curve (at pseudo-steady-state) and the curve expected for a pure PVA membrane of the same thickness. Somewhat similar PAC usage rates were observed in the sandwich membranes described in Chapter 3. Breakthrough across this membrane can also be described by the moving reactive front model if the “leakage” during the low, pseudo-steady-state flux period is ignored. In this case, the linear portion of the higher-flux period is fit to Equation 2-3 to determine the second lag time for this experiment given in Table 5-2.

$$\frac{C_{down}}{C_{up}} = \frac{DHA}{LV_{down}} (t - t_{lag}) \quad (2-3)$$

The effective  $C_{s0}$  determined using Equation 2-9 is 29 g/L, or 42% of the actual  $C_{s0}$  determined during membrane preparation and given in Table 5-2.

$$t_{lag} = \frac{L^2 C_{s0} q_{max}}{2DH(C_{up} - C_e)} \quad (2-9)$$

Thus, if sorbent efficiency (measured as % usage) is of interest, it appears as if either method of calculation may be used.

#### 5.4.3 Factors Controlling $Cu^{2+}$ Sorption and Diffusion in PVA

Functionalized sorbent loadings were also increased for the purpose of conducting  $Cu^{2+}$  breakthrough experiments in order to overcome the lower sorption capacity of ox-SWCNTs for  $Cu^{2+}$  sorption. This increase resulted in breakthrough curves displaying moving reactive front-type behavior, as shown by the increased membrane lag times observed in Figure 5-7. Relative Damköhler numbers were also determined for the ox-PAC and ox-SWCNT-containing membranes used for the  $Cu^{2+}$  breakthrough experiments (Table 5-3). Relative  $\Phi$  for  $Cu^{2+}$  cannot be compared with relative  $\Phi$  for 1,2,4-TCB directly, because  $D$  for  $Cu^{2+}$  ( $5.3 \times 10^{-12}$  m<sup>2</sup>/s) is lower than  $D$  for 1,2,4-TCB ( $1.3 \times 10^{-11}$  m<sup>2</sup>/s). The  $k_2$  values determined from data in Figures 5-9 and 5-11 are lower than the actual second-order sorption rate constants because of the added influence of membrane diffusion in these experiments. Thus, if we were to correct the relative  $\Phi$  values in Table 5-3, the correction factor for  $Cu^{2+}$  values should be larger than the correction factor for

1,2,4-TCB values, because diffusion has a larger influence of  $\text{Cu}^{2+}$  uptake. The result is that corrected  $\Phi$  values for both  $\text{Cu}^{2+}$  experiments are larger than  $\Phi$  for the 1,2,4-TCB experiments, which probably explains the difference in breakthrough behavior for the two solutes.

Effective  $C_{s0}$  calculated from the observed lag times using Equation 2-9 were 17 and 46 g/L (9 and 29% of the actual  $C_{s0}$ ) for ox-PAC and ox-SWCNT, respectively. The faster relative second-order sorption rate constant,  $k_2$ , for sorption to ox-SWCNT may explain the higher per-capacity effectiveness of the ox-SWCNT. The ox-PAC, however, was more effective per mass because of its much higher sorption capacity for  $\text{Cu}^{2+}$ .

#### *5.4.4 Implications*

While PVA membranes are typically not used as contaminant barriers, PVA was used in this study to provide an easy, side-by-side comparison of the sorbents (PAC, SWCNT, and their functionalized counterparts). SWCNT-containing PVA performed poorly compared with PAC in PVA when used for 1,2,4-TCB containment. The effectiveness of membrane-bound SWCNT, however, might be different in an alternative membrane matrix. While other materials may improve the efficiency of SWCNT, vast improvements in barrier properties with the addition of SWCNT are unlikely. Future research on sorbent-containing membrane barriers for hydrophobic organics is best focused on using coke, activated carbon, and other less expensive materials with high sorption capacities.

For the PVA films used in the chemical engineering industry, the addition of functionalized CNT for mechanical purposes may also slightly improve the films' barrier protection against cations. PVA, however, is typically used dry as a low permeability barrier for gases. For this application, the addition of raw CNT (as opposed a functionalized version) may slightly reduce organic vapor penetration while improving the mechanical properties of the film. Ni et al. (183) found that CNT dispersion in PVA could be improved with the addition of gum arabic and resulted in a film with the same mechanical properties as PVA with functionalized CNT. Regardless, the addition of SWCNTs or ox-SWCNTs for the sole purpose of barrier improvement is impractical.

## **Chapter 6**

### **Conclusions**

## **6.1 *Benefits of Active Barriers***

This work has demonstrated the ability of active scavengers to improve containment of organic environmental contaminants using geomembrane barriers by either increasing the lag time to contaminant breakthrough (delaying contaminant leakage to the environment) or reducing contaminant flux (cumulative leakage) through the geomembranes. The addition of scavengers to membranes can be optimized for the containment of a specific contaminant or contaminant class by choosing a scavenger with optimal “reactivity” toward the contaminant, placing that scavenger in a membrane matrix suitable for promoting “reaction”, and, if necessary, layering the active membrane with high-density polyethylene (HDPE) or another durable geomembrane to provide an effective, low-permeability composite barrier.

## **6.2 *Challenges in Active Barrier Design***

The experimental results described in Chapters 3 through 5 have also highlighted some challenges associated with designing active barriers for contaminant containment. Both kinetics and stoichiometry (or capacity) of the scavengers were inhibited in the membranes studied. This effect was most evident in Chapter 5 experiments, in which the kinetics of 1,2,4-trichlorobenzene (1,2,4-TCB) sorption to single-walled carbon nanotubes (SWCNTs) were much slower than to powdered activated carbon (PAC) in a poly(vinyl alcohol) PVA film—others have reported that 1,2-dichlorobenzene equilibrates faster with carbon nanotubes (CNTs) than with PAC in free solution (163). Sorption of 2,3',4',5-tetrachlorobiphenyl (2,3',4',5-PCB) to PAC was more effective in a

PVA matrix than in HDPE (Chapter 4), a likely result of the higher driving force for sorption from the hydrophilic PVA environment. Finally, comparing sandwich membrane experiments with  $\text{Fe}^0$  to those using  $\text{Fe}^0$ -containing HDPE membranes described previously (28), we could conclude that the absence of water in HDPE inhibits the reactivity of  $\text{Fe}^0$ . Even scavengers in the sandwich membranes described in Chapter 3, however, were not completely available for reaction with or sorption of the diffusing contaminants—encapsulation of scavengers in a polymer matrix is not the sole reason for the reduced “reactivity” observed. This myriad of factors contributing to inhibited kinetics and reduced scavenger stoichiometry (or capacity) makes it difficult to extend results beyond the contaminant-scavenger-polymer scenarios tested in the laboratory.

Diffusion in the membrane matrix can also influence the effects of the scavenger on membrane breakthrough curves. Slow diffusion improves the effect of the scavenger (as described by the Damköhler number), but may also limit the kinetics of contaminant “reaction” in the membrane itself, as shown in Chapter 4. In some cases, diffusion-limited sorption kinetics may be desirable, as it provides reduced contaminant flux while using less scavenger.

### ***6.3 Framework for Optimization/Prediction of Contaminant Flux***

Hydrophilic active membranes or sandwiched scavenger materials may be used in tandem with HDPE to create a durable barrier in which “reaction” is optimized. One of the objectives of this work was to develop a framework for predicting contaminant flux through layered active barriers. While lag time, flux, and permeability predictions for

single- and multi-layered membranes were used throughout this work to describe experimental breakthrough curves, this topic deserves a bit more attention. The summary below provides some generic predictions (some concrete and some speculative) regarding lag time and pseudo-steady-state flux across composite membranes with an active layer.

To estimate the pseudo-steady-state flux of a layered barrier, we must first estimate the pseudo-steady-state permeability using a sum of resistances relationship:

$$\frac{L_{composite}}{P_{composite}} = \frac{L_A}{P_A} + \frac{L_B}{P_B} + \frac{L_C}{P_C} + \dots \quad (6-1)$$

This requires the assumption that the pseudo-steady-state permeability of each layer can be determined from the appropriate flux expression given in Table 2-1 and Equation 2-5, where  $DH$  becomes the pseudo-steady-state permeability of the layer.

$$j = \frac{DHC_{up}}{L} \quad (2-5)$$

With these assumptions, the “effective” or pseudo-steady-state permeability of any layered barrier is independent of the order in which the layers are placed.

Nuxoll et al. (65) found that reactive scavengers concentrated on the downstream side of a single-layer membrane extended the lag time to a much greater extent than when scavengers were homogeneously dispersed throughout the barrier. The longer lag time was attributed to the ability of the upstream, non-reactive portion of the membrane to provide a slow stream of solute to the reactive layer, as flux through a non-reactive film is inversely proportional to  $L$  (65). Thus, if an active membrane with fast “reaction” is layered with an HDPE geomembrane in a composite contaminant barrier system, we

expect the lag time increase to be more pronounced if the active layer is placed downstream as well. An analytical lag time estimate is not available at this time (unless the permeability of the active layer is similar to that for HDPE). This qualitative conclusion, however, will help guide researchers and design engineers in the future development of composite systems. When an active membrane with pseudo-first-order kinetics is layered with HDPE, it is useful to consider how configuration will affect the rate of “reaction”. When HDPE is placed upstream, the active layer will be exposed to lower contaminant concentrations, reducing the “reaction” rate. The result will be a barrier with a slightly reduced flux that will last for a long period of time. Alternatively, if HDPE is placed downstream, the “reaction” will be faster, resulting in a barrier with a moderately reduced flux that lasts for a shorter period of time.

The above qualitative scenarios may be used to optimize the configuration of a layered barrier system, depending on the type of contamination and the isolation time required of the installation.

#### ***6.4 Opportunities for Future Research***

One benefit to using PAC as a scavenger in active membranes is that it is expected to reduce the flux of a variety of hydrophobic contaminants. Different compounds in hazardous waste landfill leachate, for example, will diffuse across the HDPE component of a (layered) active landfill liner at different rates. Thus, some compounds will reach the PAC particle surfaces faster than others. With time, however, other compounds may diffuse into the active layer and out-compete some compounds for sorption sites on the

PAC, leaving them to continue on their diffusion path toward the downstream surface of the barrier. This type of competitive diffusion/sorption may reduce the effectiveness of the barrier, especially when contaminated material contains some compounds that are more hazardous than others. Diffusion experiments using mixed solutions and/or actual landfill leachate will help define the practical limitations of PAC-containing contaminant barriers.

Reactive and sorptive materials added to geomembranes can improve containment temporarily by intercepting contaminants as they migrate through barriers, as shown in Chapters 3 through 5. Catalysts and enzymes, however, have the potential to improve containment indefinitely. For example, if the reaction is fast (relative to diffusion), the contaminant would theoretically never break through to the membrane's downstream side, because the scavenger would never be "consumed" by the diffusing contaminant. Current research in our department is focused on studying the viability of membrane-bound *Burkholderia xenovorans* strain LB400, an aerobic polychlorinated biphenyl (PCB)-degrading bacterium. Incorporation of other enzymes or bacteria exploited by current bioremediation technology (dehalorespirers for the anaerobic dechlorination of chlorinated organic contaminants, for example) into hydrophilic or sandwich membrane barriers could be coupled with the aerobic barrier to provide dechlorination, aerobic degradation, and containment in one system. Membrane-bound bacteria may benefit from their isolation from competing species and could be used to enhance water and wastewater treatment. These bacteria could be incorporated into porous membranes to

increase the rate of nutrient and substrate delivery to the microorganisms (by increasing *A*). This topic also deserves the attention of the environmental engineering community.

## References

- (1) Aiba, S.; Huang, S.Y. Oxygen permeability and diffusivity in polymer membranes immersed in liquids. *Chemical Engineering Science* **1969**, *24*, 1149-1159.
- (2) Karlsson, G.E.; Gedde, U.W.; Hedenqvist, M.S. Molecular dynamics simulation of oxygen diffusion in dry and water-containing poly(vinyl alcohol). *Polymer* **2004**, *45*, 3893-3900.
- (3) Di Felice, R.; Cazzola, D.; Garbero, M.; Ottonello, P. Unsteady- and steady-state gas permeation through active packaging walls. *Packaging Technology and Science* **2008**, *21*, 185-191.
- (4) Solis, J.A.; Rodgers, B.D. Factors affecting the performance of new oxygen scavenging polymer for packaging applications. *Journal of Plastic Film and Sheeting* **2001**, *17*, 339-349.
- (5) Ferrari, M.C.; Carranza, S.; Bonneze, R.T.; Tung, K.K.; Freeman, B.D.; Paul, D.R. Modeling of oxygen scavenging for improved barrier behavior: Blend films. *Journal of Membrane Science* **2009**, *329*, 183-192.
- (6) Akgün, H. Lined waste containment systems: A method for design and performance evaluation. *Environmental Geology* **1997**, *30*, 209-214.
- (7) U.S. EPA. *Guide for industrial waste management*; EPA 530-R-99-001, Office of Solid Waste and Emergency Response: Washington, DC, 1999.
- (8) Foose, G.J.; Benson, C.H.; Edil, T.B. Comparison of solute transport in three composite liners. *Journal of Geotechnical and Geoenvironmental Engineering* **2002**, *128*, 391-403.
- (9) Edil, T.B. A review of aqueous-phase VOC transport in modern landfill liners. *Waste Management* **2003**, *23*, 561-571.
- (10) Nicot, J.-P.; Gross, B. Self-sealing evaporation ponds for small inland desalination facilities and containment equivalence concepts in Texas. *Desalination and Water Treatment* **2009**, *3*, 29-42.
- (11) Scheirs, J. *A guide to polymeric geomembranes: A practical approach*; John Wiley and Sons Ltd.: West Sussex, U.K., 2009.
- (12) Müller, W.W. *HDPE Geomembranes in geotechnics*; Springer-Verlag: Berlin, Germany, 2007.
- (13) Benson, C.H.; Dwyer, S.F. Material stability and applications. In *Barrier systems for environmental contaminant containment and treatment*; Chien, C. C., Inyang, H. I., Everett, L. G., Eds.; CRC Press: Boca Raton, FL, 2006; pp 143-207.
- (14) Scheutz, C.; Bogner, J.; Chanton, J.P.; Blake, D.; Morcet, M.; Aran, C.; Kjeldsen, P. Atmospheric emissions and attenuation of non-methane organic compounds in cover soils at a French landfill. *Waste Management* **2008**, *28*, 1892-1908.
- (15) Palermo, M.; Maynard, S.; Miller, J.; Reible, D. *Guidance for in-situ subaqueous capping of contaminated sediments*; EPA 905-B96-004, Great Lakes National Program Office, Chicago, IL, 1998.
- (16) Sangam, H.P.; Rowe, R.K. Effects of exposure conditions on the depletion of antioxidants from high-density polyethylene (HDPE) geomembranes. *Canadian Geotechnical Journal* **2002**, *39*, 1221-1230.

- (17) Moo-Young, H.; Johnson, B.; Johnson, A.; Carson, D.; Lew, C.; Liu, S.; Hancock, K. Characterization of infiltration rates from landfills: Supporting groundwater modeling efforts. *Environmental Monitoring and Assessment* **2004**, *96*, 283-311.
- (18) El-Zein, A. A general approach to the modelling of contaminant transport through composite landfill liners with intact or leaking geomembranes. *International Journal for Numerical and Analytical Methods in Geomechanics* **2008**, *32*, 265-287.
- (19) Aboul-Nasr, O.T.; Huang, R.Y.M. Diffusivity and solubility of organic vapors in modified polyethylene films. II. Diffusivity studies. *Journal of Applied Polymer Science* **1979**, *23*, 1833-1849.
- (20) Aminabhavi, T.M.; Naik, H.G. Sorption/desorption, diffusion, permeation and swelling of high density polyethylene geomembrane in the presence of hazardous organic liquids. *Journal of Hazardous Materials* **1999**, *64*, 251-262.
- (21) Park, J.K.; Nibras, M. Mass flux of organic chemicals through polyethylene geomembranes. *Water Environment Research* **1993**, *65*, 227-237.
- (22) Joo, J.C.; Kim, J.Y.; Nam, K. Mass transfer of organic compounds in dilute aqueous solutions into high density polyethylene geomembranes. *Journal of Environmental Engineering* **2004**, *130*, 175-183.
- (23) Chao, K.-P.; Wang, P.; Lin, C.-H. Estimation of diffusion coefficients and solubilities for organic solvents permeation through high-density polyethylene geomembrane. *Journal of Environmental Engineering* **2006**, *132*, 519-526.
- (24) Joo, J.C.; Nam, K.; Kim, J.Y. Estimation of mass transport parameters of organic compounds through high density polyethylene geomembranes using a modified double-compartment apparatus. *Journal of Environmental Engineering* **2005**, *131*, 790-799.
- (25) Park, J.K.; Sakti, J.P.; Hoopes, J.A. Transport of organic compounds in thermoplastic geomembranes. I: Mathematical model. *Journal of Environmental Engineering* **1996**, *122*, 800-806.
- (26) Xiao, S.; Moresoli, C.; Burczyk, A.; Pintauro, P.; De Kee, D. Transport of organic contaminants in geomembranes under stress. *Journal of Environmental Engineering* **1999**, *125*, 647-652.
- (27) Chan Man Fong, C.F.; Moresoli, C.; Xiao, S.; Li, Y.; Bovenkamp, J.; De Kee, D. Modeling diffusion through geomembranes. *Journal of Applied Polymer Science* **1998**, *67*, 1885-1889.
- (28) Shimotori, T.; Cussler, E.L.; Arnold, W.A. High-density polyethylene membrane containing Fe<sup>0</sup> as a contaminant barrier. *Journal of Environmental Engineering* **2006**, *132*, 803-809.
- (29) Rowe, R.K.; Hrapovic, L.; Kosaric, N. Diffusion of chloride and dichloromethane through an HDPE geomembrane. *Geosynthetics International* **1995**, *2*, 507-536.
- (30) Shimotori, T.; Nuxoll, E.E.; Cussler, E.L.; Arnold, W.A. A polymer membrane containing Fe<sup>0</sup> as a contaminant barrier. *Environmental Science and Technology* **2004**, *38*, 2264-2270.

- (31) Nielsen, P.H.; Bjarnadóttir, H.; Winter, P.L.; Christensen, T.H. In situ and laboratory studies on the fate of specific organic compounds in an anaerobic landfill leachate plume, 2. Fate of aromatic and chlorinated aliphatic compounds. *Journal of Contaminant Hydrology* **1995**, *20*, 51-66.
- (32) U.S. EPA. *EPA Superfund record of decision: Velsicol Chemical Corp. (Hardeman County)*; EPA ROD-R04-91-101, Region IV: Atlanta, GA, 1991.
- (33) Assmuth, T.W.; Strandberg, T. Groundwater contamination at Finnish landfills. *Water, Air, and Soil Pollution* **1993**, *69*, 179-199.
- (34) Crank, J. *The mathematics of diffusion*; 2nd ed.; Clarendon Press: Oxford, U.K., 1975.
- (35) Cussler, E.L. *Diffusion: Mass transfer in fluid systems*; 2nd ed.; Cambridge University Press: Cambridge, U.K., 1997.
- (36) Daynes, H.A. The process of diffusion through a rubber membrane. *Proceedings of the Royal Society of London A* **1920**, *97*, 286-307.
- (37) Cussler, E.L.; Hughes, S.E.; Ward III, W.J.; Aris, R. Barrier membranes. *Journal of Membrane Science* **1988**, *38*, 161-174.
- (38) Eitzman, D.M.; Melkote, R.R.; Cussler, E.L. Barrier membranes with tipped impermeable flakes. *AIChE Journal* **1996**, *42*, 2-9.
- (39) Falla, W.R.; Mulski, M.; Cussler, E.L. Estimating diffusion through flake-filled membranes. *Journal of Membrane Science* **1996**, *119*, 129-138.
- (40) Liu, Q.; Cussler, E.L. Barrier membranes made with lithographically printed flakes. *Journal of Membrane Science* **2006**, *285*, 56-67.
- (41) DeRocher, J.P.; Gettelfinger, B.T.; Wang, J.; Nuxoll, E.E.; Cussler, E.L. Barrier membranes with different sizes of aligned flakes. *Journal of Membrane Science* **2005**, *254*, 21-30.
- (42) Goodyer, C.E.; Bunge, A.L. Numerical simulations compared against experimental results for barrier membranes with lithographically printed flakes. *Journal of Membrane Science* **2007**, *306*, 196-208.
- (43) Goodyer, C.E.; Bunge, A.L. Comparison of numerical simulations of barrier membranes with impermeable flakes. *Journal of Membrane Science* **2009**, *329*, 209-218.
- (44) Lape, N.K.; Nuxoll, E.E.; Cussler, E.L. Polydisperse flakes in barrier films. *Journal of Membrane Science* **2004**, *236*, 29-37.
- (45) Yang, C.; Smyrl, W.H.; Cussler, E.L. Flake alignment in composite coatings. *Journal of Membrane Science* **2004**, *231*, 1-12.
- (46) Lape, N.K.; Yang, C.; Cussler, E.L. Flake-filled reactive membranes. *Journal of Membrane Science* **2002**, *209*, 271-282.
- (47) Yang, C.; Nuxoll, E.E.; Cussler, E.L. Reactive barrier films. *AIChE Journal* **2001**, *47*, 295-302.
- (48) Shimotori, T.; Cussler, E.L.; Arnold, W.A. Diffusion of mobile products in reactive barrier membranes. *Journal of Membrane Science* **2007**, *291*, 111-119.
- (49) Petropoulos, J.H. Quantitative analysis of gaseous diffusion in glassy polymers. *Journal of Polymer Science Part A-2: Polymer Physics* **1970**, *8*, 1797-1801.

- (50) Kemp, D.R.; Paul, D.R. Gas sorption in polymer membranes containing adsorptive fillers. *Journal of Polymer Science: Polymer Physics Edition* **1974**, *12*, 485-500.
- (51) Paul, D.R. Effect of immobilizing adsorption on the diffusion time lag. *Journal of Polymer Science Part A-2: Polymer Physics* **1969**, *7*, 1811-1818.
- (52) Paul, D.R.; Kemp, D.R. The diffusion time lag in polymer membranes containing adsorptive fillers. *Journal of Polymer Science: Polymer Symposia* **1973**, *41*, 79-93.
- (53) Paul, D.R.; Koros, W.J. Effect of partially immobilizing sorption on permeability and the diffusion time lag. *Journal of Polymer Science: Polymer Physics Edition* **1976**, *14*, 675-685.
- (54) Warta, A.M.; Arnold, W.A.; Cussler, E.L. Permeable membranes containing crystalline silicotitanate as model barriers for cesium ion. *Environmental Science and Technology* **2005**, *39*, 9738-9743.
- (55) Nuxoll, E.E.; Cussler, E.L. The third parameter in reactive barrier films. *AIChE Journal* **2005**, *51*, 456-463.
- (56) Siegel, R.A.; Cussler, E.L. Reactive barrier membranes: Some theoretical observations regarding the time lag and breakthrough curves. *Journal of Membrane Science* **2004**, *229*, 33-41.
- (57) Siegel, R.A. Characterization of relaxation to steady state in membranes with binding and reaction. *Journal of Membrane Science* **2005**, *251*, 91-99.
- (58) Solovyov, S.E.; Goldman, A.Y. Optimized design of multilayer barrier films incorporating a reactive layer. I. Methodology of ingress analysis. *Journal of Applied Polymer Science* **2006**, *100*, 1940-1951.
- (59) Solovyov, S.E. Determining the rate constant of diffusion-controlled oxygen scavenging reaction in polymer membranes by transient permeability measurements. *The Journal of Physical Chemistry B* **2004**, *108*, 15618-15630.
- (60) Solovyov, S.E. Reactivity of gas barrier membranes filled with reactive particulates. *The Journal of Physical Chemistry B* **2006**, *110*, 17977-17986.
- (61) Saito, R.; Nakagawa, D. Synthesis of water vapor barrier membrane by coating of poly(vinyl alcohol) substrate with poly(*tert*-butyl acrylate)-silica nanocomposite. *Polymers for Advanced Technologies* **2009**, *20*, 285-290.
- (62) Barrie, J.A.; Levine, J.D.; Michaels, A.S.; Wong, P. Diffusion and solution of gases in composite rubber membranes. *Transactions of the Faraday Society* **1963**, *59*, 869-878.
- (63) Siegel, R.A. Algebraic, differential, and integral relations for membranes in series and other multilaminar media: Permeabilities, solute consumption, lag times, and mean first passage times. *The Journal of Physical Chemistry* **1991**, *95*, 2556-2565.
- (64) Mayer, P.; Fernqvist, M.M.; Christensen, P.S.; Karlson, U.; Trapp, S. Enhanced diffusion of polycyclic aromatic hydrocarbons in artificial and natural aqueous solutions. *Environmental Science and Technology* **2007**, *41*, 6148-6155.
- (65) Nuxoll, E.E.; Siegel, R.A.; Cussler, E.L. Layered reactive barrier films. *Journal of Membrane Science* **2005**, *252*, 29-36.
- (66) Solovyov, S.E.; Goldman, A.Y. Optimized design of multilayer barrier films incorporating a reactive layer. II. Solute dynamics in two-layer films. *Journal of Applied Polymer Science* **2006**, *100*, 1952-1965.

- (67) Solovyov, S.E.; Goldman, A.Y. Optimized design of multilayer barrier films incorporating a reactive layer. III. Case analysis and generalized multilayer solutions. *Journal of Applied Polymer Science* **2006**, *100*, 1966-1977.
- (68) Huckins, J.N.; Tubergen, M.W.; Manuweera, G.K. Semipermeable membrane devices containing model lipid: A new approach to monitoring the bioavailability of lipophilic contaminants and estimating their bioconcentration potential. *Chemosphere* **1990**, *20*, 533-552.
- (69) Huckins, J.N.; Manuweera, G.K.; Petty, J.D.; Mackay, D.; Lebo, J.A. Lipid-containing semipermeable membrane devices for monitoring organic contaminants in water. *Environmental Science and Technology* **1993**, *27*, 2489-2496.
- (70) Gale, R.W. Three-compartment model for contaminant accumulation by semipermeable membrane devices. *Environmental Science and Technology* **1998**, *32*, 2292-2300.
- (71) Luellen, D.R.; Shea, D. Calibration and field verification of semipermeable membrane devices for measuring polycyclic aromatic hydrocarbons in water. *Environmental Science and Technology* **2002**, *36*, 1791-1797.
- (72) Prest, H.F.; Jarman, W.M.; Burns, S.A.; Weismüller, T.; Martin, M.; Huckins, J.N. Passive water sampling via semipermeable membrane devices (SPMDs) in concert with bivalves in the Sacramento/San Joaquin River delta. *Chemosphere* **1992**, *25*, 1811-1823.
- (73) Booij, K.; Hoedemaker, J.R.; Bakker, J.F. Dissolved PCBs, PAHs, and HCB in pore waters and overlying waters of contaminated harbor sediments. *Environmental Science and Technology* **2003**, *37*, 4213-4220.
- (74) Luellen, D.R.; Shea, D. Semipermeable membrane devices accumulate conserved ratios of sterane and hopane petroleum biomarkers. *Chemosphere* **2003**, *53*, 705-713.
- (75) Carls, M.G.; Holland, L.G.; Short, J.W.; Heintz, R.A.; Rice, S.D. Monitoring polynuclear aromatic hydrocarbons in aqueous environments with passive low-density polyethylene membrane devices. *Environmental Toxicology and Chemistry* **2004**, *23*, 1416-1424.
- (76) Adams, R.G.; Lohmann, R.; Fernandez, L.A.; MacFarlane, J.K.; Gschwend, P.M. Polyethylene devices: Passive samplers for measuring dissolved hydrophobic organic compounds in aquatic environments. *Environmental Science and Technology* **2007**, *41*, 1317-1323.
- (77) Tomaszewski, J.E.; Luthy, R.G. Field deployment of polyethylene devices to measure PCB concentrations in pore water of contaminated sediment. *Environmental Science and Technology* **2008**, *42*, 6086-6091.
- (78) Dole, P.; Feigenbaum, A.E.; de la Cruz, C.; Pastorelli, S.; Paseiro, P.; Hankemeier, T.; Voulzatis, Y.; Aucejo, S.; Saillard, P.; Papaspyrides, C. Typical diffusion behaviour in packaging polymers - Application to functional barriers. *Food Additives and Contaminants* **2006**, *23*, 202-211.

- (79) Pascall, M.A.; Zabik, M.E.; Zabik, M.J.; Hernandez, R.J. Development of an analytical method for the determination of congener specific PCBs in selected polymeric packaging materials. *Bulletin of Environmental Contamination and Toxicology* **1998**, *61*, 8-14.
- (80) Pascall, M.A.; Zabik, M.E.; Zabik, M.J.; Hernandez, R.J. Uptake of polychlorinated biphenyls (PCBs) from an aqueous medium by polyethylene, polyvinyl chloride, and polystyrene films. *Journal of Agricultural and Food Chemistry* **2005**, *53*, 164-169.
- (81) Voultzatis, I.S.; Papaspyrides, C.D.; Tsenoglou, C.J.; Roussis, C. Diffusion of model contaminants in high-density polyethylene. *Macromolecular Materials and Engineering* **2007**, *292*, 272-284.
- (82) Xu, J.; Bhattacharyya, D. Membrane-based bimetallic nanoparticles for environmental remediation: Synthesis and reactive properties. *Environmental Progress* **2005**, *24*, 358-366.
- (83) Xu, J.; Bhattacharyya, D. Fe/Pd nanoparticle immobilization in microfiltration membrane pores: Synthesis, characterization, and application in the dechlorination of polychlorinated biphenyls. *Industrial and Engineering Chemistry Research* **2007**, *46*, 2348-2359.
- (84) Xu, J.; Dozier, A.; Bhattacharyya, D. Synthesis of nanoscale bimetallic particles in polyelectrolyte membrane matrix for reductive transformation of halogenated organic compounds. *Journal of Nanoparticle Research* **2005**, *7*, 449-467.
- (85) Meyer, D.E.; Bhattacharyya, D. Impact of membrane immobilization on particle formation and trichloroethylene dechlorination for bimetallic Fe/Ni nanoparticles in cellulose acetate membranes. *The Journal of Physical Chemistry B* **2007**, *111*, 7142-7154.
- (86) Wu, L.; Shamsuzzoha, M.; Ritchie, S.M.C. Preparation of cellulose acetate supported zero-valent iron nanoparticles for the dechlorination of trichloroethylene in water. *Journal of Nanoparticle Research* **2005**, *7*, 469-476.
- (87) Akay, G.; Erhan, E.; Keskinler, B.; Algur, O.F. Removal of phenol from wastewater using membrane-immobilized enzymes Part II. Cross-flow filtration. *Journal of Membrane Science* **2002**, *206*, 61-68.
- (88) Degiorgi, C.F.; Pizarro, R.A.; Smolko, E.E.; Lora, S.; Carena, M. Hydrogels for immobilization of bacteria used in the treatment of metal-contaminated wastes. *Radiation Physics and Chemistry* **2002**, *63*, 109-113.
- (89) Lyngberg, O.K.; Stemke, D.J.; Schottel, J.L.; Flickinger, M.C. A single-use luciferase-based mercury biosensor using *Escherichia coli* HB101 immobilized in a latex copolymer film. *Journal of Industrial Microbiology and Biotechnology* **1999**, *23*, 668-676.
- (90) Moutaouakkil, A.; Zeroual, Y.; Dzayri, F.Z.; Talbi, M.; Lee, K.; Blaghen, M. Decolorization of azo dyes with *Enterobacter agglomerans* immobilized in different supports by using fluidized bed bioreactor. *Current Microbiology* **2004**, *48*, 124-129.

- (91) Kim, J.Y.; Edil, T.B.; Park, J.K. Volatile organic compound (VOC) transport through compacted clay. *Journal of Geotechnical and Geoenvironmental Engineering* **2001**, *127*, 126-134.
- (92) Johnson, R.L.; Cherry, J.A.; Pankow, J.F. Diffusive contaminant transport in natural clay: A field example and implications for clay-lined waste disposal sites. *Environmental Science and Technology* **1989**, *23*, 340-349.
- (93) Christensen, T.H.; Kjeldsen, P.; Bjerg, P.L.; Jensen, D.L.; Christensen, J.B.; Baun, A.; Albrechtsen, H.-J.; Heron, G. Biogeochemistry of landfill leachate plumes. *Applied Geochemistry* **2001**, *16*, 659-718.
- (94) U.S. EPA. *National recommended water quality criteria table*; EPA-822-R-02-047, Office of Science and Technology: Washington, DC, 2002.
- (95) Baun, A.; Jensen, S.D.; Bjerg, P.L.; Christensen, T.H.; Nyholm, N. Toxicity of organic chemical pollution in groundwater downgradient of a landfill (Grindsted, Denmark). *Environmental Science and Technology* **2000**, *34*, 1647-1652.
- (96) Matheson, L.J.; Tratnyek, P.G. Reductive dehalogenation of chlorinated methanes by iron metal. *Environmental Science and Technology* **1994**, *28*, 2045-2053.
- (97) Gillham, R.W.; O'Hannesin, S.F. Enhanced degradation of halogenated aliphatics by zero-valent iron. *Ground Water* **1994**, *32*, 958-967.
- (98) Roberts, A.L.; Totten, L.A.; Arnold, W.A.; Burris, D.R.; Campbell, T.J. Reductive elimination of chlorinated ethylenes by zero-valent metals. *Environmental Science and Technology* **1996**, *30*, 2654-2659.
- (99) O'Hannesin, S.F.; Gillham, R.W. Long-term performance of an in situ "iron wall" for remediation of VOCs. *Ground Water* **1998**, *36*, 164-170.
- (100) Lien, H.-L.; Zhang, W.-X. Transformation of chlorinated methanes by nanoscale iron particles. *Journal of Environmental Engineering* **1999**, *125*, 1042-1047.
- (101) Arnold, W.A.; Roberts, A.L. Pathways and kinetics of chlorinated ethylene and chlorinated acetylene reaction with Fe(0) particles. *Environmental Science and Technology* **2000**, *34*, 1794-1805.
- (102) Liu, Y.; Choi, H.; Dionysiou, D.; Lowry, G.V. Trichloroethene hydrodechlorination in water by highly disordered monometallic nanoiron. *Chemistry of Materials* **2005**, *17*, 5315-5322.
- (103) Liu, Y.; Majetich, S.A.; Tilton, R.D.; Sholl, D.S.; Lowry, G.V. TCE dechlorination rates, pathways, and efficiency of nanoscale iron particles with different properties. *Environmental Science and Technology* **2005**, *39*, 1338-1345.
- (104) Liu, Y.; Lowry, G.V. Effect of particle age (Fe<sup>0</sup> content) and solution pH on NZVI reactivity: H<sub>2</sub> evolution and TCE dechlorination. *Environmental Science and Technology* **2006**, *40*, 6085-6090.
- (105) Li, X.-q.; Elliott, D.W.; Zhang, W.-x. Zero-valent iron nanoparticles for abatement of environmental pollutants: Materials and engineering aspects. *Critical Reviews in Solid State and Materials Science* **2006**, *31*, 111-122.

- (106) Nurmi, J.T.; Tratnyek, P.G.; Sarathy, V.; Baer, D.R.; Amonette, J.E.; Pecher, K.; Wang, C.; Linehan, J.C.; Matson, D.W.; Penn, R.L.; Driessen, M.D. Characterization and properties of metallic iron nanoparticles: Spectroscopy, electrochemistry, and kinetics. *Environmental Science and Technology* **2005**, *39*, 1221-1230.
- (107) Sun, Y.-P.; Li, X.-q.; Cao, J.; Zhang, W.-x.; Wang, H.P. Characterization of zero-valent iron nanoparticles. *Advances in Colloid and Interface Science* **2006**, *120*, 47-56.
- (108) Cao, J.; Elliot, D.; Zhang, W.-x. Perchlorate reduction by nanoscale iron particles. *Journal of Nanoparticle Research* **2005**, *7*, 499-506.
- (109) Xiong, Z.; Zhao, D.; Pan, G. Rapid and complete destruction of perchlorate in water and ion-exchange brine using stabilized zero-valent iron nanoparticles. *Water Research* **2007**, *41*, 3497-3505.
- (110) Yang, G.C.C.; Lee, H.-L. Chemical reduction of nitrate by nanosized iron: Kinetics and pathways. *Water Research* **2005**, *39*, 884-894.
- (111) Li, X.-q.; Brown, D.G.; Zhang, W.-x. Stabilization of biosolids with nanoscale zero-valent iron (nZVI). *Journal of Nanoparticle Research* **2007**, *9*, 233-243.
- (112) Bartelt-Hunt, S.L.; Smith, J.A.; Burns, S.E.; Rabideau, A.J. Evaluation of granular activated carbon, shale, and two organoclays for use as sorptive amendments in clay landfill liners. *Journal of Geotechnical and Geoenvironmental Engineering* **2005**, *131*, 848-856.
- (113) Shackelford, C.D.; Sale, T.C.; Liberati, M.R. In *Proceedings of Geo-Frontiers: Austin, Texas, 2005*.
- (114) Gotpagar, J.; Lyuksyutov, S.; Cohn, R.; Grulke, E.; Bhattacharyya, D. Reductive dehalogenation of trichloroethylene with zero-valent iron: Surface profiling microscopy and rate enhancement studies. *Langmuir* **1999**, *15*, 8412-8420.
- (115) Farrell, J.; Kason, M.; Melitas, N.; Li, T. Investigation of the long-term performance of zero-valent iron for reductive dechlorination of trichloroethylene. *Environmental Science and Technology* **2000**, *34*, 514-521.
- (116) Helland, B.R.; Alvarez, P.J.J.; Schnoor, J.L. Reductive dechlorination of carbon tetrachloride with elemental iron. *Journal of Hazardous Materials* **1995**, *41*, 205-216.
- (117) Wang, C.-B.; Zhang, W.-x. Synthesizing nanoscale iron particles for rapid and complete dechlorination of TCE and PCBs. *Environmental Science and Technology* **1997**, *31*, 2154-2156.
- (118) Kleineidam, S.; Schüth, C.; Grathwohl, P. Solubility-normalized combined adsorption-partitioning sorption isotherms for organic pollutants. *Environmental Science and Technology* **2002**, *36*, 4689-4697.
- (119) Helm, P.A.; Gewurtz, S.B.; Whittle, D.M.; Marvin, C.H.; Fisk, A.T.; Tomy, G.T. Occurrence and biomagnification of polychlorinated naphthalenes and non- and mono-*ortho* PCBs in Lake Ontario sediment and biota. *Environmental Science and Technology* **2008**, *42*, 1024-1031.

- (120) McLeod, P.B.; van den Heuvel-Greve, M.J.; Luoma, S.N.; Luthy, R.G. Biological uptake of polychlorinated biphenyls by *Macoma balthica* from sediment amended with activated carbon. *Environmental Toxicology and Chemistry* **2007**, *26*, 980-987.
- (121) Lake, J.L.; Rubinstein, N.I.; Lee II, H.; Lake, C.A.; Heltshe, J.; Pavignano, S. Equilibrium partitioning and bioaccumulation of sediment-associated contaminants by infaunal organisms. *Environmental Toxicology and Chemistry* **1990**, *9*, 1095-1106.
- (122) King, T.L.; Lee, K.; Yeats, P.; Alexander, R. Chlorobenzenes in snow crab (*Chionoectes opilio*): Time-series monitoring following an accidental release. *Bulletin of Environmental Contamination and Toxicology* **2003**, *71*, 543-550.
- (123) Zeng, E.Y.; Bay, S.M.; Greenstein, D.; Vista, C.; Yu, C.; Ritter, K. Toxic effects of polychlorinated biphenyl bioaccumulation in sea urchins exposed to contaminated sediments. *Environmental Toxicology and Chemistry* **2003**, *22*, 1065-1074.
- (124) Walters, D.M.; Fritz, K.M.; Johnson, B.R.; Lazorchak, J.M.; McCormick, F.H. Influence of trophic position and spatial location on polychlorinated biphenyl (PCB) bioaccumulation in a stream food web. *Environmental Science and Technology* **2008**, *42*, 2316-2322.
- (125) Ashizawa, A.E.; Hicks, H.E.; De Rosa, C.T. Human health research and policy development: Experience in the Great Lakes region. *International Journal of Hygiene and Environmental Health* **2005**, *208*, 7-13.
- (126) U.S. EPA. *Survey of new findings in scientific literature related to atmospheric deposition to the Great Waters: Polychlorinated biphenyls (PCB)*; EPA 452-R-07-012, Office of Air Quality Planning and Standards: Research Triangle Park, NC, 2007.
- (127) Aoki, Y. Polychlorinated biphenyls, polychlorinated dibenzo-*p*-dioxins, and polychlorinated dibenzofurans as endocrine disrupters—What we have learned from Yusho disease. *Environmental Research* **2001**, *86*, 2-11.
- (128) deCastro, B.R.; Korrick, S.A.; Spengler, J.D.; Soto, A.M. Estrogenic activity of polychlorinated biphenyls present in human tissue and the environment. *Environmental Science and Technology* **2006**, *40*, 2819-2825.
- (129) Agarwal, S.; Al-Abed, S.R.; Dionysiou, D.D. In situ technologies for reclamation of PCB-contaminated sediments: Current challenges and research thrust areas. *Journal of Environmental Engineering* **2007**, *133*, 1075-1078.
- (130) U.S. EPA. *Guidance on remedial actions for Superfund sites with PCB contamination*; EPA 540-G-90-007, Office of Emergency and Remedial Response: Washington, DC, 1990.
- (131) U.S. EPA. *Contaminated sediment remediation guidance for hazardous waste sites*; EPA 540-R-05-012, Office of Solid Waste and Emergency Response: Washington, DC, 2005.
- (132) Schneider, A.R.; Porter, E.T.; Baker, J.E. Polychlorinated biphenyl release from resuspended Hudson River sediment. *Environmental Science and Technology* **2007**, *41*, 1097-1103.

- (133) Sanchez, F.F.; Thibodeaux, L.J.; Valsaraj, K.T.; Reible, D.D. Multimedia chemical fate model for environmental dredging. *Practice Periodical of Hazardous, Toxic, and Radioactive Waste Management* **2002**, *6*, 120-128.
- (134) Voie, Ø.A.; Johnsen, A.; Rosslund, H.K. Why biota still accumulate high levels of PCB after removal of PCB contaminated sediments in a Norwegian fjord. *Chemosphere* **2002**, *46*, 1367-1372.
- (135) Thoma, G.J.; Reible, D.D.; Valsaraj, K.T.; Thibodeaux, L.J. Efficiency of capping contaminated sediments in situ. 2. Mathematics of diffusion-adsorption in the capping layer. *Environmental Science and Technology* **1993**, *27*, 2412-2419.
- (136) Murphy, P.; Marquette, A.; Reible, D.; Lowry, G.V. Predicting the performance of activated carbon-, coke-, and soil-amended thin layer sediment caps. *Journal of Environmental Engineering* **2006**, *132*, 787-794.
- (137) Palermo, M.R. Design considerations for in-situ capping of contaminated sediments. *Water Science and Technology* **1998**, *37*, 315-321.
- (138) Alshawabkeh, A.N.; Rahbar, N.; Sheahan, T. A model for contaminant mass flux in capped sediment under consolidation. *Journal of Contaminant Hydrology* **2005**, *78*, 147-165.
- (139) Eek, E.; Cornelissen, G.; Kibsgaard, A.; Breedveld, G.D. Diffusion of PAH and PCB from contaminated sediments with and without mineral capping; measurement and modelling. *Chemosphere* **2008**, *71*, 1629-1638.
- (140) Tarabara, V.V.; Wiesner, M.R. Physical and transport properties of bentonite-cement composites: A new material for in situ capping of contaminated underwater sediments. *Environmental Engineering Science* **2005**, *22*, 578-590.
- (141) Werner, D.; Ghosh, U.; Luthy, R.G. Modeling polychlorinated biphenyl mass transfer after amendment of contaminated sediment with activated carbon. *Environmental Science and Technology* **2006**, *40*, 4211-4218.
- (142) Cho, Y.-M.; Ghosh, U.; Kennedy, A.J.; Grossman, A.; Ray, G.; Tomaszewski, J.E.; Smithenry, D.W.; Bridges, T.S.; Luthy, R.G. Field application of activated carbon amendment for in-situ stabilization of polychlorinated biphenyls in marine sediment. *Environmental Science and Technology* **2009**, *43*, 3815-3823.
- (143) Millward, R.N.; Bridges, T.S.; Ghosh, U.; Zimmerman, J.R.; Luthy, R.G. Addition of activated carbon to sediments to reduce PCB bioaccumulation by a polychaete (*Neanthes arenaceodentata*) and an amphipod (*Leptocheirus plumulosus*). *Environmental Science and Technology* **2005**, *39*, 2880-2887.
- (144) Zimmerman, J.R.; Ghosh, U.; Millward, R.N.; Bridges, T.S.; Luthy, R.G. Addition of carbon sorbents to reduce PCB and PAH bioavailability in marine sediments: Physicochemical tests. *Environmental Science and Technology* **2004**, *38*, 5458-5464.
- (145) Zimmerman, J.R.; Werner, D.; Ghosh, U.; Millward, R.N.; Bridges, T.S.; Luthy, R.G. Effects of dose and particle size on activated carbon treatment to sequester polychlorinated biphenyls and polycyclic aromatic hydrocarbons in marine sediments. *Environmental Toxicology and Chemistry* **2005**, *24*, 1594-1601.

- (146) Zimmerman, J.R.; Bricker, J.D.; Jones, C.; Dacunto, P.J.; Street, R.L.; Luthy, R.G. The stability of marine sediments at a tidal basin in San Francisco Bay amended with activated carbon for sequestration of organic contaminants. *Water Research* **2008**, *42*, 4133-4145.
- (147) McDonough, K.M.; Murphy, P.; Olsa, J.; Zhu, Y.; Reible, D.; Lowry, G.V. Development and placement of a sorbent-amended thin layer sediment cap in the Anacostia River. *Soil and Sediment Contamination* **2007**, *16*, 313-322.
- (148) Lowry, G.V.; Murphy, P.J.; Marquette, A.; Reible, D. Sorbent-amended "active" sediment caps for in-place management of PCB-contaminated sediments. *Contaminated Soils* **2006**, *10*, 379-391.
- (149) Choi, H.; Agarwal, S.; Al-Abed, S.R. Adsorption and simultaneous dechlorination of PCBs on GAC/Fe/Pd: Mechanistic aspects and reactive capping barrier concept. *Environmental Science and Technology* **2009**, *43*, 488-493.
- (150) Meares, P. The solubilities of gases in polyvinyl acetate. *Transactions of the Faraday Society* **1958**, *54*, 40-46.
- (151) McGroddy, S.E.; Farrington, J.W.; Gschwend, P.M. Comparison of the *in situ* and desorption sediment-water partitioning of polycyclic aromatic hydrocarbons and polychlorinated biphenyls. *Environmental Science and Technology* **1996**, *30*, 172-177.
- (152) Di Toro, D.M.; Horzempa, L.M. Reversible and resistant components of PCB adsorption-desorption: Isotherms. *Environmental Science and Technology* **1982**, *16*, 594-602.
- (153) Gong, Y.; Depinto, J.V.; Rhee, G.-Y.; Xia, L. Desorption rates of two PCB congeners from suspended sediments—I. Experimental results. *Water Research* **1998**, *32*, 2507-2517.
- (154) Carroll, K.M.; Harkness, M.R.; Bracco, A.A.; Balcarcel, R.R. Application of a permeant/polymer diffusional model to the desorption of polychlorinated biphenyls from Hudson River sediments. *Environmental Science and Technology* **1994**, *28*, 253-258.
- (155) ten Hulscher, Th.E.M.; Vrind, B.A.; van Noort, P.C.M.; Govers, H.A.J. Resistant sorption of *in situ* chlorobenzenes and a polychlorinated biphenyl in river Rhine suspended matter. *Chemosphere* **2002**, *49*, 1231-1238.
- (156) McDonough, K.M.; Fairey, J.L.; Lowry, G.V. Adsorption of polychlorinated biphenyls to activated carbon: Equilibrium isotherms and a preliminary assessment of the effect of dissolved organic matter and biofilm loadings. *Water Research* **2008**, *42*, 575-584.
- (157) Wiesner, M.R.; Lowry, G.V.; Alvarez, P.; Dionysiou, D.; Biswas, P. Assessing the risks of manufactured nanomaterials. *Environmental Science and Technology* **2006**, *40*, 4336-4345.
- (158) Lam, C.-w.; James, J.T.; McCluskey, R.; Arepalli, S.; Hunter, R.L. A review of carbon nanotube toxicity and assessment of potential occupational and environmental health risks. *Critical Reviews in Toxicology* **2006**, *36*, 189-217.

- (159) Petersen, E.J.; Pinto, R.A.; Landrum, P.F.; Weber Jr., W.J. Influence of carbon nanotubes on pyrene bioaccumulation from contaminated soils by earthworms. *Environmental Science and Technology* **2009**, *43*, 4181-4187.
- (160) Mauter, M.S.; Elimelech, M. Environmental applications of carbon-based nanomaterials. *Environmental Science and Technology* **2008**, *42*, 5843-5859.
- (161) Andreescu, S.; Njagi, J.; Ispas, C.; Ravalli, M.T. JEM spotlight: Applications of advanced nanomaterials for environmental monitoring. *Journal of Environmental Monitoring* **2009**, *11*, 27-40.
- (162) Long, R.Q.; Yang, R.T. Carbon nanotubes as superior sorbent for dioxin removal. *Journal of the American Chemical Society* **2001**, *123*, 2058-2059.
- (163) Peng, X.; Li, Y.; Luan, Z.; Di, Z.; Wang, H.; Tian, B.; Jia, Z. Adsorption of 1,2-dichlorobenzene from water to carbon nanotubes. *Chemical Physics Letters* **2003**, *376*, 154-158.
- (164) Yan, H.; Gong, A.; He, H.; Zhou, J.; Wei, Y.; Lv, L. Adsorption of microcystins by carbon nanotubes. *Chemosphere* **2006**, *62*, 142-148.
- (165) Yang, K.; Zhu, L.; Xing, B. Adsorption of polycyclic aromatic hydrocarbons by carbon nanomaterials. *Environmental Science and Technology* **2006**, *40*, 1855-1861.
- (166) Yang, K.; Wang, X.; Zhu, L.; Xing, B. Competitive sorption of pyrene, phenanthrene, and naphthalene on multiwalled carbon nanotubes. *Environmental Science and Technology* **2006**, *40*, 5804-5810.
- (167) Chin, C.-J.M.; Shih, L.-C.; Tsai, H.-J.; Liu, T.-K. Adsorption of *o*-xylene and *p*-xylene from water by SWCNTs. *Carbon* **2007**, *45*, 1254-1260.
- (168) Lu, C.; Chung, Y.-L.; Chang, K.-F. Adsorption of trihalomethanes from water with carbon nanotubes. *Water Research* **2005**, *39*, 1183-1189.
- (169) Chen, W.; Duan, L.; Zhu, D. Adsorption of polar and nonpolar organic chemicals to carbon nanotubes. *Environmental Science and Technology* **2007**, *41*, 8295-8300.
- (170) Lin, D.; Xing, B. Adsorption of phenolic compounds by carbon nanotubes: Role of aromaticity and substitution of hydroxyl groups. *Environmental Science and Technology* **2008**, *42*, 7254-7259.
- (171) Pan, B.; Xing, B. Adsorption mechanisms of organic chemicals on carbon nanotubes. *Environmental Science and Technology* **2008**, *42*, 9005-9013.
- (172) Shen, X.-E.; Shan, X.-Q.; Dong, D.-M.; Hua, X.-Y.; Owens, G. Kinetics and thermodynamics of sorption of nitroaromatic compounds to as-grown and oxidized multiwalled carbon nanotubes. *Journal of Colloid and Interface Science* **2009**, *330*, 1-8.
- (173) Wang, X.; Tao, S.; Xing, B. Sorption and competition of aromatic compounds and humic acid on multiwalled carbon nanotubes. *Environmental Science and Technology* **2009**, *43*, 6214-6219.
- (174) El-Sheikh, A.H.; Sweileh, J.A.; Al-Degs, Y.S.; Insisi, A.A.; Al-Rabady, N. Critical evaluation and comparison of enrichment efficiency of multi-walled carbon nanotubes, C18 silica and activated carbon towards some pesticides from environmental waters. *Talanta* **2008**, *74*, 1675-1680.

- (175) Asensio-Ramos, M.; Hernández-Borges, J.; Borges-Miquel, T.M.; Rodríguez-Delgado, M.A. Evaluation of multi-walled carbon nanotubes as solid-phase extraction adsorbents of pesticides from agricultural, ornamental and forestal soils. *Analytica Chimica Acta* **2009**, *647*, 167-176.
- (176) Liu, G.; Wang, J.; Zhu, Y.; Zhang, X. Application of multiwalled carbon nanotubes as a solid-phase extraction sorbent for chlorobenzenes. *Analytical Letters* **2004**, *37*, 3085-3104.
- (177) Chen, G.-C.; Shan, X.-Q.; Wang, Y.-S.; Wen, B.; Pei, Z.-G.; Xie, Y.-N.; Liu, T.; Pignatello, J.J. Adsorption of 2,4,6-trichlorophenol by multi-walled carbon nanotubes as affected by Cu(II). *Water Research* **2009**, *43*, 2409-2418.
- (178) Treacy, M.M.J.; Ebbesen, T.W.; Gibson, J.M. Exceptionally high Young's modulus observed for individual carbon nanotubes. *Nature* **1996**, *381*, 678-680.
- (179) Dalton, A.B.; Collins, S.; Muñoz, E.; Razal, J.M.; Ebron, V.H.; Ferraris, J.P.; Coleman, J.N.; Kim, B.G.; Baughman, R.H. Super-tough carbon-nanotube fibres. *Nature* **2003**, *423*, 703.
- (180) Dalton, A.B.; Collins, S.; Razal, J.; Muñoz, E.; Ebron, V.H.; Kim, B.G.; Coleman, J.N.; Ferraris, J.P.; Baughman, R.H. Continuous carbon nanotube composite fibers: Properties, potential applications, and problems. *Journal of Materials Chemistry* **2004**, *14*, 1-3.
- (181) Shaffer, M.S.P.; Windle, A.H. Fabrication and characterization of carbon nanotube/poly(vinyl alcohol) composites. *Advanced Materials* **1999**, *11*, 937-941.
- (182) Ciambelli, P.; Sarno, M.; Gorrasi, G.; Sannino, D.; Tortora, M.; Vittoria, V. Preparation and physical properties of carbon nanotubes-PVA nanocomposites. *Journal of Macromolecular Science, Part B: Physics* **2005**, *44*, 779-795.
- (183) Ni, W.; Wang, B.; Wang, H.; Zhang, Y. Fabrication and properties of carbon nanotube and poly(vinyl alcohol) composites. *Journal of Macromolecular Science, Part B: Physics* **2006**, *45*, 659-664.
- (184) Ryan, K.P.; Cadek, M.; Nicolosi, V.; Blond, D.; Ruether, M.; Armstrong, G.; Swan, H.; Fonseca, A.; Nagy, J.B.; Maser, W.K.; Blau, W.J.; Coleman, J.N. Carbon nanotubes for reinforcement of plastics? A case study with poly(vinyl alcohol). *Composites Science and Technology* **2007**, *67*, 1640-1649.
- (185) Coleman, J.N.; Cadek, M.; Ryan, K.P.; Fonseca, A.; Nagy, J.B.; Blau, W.J.; Ferreira, M.S. Reinforcement of polymers with carbon nanotubes. The role of an ordered polymer interfacial region. Experiment and modeling. *Polymer* **2006**, *47*, 8556-8561.
- (186) Probst, O.; Moore, E.M.; Resasco, D.E.; Grady, B.P. Nucleation of polyvinyl alcohol crystallization by single-walled carbon nanotubes. *Polymer* **2004**, *45*, 4437-4443.
- (187) Langley, L.A.; Fairbrother, D.H. Effect of wet chemical treatments on the distribution of surface oxides on carbonaceous materials. *Carbon* **2007**, *45*, 47-54.
- (188) Cho, H.-H.; Smith, B.A.; Wnuk, J.D.; Fairbrother, D.H.; Ball, W.P. Influence of surface oxides on the adsorption of naphthalene onto multiwalled carbon nanotubes. *Environmental Science and Technology* **2008**, *42*, 2899-2905.

- (189) Chen, G.-C.; Shan, X.-Q.; Wang, Y.-S.; Pei, Z.-G.; Shen, X.-E.; Wen, B.; Owens, G. Effects of copper, lead, and cadmium on the sorption and desorption of atrazine onto and from carbon nanotubes. *Environmental Science and Technology* **2008**, *42*, 8297-8302.
- (190) Karanfil, T.; Kilduff, J.E. Role of granular activated carbon surface chemistry on the adsorption of organic compounds. 1. Priority pollutants. *Environmental Science and Technology* **1999**, *33*, 3217-3224.
- (191) Salame, I.I.; Bandosz, T.J. Role of surface chemistry in adsorption of phenol on activated carbons. *Journal of Colloid and Interface Science* **2003**, *264*, 307-312.
- (192) Andrade-Espinosa, G.; Muñoz-Sandoval, E.; Terrones, M.; Endo, M.; Terrones, H.; Rangel-Mendez, J.R. Acid modified bamboo-type carbon nanotubes and cup-stacked-type carbon nanofibres as adsorbent materials: Cadmium removal from aqueous solution. *Journal of Chemical Technology and Biotechnology* **2009**, *84*, 519-524.
- (193) Chen, J.P.; Wu, S. Acid/base-treated activated carbons: Characterization of functional groups and metal adsorptive properties. *Langmuir* **2004**, *20*, 2233-2242.
- (194) Goyal, M.; Rattan, V.K.; Aggarwal, D.; Bansal, R.C. Removal of copper from aqueous solutions by adsorption on activated carbons. *Colloids and Surfaces A: Physicochemical and Engineering Aspects* **2001**, *190*, 229-238.
- (195) Lu, C.; Chiu, H. Chemical modification of multiwalled carbon nanotubes for sorption of  $Zn^{2+}$  from aqueous solution. *Chemical Engineering Journal* **2008**, *139*, 462-468.
- (196) Rangel-Mendez, J.R.; Streat, M. Adsorption of cadmium by activated carbon cloth: Influence of surface oxidation and solution pH. *Water Research* **2002**, *36*, 1244-1252.
- (197) Schierz, A.; Zänker, H. Aqueous suspensions of carbon nanotubes: Surface oxidation, colloidal stability and uranium sorption. *Environmental Pollution* **2009**, *157*, 1088-1094.
- (198) American Public Health Association; American Water Works Association; Water Environment Federation. *Standard Methods for the Examination of Water and Wastewater*; 20 ed.; American Public Health Association: Washington, D.C., 1998.
- (199) Saleh, N.B.; Pfefferle, L.D.; Elimelech, M. Aggregation kinetics of multiwalled carbon nanotubes in aquatic systems: Measurements and environmental implications. *Environmental Science and Technology* **2008**, *42*, 7963-7969.
- (200) Thomsen, C.; Reich, S.; Maultzsch, J. Resonant Raman spectroscopy of nanotubes. *Philosophical Transactions: Mathematical, Physical and Engineering Sciences* **2004**, *362*, 2337-2359.
- (201) Dresselhaus, M.S.; Eklund, P.C. Phonons in carbon nanotubes. *Advances in Physics* **2000**, *49*, 705-814.
- (202) Jishi, R.A.; Venkataraman, L.; Dresselhaus, M.S.; Dresselhaus, G. Phonon modes in carbon nanotubes. *Chemical Physics Letters* **1993**, *209*, 77-82.

- (203) Venkateswaran, U.D.; Rao, A.M.; Richter, E.; Menon, M.; Rinzler, A.; Smalley, R.E.; Eklund, P.C. Probing the single-wall carbon nanotube bundle: Raman scattering under high pressure. *Physical Review B: Condensed Matter and Materials Physics* **1999**, *59*, 10928-10934.
- (204) Bockrath, M.; Liang, W.; Bozovic, D.; Hafner, J.H.; Lieber, C.M.; Tinkham, M.; Park, H. Resonant electron scattering by defects in single-walled carbon nanotubes. *Science* **2001**, *291*, 283-285.
- (205) Shimodaira, N.; Masui, A. Raman spectroscopic investigations of activated carbon materials. *Journal of Applied Physics* **2002**, *92*, 902-909.
- (206) Koh, M.; Nakajima, T. Adsorption of aromatic compounds on C<sub>x</sub>N-coated activated carbon. *Carbon* **2000**, *38*, 1947-1954.
- (207) Reid, R.C.; Prausnitz, J.M.; Polling, B.E. *Properties of Gases and Liquids*; 4th ed.; McGraw-Hill: New York, 1987.
- (208) Rein, A.; Fernqvist, M.M.; Mayer, P.; Trapp, S.; Bittens, M.; Karlson, U.G. Degradation of PCB congeners by bacterial strains. *Applied Microbiology and Biotechnology* **2007**, *77*, 469-481.
- (209) Rehmann, L.; Daugulis, A.J. Biphenyl degradation kinetics by *Burkholderia xenovorans* LB400 in two-phase partitioning bioreactors. *Chemosphere* **2006**, *63*, 972-979.
- (210) Arnett, C.M.; Parales, J.V.; Haddock, J.D. Influence of chlorine substituents on rates of oxidation of chlorinated biphenyls by the biphenyl dioxygenase of *Burkholderia* sp. strain LB400. *Applied and Environmental Microbiology* **2000**, *66*, 2928-2933.
- (211) Erickson, B.D.; Mondello, F.J. Nucleotide sequencing and transcriptional mapping of the genes encoding biphenyl dioxygenase, a multicomponent polychlorinated-biphenyl-degrading enzyme in *Pseudomonas* strain LB400. *Journal of Bacteriology* **1992**, *174*, 2903-2912.
- (212) Haddock, J.D.; Nadim, L.M.; Gibson, D.T. Oxidation of biphenyl by a multicomponent enzyme system from *Pseudomonas* sp. strain LB400. *Journal of Bacteriology* **1993**, *175*, 395-400.
- (213) Haddock, J.D.; Gibson, D.T. Purification and characterization of the oxygenase component of biphenyl 2,3-dioxygenase from *Pseudomonas* sp. strain LB400. *Journal of Bacteriology* **1995**, *177*, 5834-5839.
- (214) Seeger, M.; Zielinski, M.; Timmis, K.N.; Hofer, B. Regiospecificity of dioxygenation of di- to pentachlorobiphenyls and their degradation to chlorobenzoates by the *bph*-encoded catabolic pathway of *Burkholderia* sp. strain LB400. *Applied and Environmental Microbiology* **1999**, *65*, 3614-3621.
- (215) Deneff, V.J.; Park, J.; Tsoi, T.V.; Rouillard, J.-M.; Zhang, H.; Wibbenmeyer, J.A.; Verstraete, W.; Gulari, E.; Hashsham, S.A.; Tiedje, J.M. Biphenyl and benzoate metabolism in a genomic context: Outlining genome-wide metabolic networks in *Burkholderia xenovorans* LB400. *Applied and Environmental Microbiology* **2004**, *70*, 4961-4970.

- (216) Denef, V.J.; Patrauchan, M.A.; Florizone, C.; Park, J.; Tsoi, T.V.; Verstraete, W.; Tiedje, J.M.; Eltis, L.D. Growth substrate- and phase-specific expression of biphenyl, benzoate, and C<sub>1</sub> metabolic pathways in *Burkholderia xenovorans* LB400. *Journal of Bacteriology* **2005**, *187*, 7996-8005.
- (217) Denef, V.J.; Klappenbach, J.A.; Patrauchan, M.A.; Florizone, C.; Rodrigues, J.L.M.; Tsoi, T.V.; Verstraete, W.; Eltis, L.D.; Tiedje, J.M. Genetic and genomic insights into the role of benzoate-catabolic pathway redundancy in *Burkholderia xenovorans* LB400. *Applied and Environmental Microbiology* **2006**, *72*, 585-595.
- (218) Zaitsev, G.M.; Tsoi, T.V.; Grishenkov, V.G.; Plotnikova, E.G.; Boronin, A.M. Genetic control of degradation of chlorinated benzoic acids in *Arthrobacter globiformis*, *Corynebacterium sepeidonicum* and *Pseudomonas cepacia* strains. *FEMS Microbiology Letters* **1991**, *81*, 171-176.
- (219) Loh, K.-C.; Chua, S.-S. *Ortho* pathway of benzoate degradation in *Pseudomonas putida*: Induction of *meta* pathway at high substrate concentrations. *Enzyme and Microbial Technology* **2002**, *30*, 620-626.
- (220) Hepworth, S.J.; Leach, M.O.; Doran, S.J. Dynamics of polymerization in polyacrylamide gel (PAG) dosimeters: (II) Modelling oxygen diffusion. *Physics in Medicine and Biology* **1999**, *44*, 1875-1884.
- (221) van Stroe-Biezen, S.A.M.; Everaerts, F.M.; Janssen, L.J.J.; Tacken, R.A. Diffusion coefficients of oxygen, hydrogen peroxide and glucose in a hydrogel. *Analytica Chimica Acta* **1993**, *273*, 553-560.
- (222) Stannett, V. Simple Gases. In *Diffusion in Polymers*; Crank, J., Park, G.S., Eds.; Academic Press Inc.: London, U.K., 1968; pp 41-73.
- (223) Cunliffe, A.V.; Davis, A. Photo-oxidation of thick polymer samples—Part II: The influence of oxygen diffusion on the natural and artificial weathering of polyolefins. *Polymer Degradation and Stability* **1982**, *4*, 17-37.

## Appendix A. Flux Prediction for a Sorptive Abiotic Membrane, a Biologically-Active Membrane, and Multi-Layered Active Membrane for PCB Containment

### A.1 Introduction

A layered barrier has been proposed for the *in situ* capping and treatment of polychlorinated biphenyl (PCB)-contaminated sediments. The proposed barrier would have a powdered activated carbon (PAC)-containing high-density polyethylene (HDPE) layer in contact with the contaminated sediments. This layer provides a strong, durable structure that physically separates the contaminated sediments from benthic organisms. The low permeability of HDPE slows diffusion of PCBs through the composite barrier, and the PAC further reduces PCB flux (see Chapter 4). The second layer is a hydrophilic membrane embedded with an aerobic, PCB-degrading bacterium, *Burkholderia xenovorans* strain LB400. Polyacrylamide (PAA) was used for initial laboratory experiments. The hydrophilic matrix allows diffusion of water and nutrients to the bacteria while protecting the LB400 from competition with other organisms. PCBs that pass through the HDPE layer are degraded by LB400 within the hydrophilic layer, further reducing the PCB exposure of aquatic organisms in the overlying sediments and water. The purpose of this section is to provide a theoretical basis for predicting reduced flux through the individual active layers and the composite membrane proposed.

The rate of LB400-mediated PCB degradation,  $r_{LB400}$ , has been described by the Monod equation (208):

$$r_{LB400} = \frac{k_M X C_m}{K_M + C_m} \quad (\text{A-1})$$

where  $k_M$  is the Monod second-order degradation rate constant,  $X$  is the biomass concentration (equivalent to  $C_{s0}$ , assumed somewhat constant for membrane-embedded bacteria), and  $K_M$  is the Monod half-saturation constant, or the concentration at which the degradation rate is equal to half of the maximum degradation rate.

When PCB concentrations in the membrane are low, kinetics can be described as first-order:

$$r_{LB400} = \frac{k_M X}{K_M} C_m \quad (\text{A-2})$$

This pseudo-first-order rate constant ( $k_M X / K_M$ ) can be used in tandem with the model 2 flux expression in Table 2-1 to predict the steady-state flux across this biologically-active layer.

When membrane concentrations are high, the degradation rate is zero-order with respect to  $C_m$ :

$$r_{LB400} = k_0 = k_M X \quad (\text{A-3})$$

The reaction-diffusion equation for a membrane with zero-order reaction is:

$$\frac{\partial C_m}{\partial t} = D \frac{\partial^2 C_m}{\partial x^2} - k_0 \quad (\text{A-4})$$

The steady-state solution to Equation A-4 can be used to define the steady-state flux:

$$j = \frac{DHC_{up}}{L} - \frac{k_0 L}{2} \quad (\text{A-5})$$

The following analysis uses the above equations and those described in Chapter 2 to predict the flux of PCBs through the single-layer barriers. All predictions assume  $C_{up} = 0.01$  nM, an estimate used in Chapter 4 based on sediment porewater concentrations reported in the literature. Base values for each of the input parameters are given in Table A-1. The  $D$  and  $H$  values for HDPE and  $R$ , the “effective” PAC particle size in sorbent-containing HDPE membranes, were determined for 2,3',4',5-tetrachlorobiphenyl (2,3',4',5-PCB) in Chapter 4.  $D$  and  $H$  for PAA were measured using a breakthrough experiment.<sup>3</sup> PAA membranes were loaded with LB400 during membrane preparation, resulting in membranes with 375 gm biomass/L, as given in Table A-1.<sup>4</sup>

### A.2 A Single PAC-Containing HDPE Barrier

Design variables for a PAC-containing HDPE membrane include membrane thickness and PAC particle loading (volume fraction). For pure polymers, flux is inversely proportional to  $L$ . Because of the exponential dependence of active membrane flux on  $L$  (Table 2-1), however, the effect of increasing  $L$  is much more pronounced in a PAC-containing membrane. The pseudo-steady-state flux is designated as  $j$  in Figure A-1.

Increasing the PAC content in a barrier membrane may transition breakthrough behavior from that described by the diffusion-limited sorption kinetics model to that described by the moving reactive front model. In effect, the flux is reduced to such a low level that the flux across the membrane is essentially zero (and looks like an extended lag time). The

**Table A-1.** Base values for predicting flux across single-layer and composite membranes

$D$ for HDPE	$8 \times 10^{-15} \text{ m}^2/\text{s}$
$H$ for HDPE	40,000
$R$	40 $\mu\text{m}$
$D$ for PAA	$8 \times 10^{-12} \text{ m}^2/\text{s}$
$H$ for PAA	7
$X$	375 mg biomass/L

<sup>3</sup> 2,3',4',5-PCB breakthrough across PAA was measured by Jenna Grady.

<sup>4</sup> LB400-containing PAA membrane were prepared by Jenna Grady.

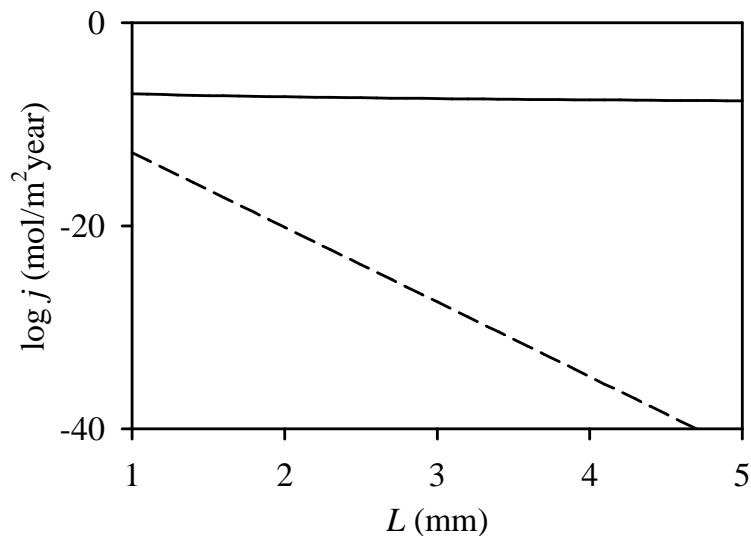


**Figure A-1.** Predicted pseudo-steady-state PCB flux across pure HDPE (—) and HDPE with  $R = 40 \mu\text{m}$  and  $\phi = 0.08$  (---) as a function of membrane thickness.

relationship between flux and PAC volume fraction described by Equation 2-19 and the model 2 flux expression in Table 2-1 is shown in Figure A-2.

$$k_1 = \frac{3D}{R^2 \left(1 - \phi^{1/3}\right) \left(\frac{1}{\phi} - 1\right)} \quad (2-19)$$

### A.3 A Single Biologically-Active PAA Barrier

If sediment PCB porewater concentrations ( $C_{up}$ ) are truly on the order of 0.01 nM, it is likely that the degradation rate will remain limited by PCB concentration in the membrane (0.07 nM) and not by the mechanisms of the bacteria described by Equation A-3.

At low PCB concentrations relative to  $K_M$ , the rate of PCB degradation is pseudo-first-order with respect to  $C_m$ , as described in Equation A-2. The Damköhler number for this membrane is:

$$\Phi = \frac{k_M X L^2}{K_M D} \quad (A-6)$$

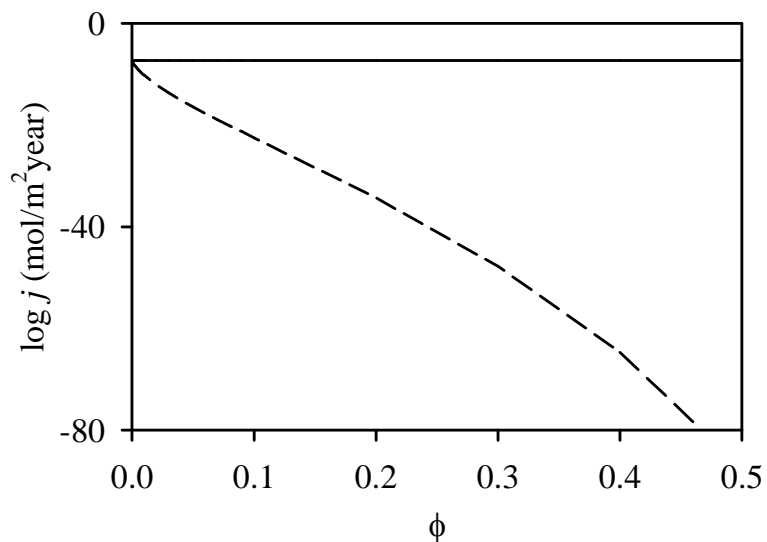


**Figure A-2.** Predicted PCB flux across 2 mm pure HDPE (—) and sorbent-containing HDPE (---) as a function of PAC volume fraction in the membrane.

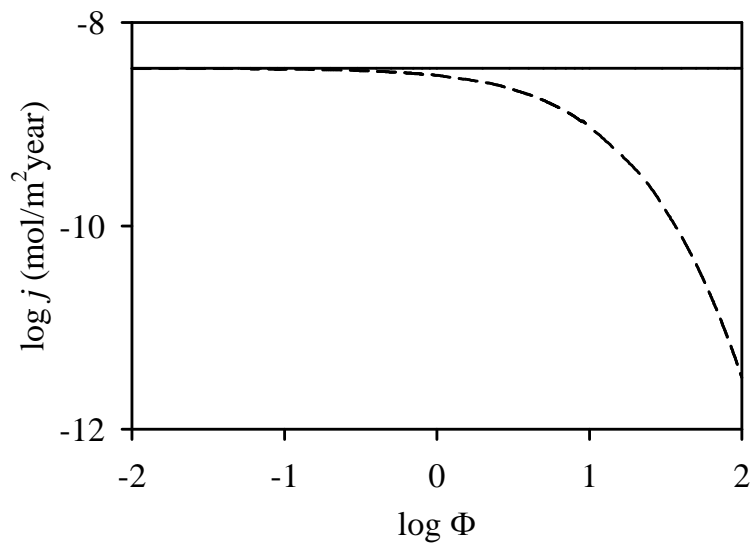


**Figure A-3.** Predicted PCB flux across 5 mm pure PAA (—) and biologically-active PAA (---) as a function of the Damköhler number.

Di Felice et al. (2) concluded using a series of model predictions that flux is relatively unaffected by reaction when  $\Phi < 0.01$  and that flux is practically zero (as described by the moving reactive front model) when  $\Phi > 100$ . Instead of studying flux as a function of  $k_M$  or  $K_M$ , the effect of PCB degradation is given in Figure A-3 as a function of  $\Phi$ .

The degradation kinetics parameters,  $k_M$  and  $K_M$ , are  $1.9 \times 10^{-6}$   $\mu\text{mol}/\text{mg}\cdot\text{s}$  and  $0.034$   $\mu\text{M}$ , respectively, according to Rein et al. (208). Rehmann and Daugulis (209) measured these parameters for the degradation of biphenyl and reported that  $k_M = 9.4 \times 10^{-4}$   $\mu\text{mol}/\text{mg}\cdot\text{s}$  and  $K_M = 0.65$   $\mu\text{M}$ . The rate of degradation of 2,3',4',5-PCB by  $\text{ISP}_{\text{BPH}}$  (the iron-sulfur protein in 2,3-biphenyl dioxygenase responsible for catalyzing the dioxygenation of biphenyl) was similar to that for biphenyl (210). If this is the case, greater agreement between the values reported by Rein et al. (208) and Rehmann and Daugulis (209) is expected. Regardless, the degradation rate within membranes is expected to be lower than in these free solution experiments due to the physical constraints imposed by the membrane structure. Assuming the values for  $X$ ,  $L$ , and  $D$  given in Table A-1 and  $K_M = 0.034$   $\mu\text{M}$  as reported by Rein et al. (208), the range of  $\Phi$  in Figure A-3 corresponds to a range in  $k_M$  from  $3 \times 10^{-13}$  to  $3 \times 10^{-9}$   $\mu\text{mol}/\text{mg}\cdot\text{s}$ .

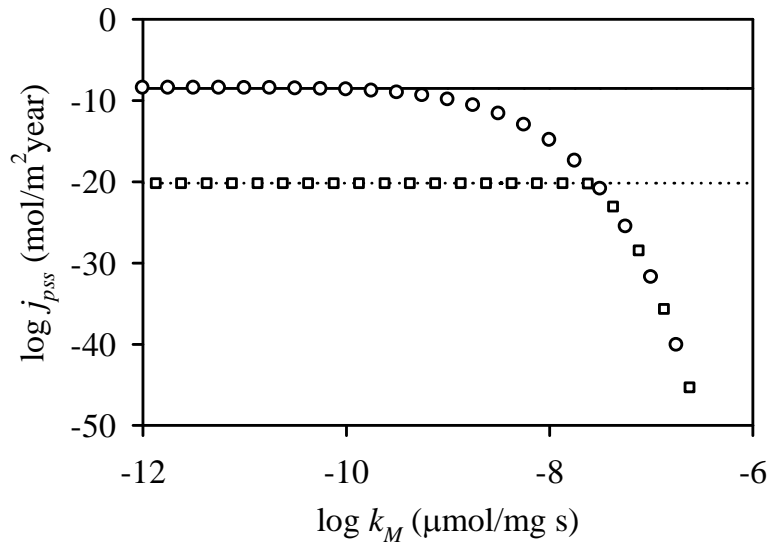


**Figure A-4.** Predicted PCB flux across 2-layer barriers: 2 mm pure HDPE + 5 mm pure PAA (—), 2 mm pure HDPE + 5 mm PAA with 375 mg LB400 biomass/L (○), 2 mm HDPE with PAC  $\phi = 0.08$  + 5 mm pure PAA (⋯), and 2 mm HDPE with PAC  $\phi = 0.08$  + 5 mm PAA with 375 mg LB400 biomass/L (□).

#### ***A.4 A Composite Abiotic/Biologically-Active Barrier for PCB Containment***

The pseudo-steady-state flux across the layered barrier proposed above can be estimated using Equation 2-26 with  $L_{A2} = 0$ . This flux is given as a function of  $k_M$  in Figure A-4.

$$\frac{L_{composite}}{P_{composite}} = \frac{L_{A1} + L_{A2}}{P_A} + \frac{L_B}{P_B} \quad (2-26)$$

From Figure A-4, we can conclude that the resistance of the PAC-containing HDPE layer to PCB diffusion dominates for  $k_M < 10^{-7.5}$   $\mu\text{mol}/\text{mg}\cdot\text{s}$ . If the degradation rate by PAA-encapsulated LB400 is slower, there is no point in adding the LB400 bacteria to the PAA layer of this barrier membrane. Conversely, if degradation is fast ( $k_M > 10^{-7.5}$   $\mu\text{mol}/\text{mg}\cdot\text{s}$ ), the addition of PAC to the HDPE layer may be unnecessary.

## **Appendix B. *Burkholderia xenovorans* strain LB400 growth on benzoate at reduced dissolved oxygen concentrations**

### ***B.1 Introduction***

The proposed layered barrier membrane containing *Burkholderia xenovorans* strain LB400 has the potential to drastically improve containment of polychlorinated biphenyl (PCB)-contaminated sediments. LB400 is an aerobic bacterium that can metabolize biphenyl and cometabolize PCBs using molecular oxygen (O<sub>2</sub>) as its electron acceptor (211-215). Limited access to O<sub>2</sub>, however, is expected to impede the degradation performance of membrane-bound bacteria. The purpose of this study was to evaluate the effect of reduced dissolved oxygen concentrations on LB400 growth.

### ***B.2 Experimental Methodology***<sup>5</sup>

#### ***B.2.1 Experimental Apparatus Design***

Filtered (0.22 μm nylon, Acrodisc) high-pressure air and nitrogen were mixed and humidified in two parallel bottles partially filled with water. Each bottle was sealed with a rubber stopper fitted with three pieces of copper tubing: one connected to a fish tank aerator for sparging the water with air, one connected to a fish tank aerator for sparging the water with nitrogen, and one for collecting the exit gas to send to the reactors. Each exit gas line was split into three so that a total of six reactors could be accommodated by the experimental set-up. Because of bends in the copper tubing, the mixing/humidifying process resulted in different dissolved oxygen concentrations in each set of three reactors when both air and nitrogen valves were open. This effect was desired so that growth experiments could be conducted at two dissolved oxygen concentrations at once.

The six reactors were made from autoclavable 250-mL screw-cap bottles by drilling three holes into the each cap: one was fitted with polytetrafluoroethylene (PTFE) tubing for bubbling the reactor contents with the mixed, humidified gas, one was plugged with a rubber stopper for use as a sample port, and the last allowed gas to leave the system so as to avoid pressure build-up. A magnetic stir bar was placed in each reactor. The photo in Figure B-1 shows the fully-assembled experimental set-up.

#### ***B.2.2 Growth Experiments***

Because LB400 can grow using a variety of substrates (including biphenyl, benzoate, succinate, etc.) (216,217), a highly-soluble, non-volatile substrate, benzoate, was chosen as the electron donor/carbon source for this study. Each reactor was filled with 176 mL of 1.14 mM potassium benzoate (0.1342 g benzoic acid: 99.8%, J.T. Baker; 0.0680 g potassium hydroxide: 88%, Mallinckrodt; 1.08 L nanopure water, Milli-Q, Millipore). The entire apparatus shown in Figure A2-1 was sterilized in an autoclave at 121 °C at 15 psig for 40 minutes. After cooling, the entire apparatus was moved to a warm room set to

---

<sup>5</sup> Experiments were designed and conducted by Erin Surdo and Katherine Phillips.



**Figure B-1.** Experimental apparatus used for supplying LB400 with a constant stream of reduced-oxygen gas. In this photo, two of the reactors (and one control) were used to measure the growth of *Synechocystis* sp. PCC 6803 (a blue-green algae) and three were used to measure LB400 growth on biphenyl, which necessitated a carbon trap at the reactor exit.

30 °C and reactors were lined up on a multi-point stir plate. Twenty milliliters of sterile 10× K1 stock and 4 mL sterile Hunter Mix (218) were added to each reactor, and the air valve was opened to begin sparging. LB400 grown on K1 plates sprinkled with biphenyl were used to streak a K1 plate with 1 mM potassium benzoate. After incubation for at least two days, LB400 on this latter plate were used to inoculate a seed reactor (reactor 1). The seed reactor was incubated overnight with 21% oxygen bubbling through the system.

The nitrogen valve was opened one hour before starting the reduced oxygen experiments. Reactors 2, 4 and 5 were inoculated with 2 mL each from the seed reactor (reactor 1). (Reactors 2 and 6 were sterile controls.) Optical density at 600 nm ( $OD_{600}$ , used to measure biomass concentration as described below) of the seed reactor was 0.171 and 0.196 for the 21% oxygen experiment and the reduced oxygen experiments, respectively. Biomass, benzoate, and dissolved oxygen concentrations were monitored during each experiment.

### *B.2.3 Measurement of Bacterial Growth*

Three-milliliter samples were collected from each reactor at timepoints throughout the experiment using sterile techniques. The samples were transferred to acrylic cuvettes, and the optical density of samples at 600 nm was measured using a Shimadzu UV-1601PC spectrophotometer.  $OD_{600}$  is commonly used to estimate biomass concentrations in liquid culture, a technique that assumes a linear relationship between cell concentration and  $OD_{600}$ . For example, Rein et al. (208) reported a correction factor of 0.263 for LB400 such that biomass concentration (g/L) could be estimated as  $0.263 \cdot OD_{600}$ . The concentration factor cancels out when  $OD_{600}$  data are used to estimate growth rates,

however, so no particular conversion factor was required for use in our calculations. Thus, the conversion factor was not measured for our specific growth substrate and set of growth conditions.

#### *B.2.4 Measurement of Benzoate Consumption*

Samples (1.5 mL) were also collected for benzoate concentration measurements. Samples were collected using sterile techniques, transferred to 1.5-mL centrifuge tubes, and centrifuged at 13,000 rpm for one minute. The supernatant was filtered through a 0.22  $\mu\text{m}$  nylon syringe filter, and a 500-mL aliquot of the filtered sample was diluted to 5.5 mL with sterile K1 media. The absorbance of the diluted samples was measured through a quartz cuvette at 226 nm using the Shimadzu UV-1601PC spectrophotometer. Some samples were also scanned from 190 nm to 800 nm to determine if other dissolved compounds present in the samples were interfering with  $\text{OD}_{600}$  measurements. A set of eight standards ranging in concentration from 0.001 to 0.100 mM potassium benzoate was used to calibrate the absorbance measurements.

#### *B.2.5 Measurement of Dissolved Oxygen Concentration*

Dissolved oxygen concentrations were measured using an MI-730 oxygen electrode (Microelectrodes, Inc.). The probe tip was sterilized with ethanol (200 proof, AAPER Alcohol and Chemical Co.) and rinsed with nanopure water prior to each measurement. Dissolved oxygen was measured by placing the probe tip directly into each reactor for approximately one minute. The probe was zeroed before each experiment (in nitrogen-sparged nanopure water) and calibrated in air-sparged water before and after each set of measurements. Significant drift was observed during each set of measurements and was assumed to be linear. That is, the calibration was linearized using calibration data points taken before and after each set of measurements.

### **B.3 Results**

LB400 growth curves are shown for experiments sparged with 21% oxygen in Figure B-2. Figure B-3 shows LB400 growth curves at reduced oxygen levels. Dissolved oxygen concentrations are reported in %, where water in equilibrium with air would have a dissolved oxygen concentration of 21%.

Growth rate constants were determined by linearizing the growth curves ( $\ln \text{OD}_{600}$  vs. time, not shown) and regressing data during growth. The slope is equivalent to the pseudo-first-order growth rate constant. The pseudo-first-order rate constants,  $k_1$ , for all inoculated reactors are plotted against dissolved oxygen concentrations in Figure B-4.

Care was taken to ensure that the growth rate constant was measured only for periods when benzoate concentrations were also constant so that pseudo-first-order kinetics could be assumed. Benzoate concentrations are shown in Figures B-5 and B-6. Scanning of the benzoate samples at higher wavelengths resulted in an observed peak at approximately 551 nm that may have interfered with  $\text{OD}_{600}$  measurements. An attempt to correct  $k_1$  for

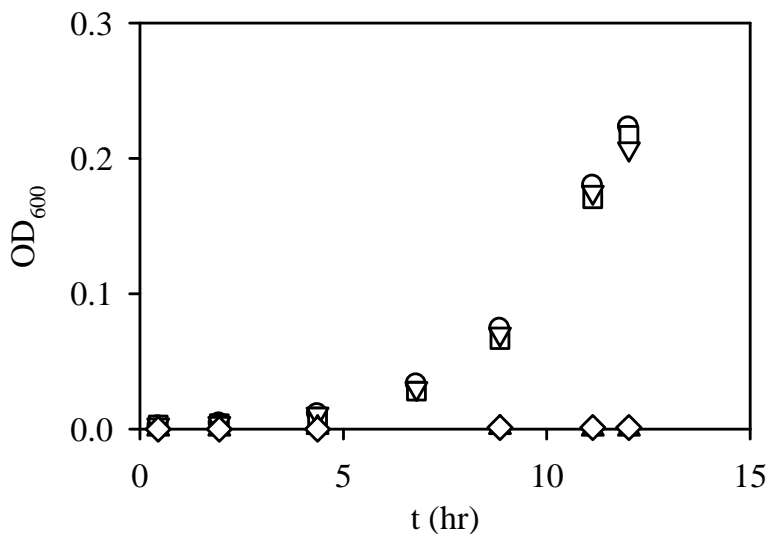


**Figure B-2.** Optical density at 600 nm ( $OD_{600}$ ) as a measure of LB400 concentration for inoculated reactors ( $\circ, \square, \nabla$ ) and sterile controls ( $\triangle, \diamond$ ) with  $21.7 \pm 0.5\%$  oxygen.

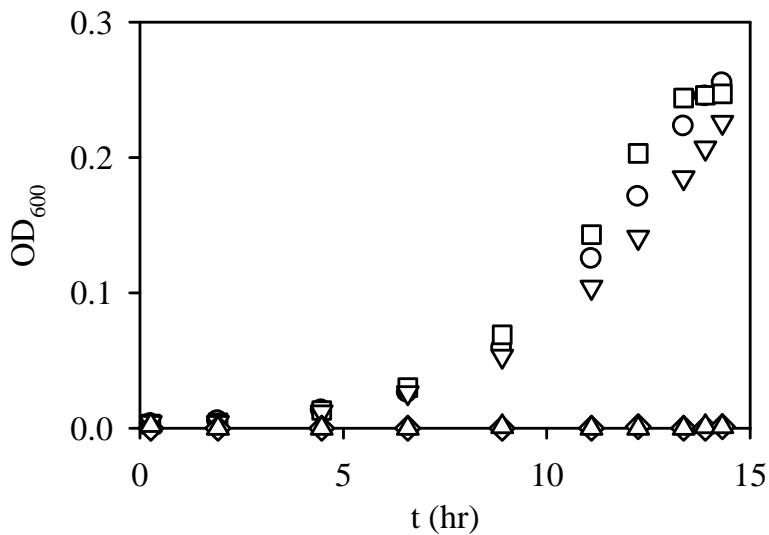


**Figure B-3.** Optical density at 600 nm ( $OD_{600}$ ) as a measure of LB400 concentration for inoculated reactors with  $13.4 \pm 0.3\%$  oxygen ( $\circ, \square$ ), and  $10.7 \pm 0.4\%$  oxygen ( $\nabla$ ) maintained throughout each experiment. Sterile controls with  $13.4 \pm 0.3\%$  oxygen ( $\triangle$ ) and  $10.7 \pm 0.4\%$  oxygen ( $\diamond$ ) are also shown.

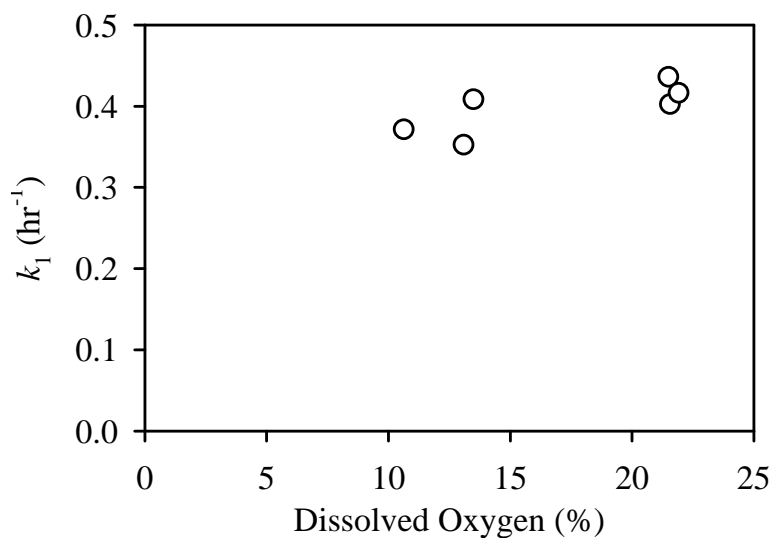


**Figure B-4.** Pseudo-first-order growth rate constants for LB400 growth on benzoate (1 mM) at various dissolved oxygen concentrations.

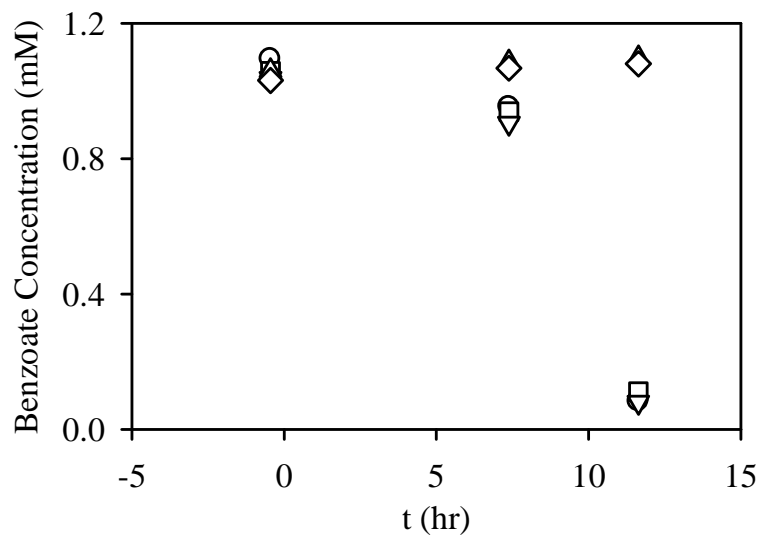


**Figure B-5.** Benzoate concentration in inoculated reactors (○,□,▽) and sterile controls (△,◇) with  $21.7 \pm 0.5\%$  oxygen.

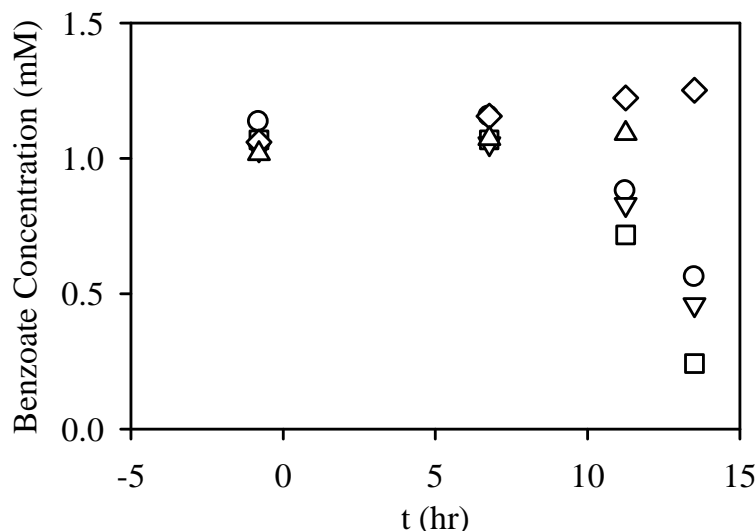


**Figure B-6.** Benzoate concentration in inoculated reactors with  $13.4 \pm 0.3$  % oxygen ( $\circ, \square$ ), and  $10.7 \pm 0.4$  % oxygen ( $\nabla$ ) maintained throughout each experiment. Sterile controls with  $13.4 \pm 0.3$  % oxygen ( $\triangle$ ) and  $10.7 \pm 0.4$  % oxygen ( $\diamond$ ) are also shown.

this interference was unsuccessful, because negative  $OD_{600}$  values were obtained in several cases.

#### **B.4 Discussion**

The pseudo-first-order rate constants at reduced oxygen conditions shown in Figure B-4 are lower than those measured for air-saturated conditions, but not by as much as was expected based on stoichiometry. It is likely that at 21% oxygen, the rate is limited by the growth mechanisms of the bacteria and not by the concentration of oxygen available for the growth reaction. Unfortunately, not enough data are available to develop a Monod-type expression for growth rate as a function of dissolved oxygen concentration.

Growth experiments at dissolved oxygen concentrations closer to zero would ideally be conducted to determine when oxygen becomes truly limiting. Unfortunately, two major complications prevented further experiments. First, the disfunctional heating element in our warm room prevented us from conducting further experiments at a constant 30 °C. Second, and more importantly, color formation in the media during LB400 growth interfered with  $OD_{600}$  measurements. Loh and Chua (219) studied benzoate degradation by *Pseudomonas putida* (which uses metabolic pathways for benzoate degradation similar to those used by LB400) and observed the accumulation of catechol when cells were grown in the presence of high benzoate concentrations. Further, they observed the

**Table B-1.** Oxygen diffusion coefficients ( $D$ ) reported in the literature

Polymer	$D$ (m <sup>2</sup> /s)	Reference
polyacrylamide	$8 \times 10^{-10}$	(220)
poly(vinyl alcohol)	$3.6-6.8 \times 10^{-10}$	(221)
high-density polyethylene	$1.7-5.4 \times 10^{-11}$	(1,222)
low-density polyethylene	$4.8 \times 10^{-11}$	(223)

formation of a brownish product when cells were grown in using catechol as the sole carbon source, and they attributed the color formation to the abiotic autopolymerization of catechol (219). While the color formation in our reactors was more of a purple-ish color than a brownish one, it is possible that a similar mechanism is the cause of the colored product formation observed in our reactors. Because the observed color of the product was deeper at lower dissolved oxygen concentrations, we suspect that further reducing oxygen would result in an even more significant interference from this product.

The purpose of the oxygen growth experiments was to determine the oxygen concentration required to maintain LB400 function within membrane systems, where oxygen availability may be limiting. Although we were unable to confirm the minimum oxygen concentration required to maintain LB400 growth, we can estimate the rate of oxygen delivery to the LB400. A literature review uncovered reported values of oxygen diffusion through the various polymers used in our current research, including polyacrylamide (Table B-1). Often, polymer preparation procedures and experimental conditions do not exactly match those used in our research, but the values in Table B-1 should be sufficient for model calculations.

Oxygen diffusion through polyacrylamide and through the other polymers considered for use in layered LB400-containing barrier systems is high relative to 2,3',4',5-tetrachlorobiphenyl (2,3',4',5-PCB) diffusion ( $8 \times 10^{-12}$  m<sup>2</sup>/s in polyacrylamide<sup>6</sup>). Oxygen diffusion is also expected to be high relative to most other carbon sources that LB400 may use for growth and maintenance, such as benzoate. Therefore, oxygen should not be the limiting variable when oxygen and a carbon source (or PCBs) are both delivered to the membrane-bound LB400 via diffusion.

---

<sup>6</sup> From breakthrough experiment data collected by Jenna Grady.

**Appendix C.** Equilibrium Adsorption/Partitioning of 1,2,4-TCB and  $\text{Cu}^{2+}$  in Sorbent-Containing poly(vinyl alcohol) (PVA) Membranes

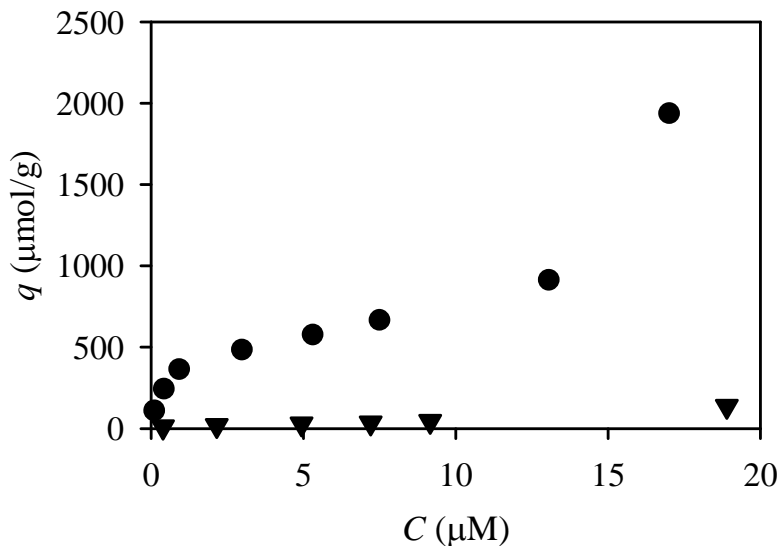


**Figure C-1.** Membrane “isotherm” data for aqueous 1,2,4-TCB in equilibrium with sorbent particles in PVA coupons containing 69 g/L PAC (●) and 77 g/L SWCNT (▼).

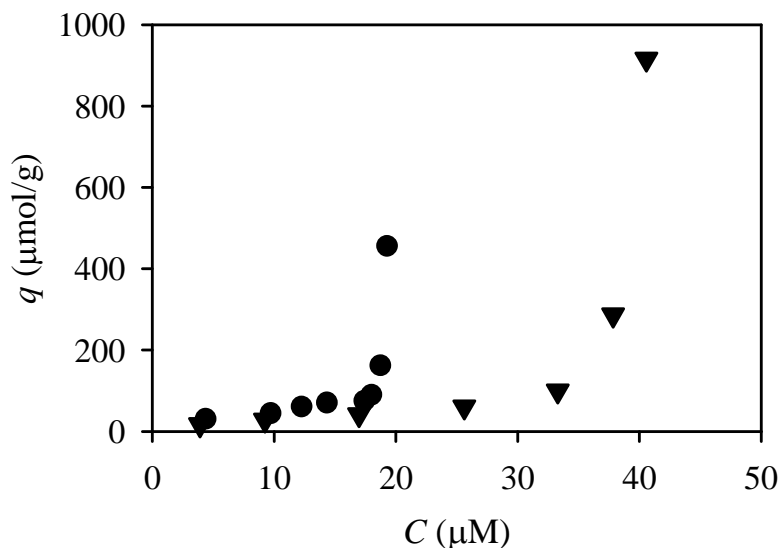


**Figure C-2.** Membrane “isotherm” data for aqueous 1,2,4-TCB in equilibrium with sorbent particles in PVA coupons containing 62 g/L ox-PAC (●) and 42 g/L ox-SWCNT (▼).

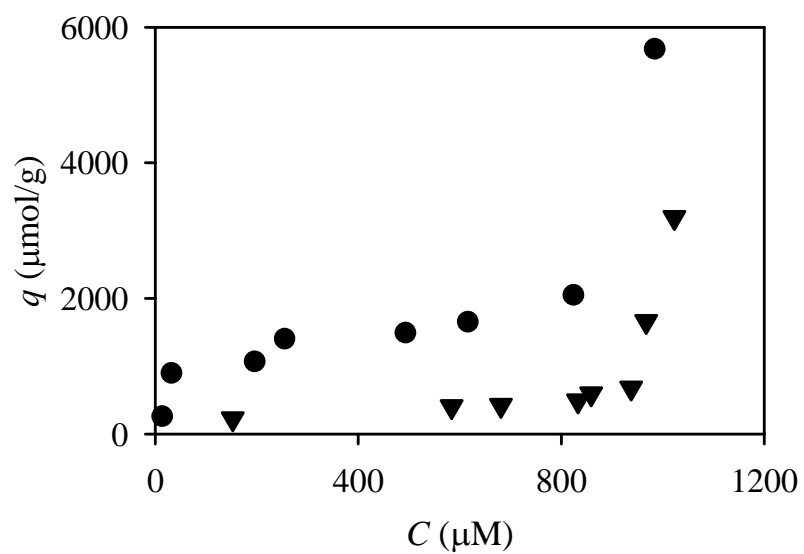


**Figure C-3.** Membrane “isotherm” data for aqueous  $\text{Cu}^{2+}$  in equilibrium with sorbent particles in PVA coupons containing 186 g/L ox-PAC (●) and 157 g/L ox-SWCNT (▼).

**Appendix D.** Raman Spectra for Raw and Functionalized SWCNTs and PAC

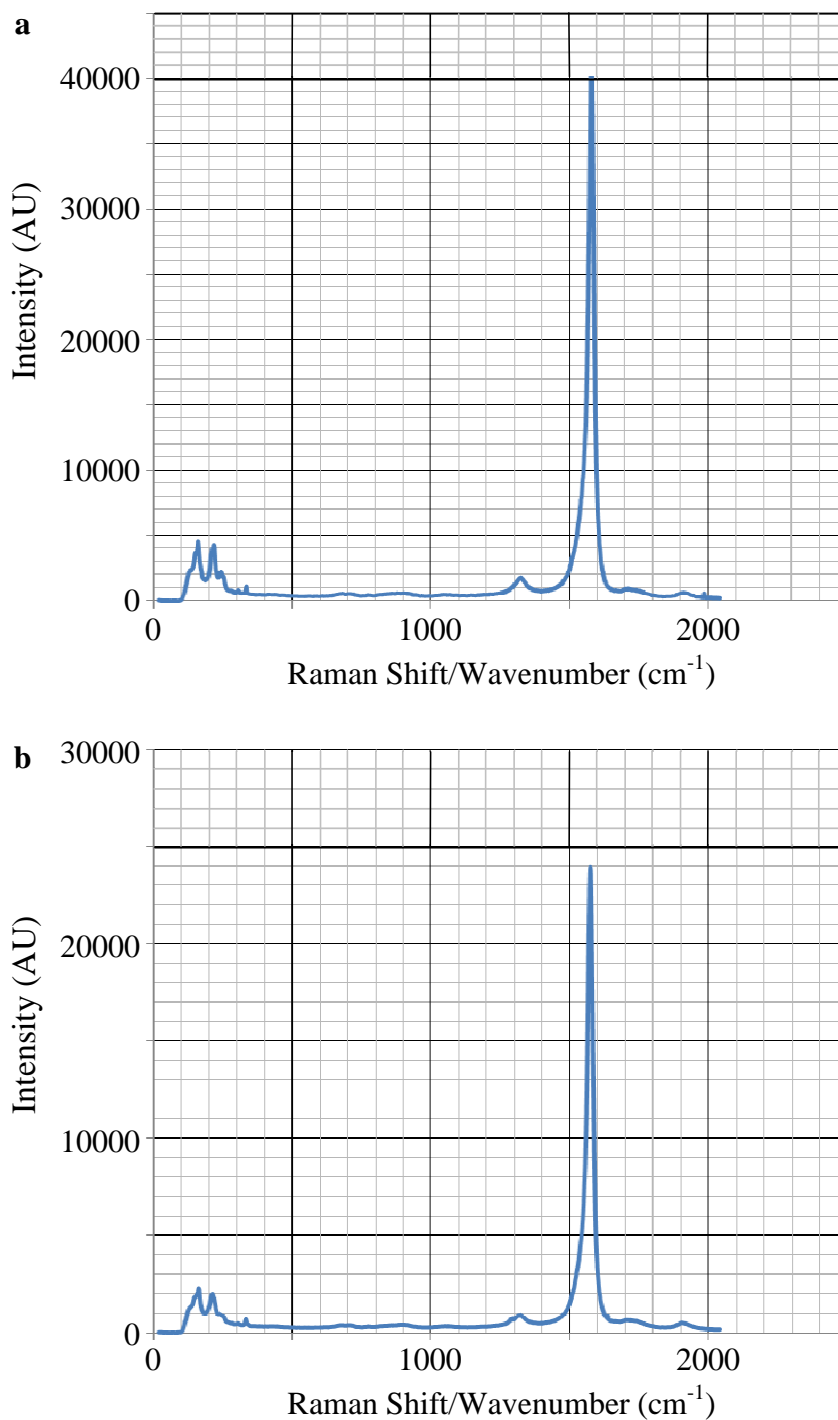


**Figure D-1.** Raman spectra at 632 nm of SWCNT (a) and ox-SWCNT (b).

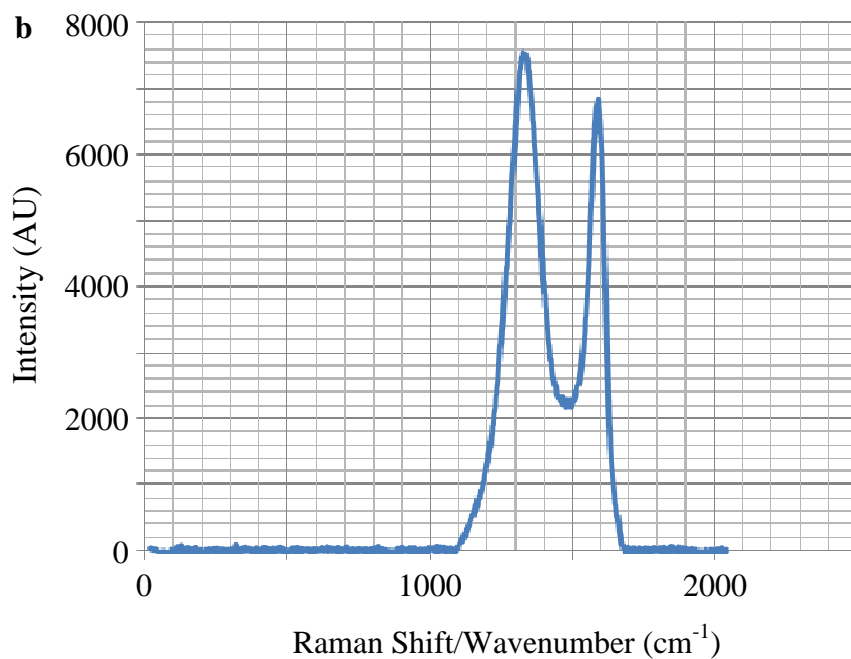
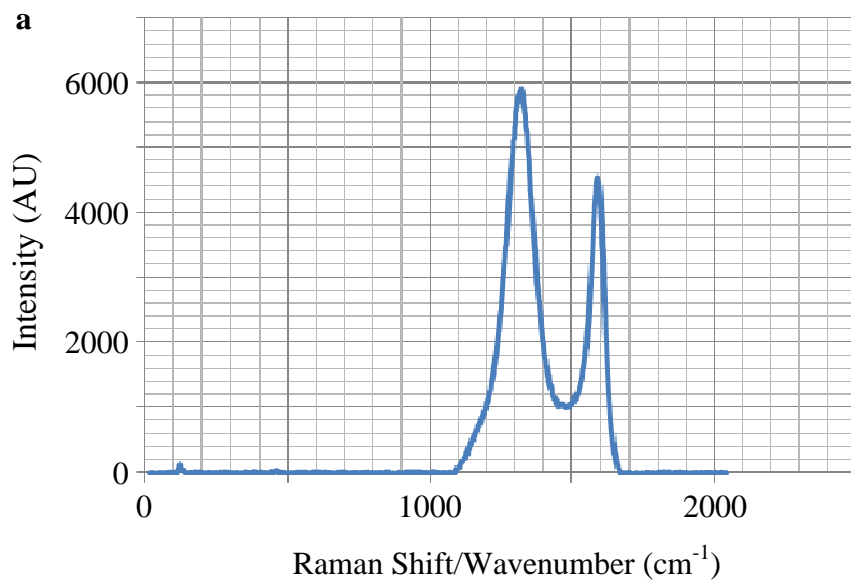


**Figure D-2.** Raman spectra at 632 nm of PAC (a) and ox-PAC (b).